CHEMICAL REVIEWS

Review

pubs.acs.org/CR

# Lanthanide-Activated Phosphors Based on 4f-5d Optical Transitions: Theoretical and Experimental Aspects

Xian Qin,*[,†] Xiaowang Liu,[†] Wei Huang,*[,‡,§] Marco Bettinelli,*[,∥] and Xiaogang Liu*[,†,⊥]

[†]Department of Chemistry, National University of Singapore, 3 Science Drive 3, Singapore 117543, Singapore

[‡]Key Laboratory of Flexible Electronics and Institute of Advanced Materials, Jiangsu National Synergetic Innovation Center for Advanced Materials, Nanjing Tech University, Nanjing 211816, P. R. China

[§]Key Laboratory for Organic Electronics and Information Displays & Institute of Advanced Materials, Jiangsu National Synergetic Innovation Center for Advanced Materials, Nanjing University of Posts and Telecommunications, Nanjing 210023, P. R. China

[∥]Luminescent Materials Laboratory, DB, University of Verona, Strada Le Grazie 15, I-37134 Verona, Italy

[⊥]Center for Functional Materials, NUS Suzhou Research Institute, Suzhou, Jiangsu 215123, P. R. China

**ABSTRACT:** The synthesis of lanthanide-activated phosphors is pertinent to many emerging applications, ranging from high-resolution luminescence imaging to next-generation volumetric full-color display. In particular, the optical processes governed by the 4f-5d transitions of divalent and trivalent lanthanides have been the key to enabling precisely tuned color emission. The fundamental importance of lanthanide-activated phosphors for the physical and biomedical sciences has led to rapid development of novel synthetic methodologies and relevant tools that allow for probing the dynamics of energy transfer processes. Here, we review recent progress in developing methods for preparing lanthanide-activated phosphors, especially those featuring 4f-5d optical transitions. Particular attention will be devoted to two widely studied dopants, $Ce^{3+}$ and $Eu^{2+}$. The nature of the 4f-5d transition is examined by combining phenomenological theories with quantum mechanical calculations. An emphasis is placed on the correlation of host crystal structures with the 5d-4f luminescence characteristics of lanthanides, including quantum yield, emission color, decay rate, and thermal quenching behavior. Several parameters, namely Debye temperature and dielectric constant of the host crystal, geometrical structure of coordination polyhedron around the luminescent center, and the accurate energies of 4f and 5d levels, as well as the position of 4f and 5d levels relative to the valence and conduction bands of the hosts, are addressed as basic criteria for high-throughput computational design of lanthanide-activated phosphors.

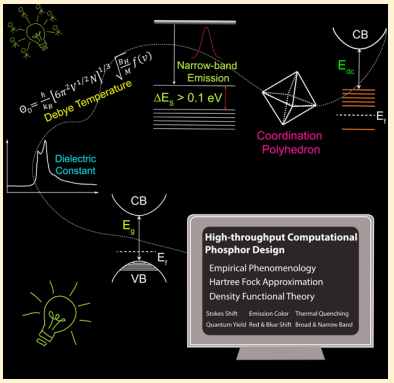


## CONTENTS



**Received:** October 10, 2016





DOI: 10.1021/acs.chemrev.6b00691
*Chem. Rev.* XXXX, XXX, XXX–XXX

## 1. INTRODUCTION

Rare-earth elements are a set of 17 chemical elements, the lanthanides along with the transition metals scandium and yttrium, that are highly recognized for their versatile applications, ranging from high-tech products and green technologies to health and medical utilization.[1,2] Particularly, there has been a steady increase in the theoretical and experimental studies of lanthanide-activated inorganic phosphors over the past decade, principally due to an ever-increasing demand for photoluminescence and related applications, including lighting, electronic display, lasing, anticounterfeiting, biological labeling, and imaging (Figure 1).[3−9] In contrast to organic dye-based fluorescent labels, the

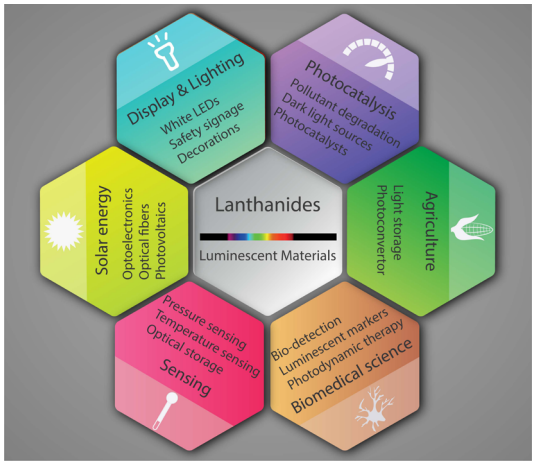


**Figure 1.** Various applications of lanthanide-activated inorganic phosphors.

lanthanide-activated phosphors offer better photostability and improved color performance in the form of higher monochromatic (color) purity and spatial resolution. Moreover, these inorganic phosphors present wide optical tunability over emission wavelength and lifetime, as enabled by the intraconfigurational 4f-4f and interconfigurational 4f-5d transitions of lanthanides (Figure 2).[10,11] When compared with the parity forbidden transitions within the f-manifold of lanthanides, the $4f^n$-$4f^{n-1}5d^1$ optical transitions are often characterized by high radiative emission probability and short lifetime (tens of nanoseconds) because the f-d transition is electrical-dipole allowed. Furthermore, unlike the sharp linelike emission associated with the transition of the f-f type, the f-d transition generally features much broader absorption and emission spectra owing to the high sensitivity of 5d orbital to the surrounding environment. It is thus conceivable to employ the 4f-5d transitions of lanthanides for situations in which large oscillator strengths, broad absorption bands, or fast response

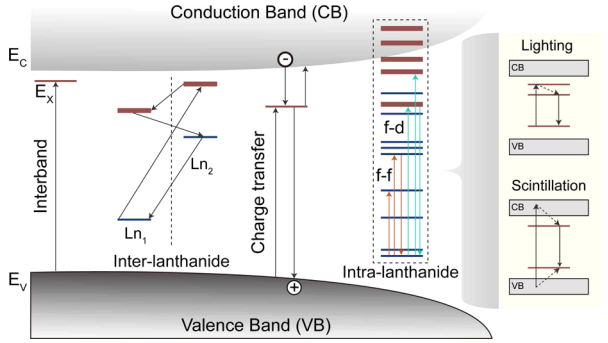


**Figure 2.** Schematic diagram showing four types of electronic transition in lanthanide-activated inorganic compounds. $E_x$ represents the energy needed to excite an electron from the top of the valence band across the band gap to form an exciton. $E_c$ and $E_v$ are the energies of conduction band minimum and valence band maximum, respectively. Interband transition corresponds to the process where an electron is excited from the top of the valence to an exciton state. Charge transfer refers to electron transfer between the dopant and the host. The interlanthanide transition is related to the electron transfer between any two lanthanide ions adjacently doped in the host material, while intralanthanide transition is related to the process where an electron is excited from the lanthanide's occupied 4f orbitals to its unoccupied 4f or 5d orbitals. The inset on the right side shows a schematic illustration of typical excitation and emission processes dominated in lanthanide-based phosphors for lighting (top panel) and scintillation (bottom panel) applications. Adapted with permission from ref 275. Copyright 2012 Royal Society of Chemistry.

times are required. With the advent of thin film technology and rapid development in the semiconductor industry, inorganic phosphors exhibiting 4f-5d transitions have achieved important status. White light emitting diodes (LEDs), which utilize yellow light emitting YAG:Ce (cerium-doped yttrium aluminum garnet; $Y_3Al_5O_{12}:Ce^{3+}$) phosphor overcoated onto a blue InGaN LED, are already commercially available.[12,13] Moreover, the utilization of 4f-5d transitions of $Ce^{3+}$ in $LaBr_3$, $LuI_3$, and $YI_3$ compounds has made the brightest scintillators accessible for applications in the areas of security measures and particle physics.[14−16]

Despite the complex mechanisms underlying lanthanide-based luminescence (Figure 2), the pronounced effects of host materials on luminescence properties, including emission color, quantum conversion efficiency, and thermal quenching behavior, have been demonstrated for all types of 4f-5d optical transitions. For example, the 5d-4f luminescence properties of $Eu^{2+}$ have been compiled for more than 300 compounds, in which the emission color can be precisely tuned from near-ultraviolet to deep red.[17] Obviously, apart from choosing different lanthanide emitters, an alternative route toward tunable luminescence is to vary the type of host material, benefiting from the subtle response of lanthanide emitters ($Ln^{3+}$ or $Ln^{2+}$) at their 5d energy levels to the environment. Not only can phosphor materials for lighting benefit from host tailoring but also can the scintillators which can be considered as phosphors for detecting high energy ionizing radiation.

Through modulation of host lattices and dopant composition, a large variety of lanthanide-doped scintillators containing halides and oxides have been prepared, displaying fascinating optical characteristics such as high luminance, fast response, and excellent energy resolution.[18] On a separate development, Pust et al. have recently synthesized a narrow-band, red-emitting $Eu^{2+}$-doped phosphor featuring low thermal quench-


DOI: 10.1021/acs.chemrev.6b00691
Chem. Rev. XXXX, XXX, XXX−XXX

ing and high color rendering index using nitridoaluminate as the host lattice.[19] Despite these achievements, the basic role of the host in affecting the f-d transition of the dopants has yet been fully understood. Indeed, the mechanisms of action of host lattice on the scintillation response time in different $Ce^{3+}$-doped materials are some currently active topics of investigation in materials chemistry.[20] It is worth noticing that many lanthanides suffer from concentration quenching at elevated temperatures, as confirmed by a deprivation of the 5d-4f radiative emission in some hosts.[21] Other challenging issues include enhancement of luminescence efficiency and precise tuning over emission color.

In the recent past, scientific advances through experimentation have provided an abundance of theoretical insights into the rational design of high-performance lanthanide-activated phosphors. This development was best exemplified by the practice of the phenomenological approach, which has been used since the 1970's as an effective research tool to acquire information through inductive, qualitative methods based on a paradigm of personal knowledge and interpretation. As in most such studies, Dorenbos has devoted his career to analyzing energy levels of divalent and trivalent lanthanides doped in more than 1000 inorganic compounds.[22−24] Using phenomenology-based empirical equations, the 4f-5d absorption and emission energies of lanthanides incorporated in a given crystalline material could principally arrive within an acceptable error margin of the available experimental data. These investigations provide a theoretical basis on how redshift, defined as a consequence of centroid shift and crystal field splitting, responds to changes in the local environment of the activator (Figure 3).

There is currently a major trend for expanding our understanding of 4f-5d transitions in lanthanide-activated phosphors, that is, the construction of computational models to study the optical behavior of a complex system.[25−29] By doing so, mathematical equations can be incorporated into computational codes, expressed graphically, and manipulated easily with editing commands. A handy control of simulations can advance theories, thereby triggering new ideas and insights. Computational work can also complement current experimental techniques. In some cases, the development of theory is vital to our experimental progress. With the help of computational tools, researchers could essentially explore the physical and chemical properties of any substances at the atomic and molecular level using a series of empirical parameter-free methodologies, such as quantum mechanical methods based on density functional theory (DFT) and Hartree−Fock (HF) theory. As such, high-throughput computing has made it possible to design new materials from lab testing to commercial application within a considerably short period of time.[30−32]

The combination of advanced quantum chemistry methods and supercomputers has now provided researchers with a new opportunity to exploit the 4f-5d transition of lanthanides beyond reach with current experimental technology and, consequently, create a new breed of high efficiency phosphors with improved luminescence characteristics, sufficient chemical durability, and little photothermal degradation. However, the existing theories seem incapable of explaining experimental anomalies of emission because of intrinsic limitations of the computational approaches. Strongly electron-correlated materials containing rare-earth metal ions with partially filled f shells are examples where deficiency of the DFT method involving local density approximation is most clearly shown.

In this review, we begin by brief discussions of the recent approaches to synthesizing lanthanide-activated phosphors both in bulk and in nano form. This is followed by a careful evaluation of the predictive power that can be expected from the combined application of quantum computational techniques and phenomenological methodology for important luminescence properties. We focus on the phenomenological theory employed by Dorenbos as an essential descriptive guideline for examples of some selected areas of application. A parallel focus is placed on the theoretical background and the technical aspects of DFT- and HF-based methodologies through which the criteria for the design of high-performance phosphors can readily be identified. Recent advances involving lanthanide-activated phosphors in a collection of applications are also highlighted. We finish the discussion by assessing future prospects for the greater involvement of quantum calculations as a means of accessing a new generation of phosphors. The main thrust here is to identify the critical parameters governing the design of lanthanide-activated phosphors.

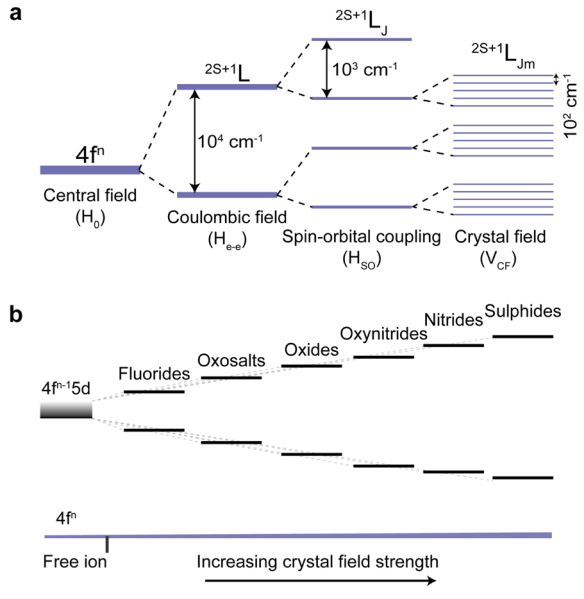


**Figure 3.** (a) Simplified illustration of the effect of Coulombic field, spin−orbital coupling, and crystal field interaction on the splitting of the $[Xe]4f^n$ configuration. (b) Schematic representation showing the degree in the energy splitting of 5d and 4f levels of lanthanides when doped into different classes of inorganic compounds.

## 2. SYNTHETIC STRATEGIES FOR LANTHANIDE-ACTIVATED PHOSPHORS

The preparation of deliberately designed, high-quality lanthanide-activated phosphors not only provides on-demand optical materials for many technological applications but also is crucial to understanding the underlying luminescence mechanisms of the phosphors.[33−35] The luminescence properties of these phosphors with respect to emission and excitation wavelengths, quantum yield, and lifetime are strongly affected by a set of factors, such as phosphor crystallinity, interatomic bond length, the coordination number of the activators, as well as defect concentration in the host lattices.[3,36−38] Subtle changes in experimental conditions can lead to substantial variations in the luminescence properties of the phosphors. In this section, we begin with a summary of the approaches currently used for


DOI: 10.1021/acs.chemrev.6b00691
Chem. Rev. XXXX, XXX, XXX−XXX

preparing lanthanide-activated bulk phosphors, followed by discussions on emerging methods that offer easy access to their nanosized counterparts.

## 2.1. Synthesis of Bulk Phosphors

The bulk phosphors described here are those luminescent crystalline materials with an averaged grain size of several micrometers. Investigations on the synthesis and characterization of phosphors possessing 4f-5d optical transitions can be traced back to 1970's, when Blasse, Bril, and others observed blue light emission from $Ce^{3+}$- and $Eu^{2+}$-activated phosphors upon ultraviolet excitation.[39−41] The combination of these blue-emitting phosphors with green- and red-emitting phosphors originating from intraconfigurational optical transitions within $Tb^{3+}$ and $Eu^{3+}$ ions allows the development of white lamps displaying superior properties to halophosphate-based fluorescent lamps. Indeed, the past few decades have witnessed an exponential growth in synthetic strategies for lanthanide-activated phosphors with predesignated optical properties and crystal structures.[42−44] The majority of these methods, including the solid-state reaction, combustion technique, sol−gel processing, hydrothermal treatment, coprecipitation approach, microwave-assisted synthesis, and mechanochemical route, are summarized in Table 1.

**2.1.1. Solid-State Reaction.** The solid-state reaction is a conventional but robust method for exploring the preparation of high-quality lanthanide-activated phosphors. It generally involves chemical reactions at relatively high temperatures between powder-form precursors. In some cases, a small amount of fluxing agents, such as $H_3BO_3$ or LiF, is added into the mixture to facilitate crystal growth and grain formation. The synthetic temperatures highly depend on the chemical reactivity of the starting materials and the bonding nature of the host lattices. For example, high reaction temperatures (>1500 °C) are required for the generation of corresponding aluminate and nitride phases due to the chemical inertness of $Al_2O_3$ and $Si_3N_4$.[45−47] In contrast, the synthesis of lanthanide-activated phosphates can be realized at much lower temperatures (~1000 °C) as a result of higher reactivity of the precursors to phosphates.[48−50] It is important to stress that most of the phosphors, such as aluminates, phosphates, and silicates, require a sintering process under a reductive atmosphere to prevent sample decomposition or oxidization. This condition leads to designable chemical reduction of $Eu^{3+}$ to $Eu^{2+}$ or prevents the oxidation of $Ce^{3+}$. The final products thus have the ability to emit tunable luminescence from blue to red depending on the nature of the host lattices.[51−54]

The high-temperature sintering may not only promote the formation of highly crystalline phases of phosphors but also lead to a gradual increase in defect concentration with the extension of reaction time. The thermal defects in the forms of cation and anion vacancies, as well as cation interstitials, can participate in the storage of excitation energy, which can be gradually released as photons upon thermal activation. Such a phenomenon is known as afterglow luminescence.[36,55] A case in point is the observation of blue and green long persistent phosphorescence from $CaAl_2O_4:Eu^{2+},Nd^{3+}$ and $SrAl_2O_4:Eu^{2+},Dy^{3+}$, respectively.[56,57] But in the past few years, it has become evident that despite its attractiveness, the solid-state reaction has an intrinsic limitation associated with the need for a long sintering time to improve homogeneity and yield a phosphor with high quantum efficiency. To prevent the formation of inhomogeneous grain boundaries, the starting

**Table 1. Comparison of Reported Strategies for the Preparation of Lanthanide-Activated Bulk Phosphors**

| strategies | host materials | activators | $T$ (°C) | remarks |
|---|---|---|---|---|
| solid-state reaction | β-YFS,[80] $Li_2SrSiO_4$,[81] $Ca_2F_2Si_2O_7$,[82] $LiBaPO_4$,[58] $Ba_4Gd_3Na_3(PO_4)_6F_2$,[83] $K_2Al_2B_2O_7$,[84] $Ca_2Sr(PO_4)_2$,[59] $Sr_4OCl_6$,[85] $Sr_9Mg_{1.5}(PO_4)_7$,[86] $SrSi_2O_2N_2$,[87] $CaAlSiN_3$,[88] $Sr_3Si_2O_4N_2$,[89] $(Lu,Y)_3Al_5O_{12}$,[90] $Y_3Sc_2Ga_{3-x}Al_xO_{12}$,[91] α-$Ca_{1.65}Sr_{0.35}SiO_4$,[92,93] $K_2Ba_2Si_{16}O_{40}$,[94] $Ba_2Ln(BO_3)_2Cl$ (Ln = Y, Gd and Lu),[95] β-NaSrBO$_3$,[96] $Ca_9Y(PO_4)_7$,[97] $Ca_2Al_3O_6F$,[98] $CaZr_4(PO_4)_6$,[50] LaOCl,[99] $BaSi_2N_{10}$,[100] $Sr_5(PO_4)_2(SiO_4)_3$,[101] $CaSrAl_2SiO_7$,[102] $CaAl_2Si_2O_8$,[103] and $Sr_3SiO_5$[104] | $Ce^{3+}$ and $Eu^{2+}$ | >1000[a] | robust and useful for preparing high-efficiency phosphors; time-consuming and need for a reducing atmosphere;[b] hard to control exact stoichiometry in certain cases; products with relatively large crystallites/low surface area |
| combustion technique | $Li_2SrSiO_4$,[81] $MAl_2O_4$: (M = Sr, Ba, Ca)[63−66,105,106] $BaMgAl_{10}O_{17}$,[61,107,108] $Sr_4Al_{14}O_{25}$,[62,109] $SrB_4O_7$,[110] $Sr_2SiO_4$,[111] and $Ba_3MgSi_2O_8$[112] | $Ce^{3+}$ and $Eu^{2+}$ | <1000 | effective for rapidly producing fine and homogeneous powders;[c] exothermic with a high heat release rate and possibly explosive |
| sol−gel processing | $Ca_8La_2(PO_4)_6O_2$,[67] $SrMgAl_2SiO_7$,[68] $Sr_2MgSi_2O_7$,[69] $CaMgSi_2O_6$,[70] $Sr_2MgSiO_5$,[71] $Ba_2SiO_4$,[72] $LiSrPO_4$,[73] $Ca_xSr_{1-x}Al_2O_4$,[74] $SrAl_2O_4$,[75,76] and $Sr_3B_2O_6$[77] | $Ce^{3+}$ and $Eu^{2+}$ | <1000 | useful routes for preparing metal oxide and silicate phosphors; high purity and homogeneity achievable at room temperature; requirement of chelating reagents and repeated thermal treatment in some cases |
| hydro(solvo)thermal treatment | $Sr_5(PO_4)_3Cl$,[113,114] $SiO_2$−$SrAl_2Si_2O_8$,[115d] $SrAl_2O_4$,[116] $KMgF_3$,[117] and $Ba_xSi_yO_z$[118] | $Ce^{3+}$ and $Eu^{2+}$ | <300 | facile control over particle size, morphology, and doping composition; likely the requirement of chelating agents or surfactants and an extra step of thermal treatment |
| coprecipitation approach | ZnS,[119,120] $K_2Ca_2(SO_4)_3$,[121] and $CaAl_2O_4$[34] | $Ce^{3+}$ and $Eu^{2+}$ | >1000 | limited by the need for host matrices with a low solubility and thermal treatment for improved emission intensity; difficult in controlling particle size and morphology |
| microwave-assisted synthesis | $Y(Lu)_3Al_5O_{12}$,[122] $Sr_3Al_2O_6$,[123,124] and $Ba_2Mg(BO_3)_2$[125] | $Ce^{3+}$ and $Eu^{2+}$ | <1000 | fast synthesis and low-energy consumption; high homogeneity and crystallinity; debatable mechanism on thermal microwave effects |
| mechanochemical route | Ca-α-SiAlON,[126] $Al_{10}O_3N_8$,[127] and $BaFBr$[128] | $Eu^{2+}$ | room temp. | large-scale synthesis with generally poor crystallinity and high density of surface defects; constrained by the need for high-temperature annealing steps |

[a]The reaction temperature used for the solid-state reaction depends on the reactivity of the raw materials and the chemical bonding within the host lattices. [b]The reducing atmosphere usually comprises hydrogen (5−25%) and nitrogen (or argon; 95−75%) gases. [c]In the case of low phosphor crystallinity, an extra calcination step at temperatures above 1000 °C is needed. [d]The samples have a core−shell morphology.



DOI: 10.1021/acs.chemrev.6b00691
Chem. Rev. XXXX, XXX, XXX−XXX

precursors in some cases are required to be pretreated at a relatively low temperature (~500−600 °C), followed by thorough grinding and then successive rounds of sintering at higher temperatures (>1000 °C).[58,59]

**2.1.2. Combustion Technique.** The combustion technique,[60] which relies on a thermodynamic concept of complexation and dispersion with rapid heating, is a fast method for the preparation of lanthanide-activated phosphors (Figure 4). It

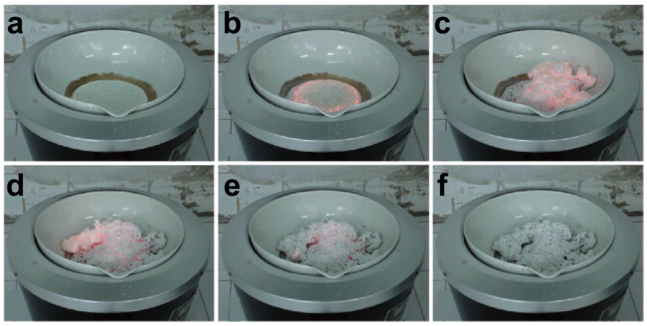


**Figure 4.** (a−f) Photographs showing a typical combustion reaction of $Ca(NO_3)_2$, $Al(NO_3)_3$, and $\beta$-alanine. Note that the fast reaction between $\beta$-alanine and $Ca(NO_3)_2$ triggers an exothermic combustion characterized by the appearance of a red incandescence. Adapted with permission from ref 60. Copyright 2009 Elsevier B. V.

usually makes use of a self-sustaining exothermic reaction between the starting materials at the onset of the reaction. The raw precursors mainly include nitrate salts of various cations and urea (or hexamine, ammonium, glycine, and citric acid), which function as the oxidant and fuel, respectively. The metal nitrates mainly include $Zn(NO_3)_2{\cdot}6H_2O$, $Mg(NO_3)_2{\cdot}6H_2O$, $Al(NO_3)_3{\cdot}9H_2O$, $Eu(NO_3)_3$, and $(NH_4)_2Ce(NO_3)_6$. In principle, the reaction of the nitrates with a fuel can provide enough heat for the formation of crystalline phases. However, as the exothermic reaction lasts only for a few minutes, a subsequent heat treatment at high temperatures in some instances is necessary to foster the crystallinity of the phosphors in order for improving their emission efficiency.

Apart from direct mixing in the solid state, the metal salts and fueling agents for combustion can be dissolved in an aqueous solution followed by solvent evaporation and recrystallization. The solution-based route affords very high levels of chemical homogeneity in the solution. A subsequent decomposition of the homogeneous mixture is likely to result in a uniform distribution of luminescent centers.[61,62] Notably, the burst gas generation during the synthesis can effectively limit interparticle contact and thus provide fine-grained control over powdery products. The gas released from the combustion process has the ability to reduce $Eu^{3+}$ to $Eu^{2+}$.[63−66] Despite the ease of preparing $Eu^{2+}$-doped phosphors, the combustion technique is limited to the preparation of host matrices for aluminates and silicates due to the lack of suitable precursors for other host lattices. On a separate note, experimental conditions, including the ignition temperature, the oxidizer-to-fuel ratio, and the chemical composition of the precursors, should be carefully optimized to prevent the occurrence of explosion or the production of toxic gases. This is also true to prevent the oxidation of $Ce^{3+}$ to $Ce^{4+}$.

**2.1.3. Sol−Gel Processing.** Over the past decade there has been a steady growth of interest in the sol−gel processing of molecular lanthanide compounds for inorganic phosphors.[67−77] The term sol−gel processing refers to a transformation in which solid particles suspended in a liquid (a sol) agglomerate to form a three-dimensional network extending throughout the liquid (a gel) through polycondensation reactions of molecular precursors.[78,79] In the sol−gel process, the precursors typically consist of a metal or metalloid element stabilized by various ligands. The choice of the liquid is mainly determined by the nature of the precursor. For instance, a solution of nitric acid is often employed to dissolve metal oxides, whereas organic solvents are commonly used to give rise to metal alkoxides with perhaps the most thoroughly studied example being the tetraethyl orthosilicate (TEOS), $Si(OC_2H_5)_4$. Aging of the precursor solutions at an appropriate temperature (<100 °C) leads to gradual evaporation of the solvent and the ensuing formation of a continuous solid skeleton made of a molecular substance with extended macroscopic dimensions. The substance is said to be a gel. A xerogel is likely to form upon further drying by completely removing the liquid phase of the gel.

Alternatively, gelation can be realized via polyesterification reactions between chelating agents (e.g., citric acid) and cross-linking agents (e.g., ethylene glycol) at elevated temperatures (>100 °C). High-temperature post-treatment is usually needed to decompose the preformed gel precursors and afford phosphors with high phase purity and crystallinity. The detailed calcination conditions are, for the most part, determined by the nature of the starting precursors as well as the composition of the phosphors. For example, doping of $Eu^{2+}$ ions into $Ba_2SiO_4$, $SrAl_2O_4$, and $Sr_3B_2O_6$ host lattices requires reactions to be carried out under reducing conditions for the reduction of $Eu^{3+}$ to $Eu^{2+}$ in the gel, by analogy with the synthesis of $Eu^{2+}$-doped phosphors through solid-state reactions.[72,75−77]

**2.1.4. Hydro(Solvo)thermal Treatment.** Hydro(solvo)-thermal treatment is a wet-chemistry strategy widely adopted for preparing phosphors with controlled particle size, shape, and doping composition. This method benefits from high vapor pressures generated by heating of the reaction mixture in a sealed vessel, best known as the autoclave, at temperatures above the boiling point of the solvents.[129] These special synthetic conditions significantly affect the diffusion behaviors of the starting materials as well as the way single nanoclusters coalesce, which could be very different under normal atmospheric conditions. This means that lanthanide-activated phosphors with high purity and homogeneity can be achieved under such an extraordinary environment.[113−118,130]

A distinct feature of hydro(solvo)thermal treatment is the utilization of chelating ligands to regulate the nucleation kinetics in order to control the growth of the particles during synthesis and prevent the aggregation of the phosphors in solutions. The chelating ligands bound to the phosphor surface can also impart the phosphors with a versatile function for bioconjugation and immobilization. However, given the fact that the capping ligands are likely to consume the excitation energy through molecular vibration and result in nonradiative deactivation of the excited lanthanides, the decrease in the luminescence intensity of the phosphors can be expected. Another obvious limitation of the hydro(solvo)thermal method is imposed by the use of Teflon-lined autoclaves, typically with a maximum operating temperature of 300 °C. As a side note, an extra step of thermal treatment in a reducing environment is preferable to in situ chemical reduction for the preparation of $Eu^{2+}$-activated phosphors.[131,132]


DOI: 10.1021/acs.chemrev.6b00691
Chem. Rev. XXXX, XXX, XXX−XXX

**2.1.5. Coprecipitation Approach.** The coprecipitation approach has been considered as one of the most convenient strategies for the synthesis of lanthanide-activated phosphors. In a typical procedure, solutions of metal precursors are first prepared either using suitable metal salts or by dissolution of metal oxides in an acidic solution. Thereafter, these solutions are mixed in predetermined concentration ratios to induce local supersaturation, primary nucleation, and subsequent stages of crystallization. Above a critical size, the phosphor precursors with narrow size distribution can precipitate out of the solution. One limitation associated with this method is that the host materials should have a low solubility in the chosen solvent to facilitate the process of precipitation.[120,121] The phosphor precursors are then collected by centrifugation. Finally, the collected precipitates are subjected to annealing at high temperatures (>1000 °C) to boost crystallinity. For the synthesis of $Eu^{2+}$-activated phosphors, it is a general consensus to carry out the annealing step under a reducing environment.[34]

In the absence of reagents for regulating reaction kinetics, it would be difficult to control the growth of phosphor precursors. In effect, this deficiency makes it difficult to exert control over the size and morphology of the phosphors. In addition, the cations making up the host lattice usually exhibit a different reactivity from dopant ions, and hence one would expect a small discrepancy between predicted and observed values for doping concentration. The difference in the reactivity of the precursors may also lead to an inhomogeneous distribution of lanthanide dopants.

**2.1.6. Microwave-Assisted Synthesis.** The term microwave refers to a form of electromagnetic radiation having frequencies between 300 MHz and 300 GHz, corresponding to wavelengths ranging from one meter to one millimeter. The microwave band is well-suited for accelerating chemical reactions as polar solvent molecules or reactants can absorb microwave radiation and generate a large amount of heat by agitating the orientation of the molecules in phase with the external field. This heating effect can be harnessed in the synthesis of lanthanide-activated phosphors. When compared with conventional heating procedures based on convection, the microwave-assisted synthesis is able to heat up the reaction mixture much faster at ambient pressure. Enormous accelerations in reaction time can be achieved. If the reaction is carried out in sealed containers, a reaction that takes several hours under normal reflux conditions can be completed in a matter of minutes.[133]

Seshadri et al. compared the microwave-assisted synthesis of $Ce^{3+}$-doped garnet phosphors with the solid-state synthesis.[122] They found that when using carbon as susceptor, the microwave-assisted synthesis allows a reduction of 95% in preparation time and of 99% in overall energy consumption. Importantly, the resultant phosphors are of single crystalline in nature and show luminescent properties comparable to those prepared by the conventional solid-state reaction. The microwave-assisted synthesis has also been applied to $Eu^{2+}$-activated phosphors, as exemplified by Zhang et al., who have demonstrated the synthesis of $Sr_3Al_2O_6:Eu^{2+}$ afterglow phosphors. In their work, $SrCO_3$, $Al(OH)_3$, and $Eu_2O_3$ were used as starting precursors, while $Fe_2O_3$ and active carbon were added as the heat collector and the reducing agent, respectively.[124] A reducing atmosphere generated upon heating the active carbon plays a crucial role in the chemical reduction of $Eu^{3+}$ to $Eu^{2+}$. It is worth noting that the presence of a susceptor in the reaction is essential to heat the reaction medium to suitable temperatures in favor of the formation of crystalline particles. Otherwise, an extra step of thermal annealing is required to produce luminescent crystalline materials.[125]

**2.1.7. Mechanochemical Method.** A mechanochemical reaction is a unique type of chemical reaction, a process in which the starting materials are activated by the input of mechanical energy.[134,135] This activation is frequently realized with high-energy milling with different work regimes, including compression, shear, and impact. A set of factors, such as the type of the mills, the nature of milling media, ball-to-powder ratios, milling conditions, exert a profound influence on the nature of the as-synthesized lanthanide-activated phosphors.

The mechanochemical method boasts several advantages over other methods. These include simple experimental setup, easy handling and cleaning, and high scalability. For example, industrial planetary mills with continuous operation have the capability to produce products with a rate of 3−5 tons per hour.[135] However, as an intrinsic property, direct mechanochemical synthesis may yield phosphors with poor crystallinity that possess a large number of surface defects. By its very nature, a postannealing procedure is inevitable for improving the quality of the phosphors. As an illustration, Xu and coworkers reported the synthesis of $Eu^{2+}$-doped Ca-$\alpha$-SiAlON phosphors by mechanochemical processing of a stoichiometric mixture of $\beta$-$Si_3N_4$, AlN, $Al_2O_3$, CaO, and $Eu_2O_3$ at room temperature, followed by postannealing at high temperatures (>1600 °C).[126] The homogeneous distribution of $Eu^{2+}$ ions in the phosphor precursor, provided by the milling processing, led to much improved luminescence after thermal treatment. The same strategy has also been successfully applied by the groups of Yin and Riesen to the preparation of $Al_{10}O_3N_8:Eu^{2+}$ and $BaFBr:Eu^{2+}$ phosphors.[127,128]

## 2.2. Synthesis of Nanophosphors

Given the new possibilities for nanoengineering where chemistry, physics, biology, and materials science come into play, considerable efforts have been devoted to the development of advanced techniques for synthesizing lanthanide-activated nanophosphors since the middle 1990's.[35,136,137] Intuitively, nanosized phosphors can be obtained by either post-treatment of their bulk counterparts, using the methods as described above, or through modification of those methods. For example, ultrafine nanophosphors is easily attainable through ball milling of the bulk phosphors obtained by the solid-state reaction, combustion, or sol−gel processing (Figure 5).[52] In addition, introduction of an appropriate amount of surfactants or chelating reagents during the course of hydro(solvo)thermal or microwave-assisted reactions has proven to be an effective technique to limit the growth of phosphors in size. To further control the size distribution, morphology, and surface-defect concentration of the phosphors, a number of advanced techniques, including laser ablation, microemulsion route, template-directed synthesis, and single-precursor thermal decomposition, can be considered. The advantages and disadvantages of these methods are highlighted in this section.

**2.2.1. Laser Ablation.** Laser ablation has the ability to deliver large amounts of energy into confined regions of a material. This ability has proven effective for the production of nanophosphors. In this synthetic method, a bulk phosphor is used as a target and irradiated by an intense laser beam. The high intensity of the laser beam can generate a plasma in liquids and evaporate the target explosively, allowing nanosized


DOI: 10.1021/acs.chemrev.6b00691
Chem. Rev. XXXX, XXX, XXX−XXX

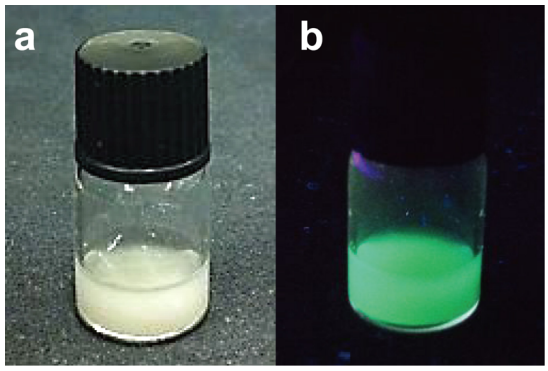


**Figure 5.** Photographs recorded for a colloidal solution of $Ba_2SiO_4:Eu^{2+}$ under different excitation sources. (a) Ambient light exposure. (b) Ultraviolet light irradiation. Note that the nanoparticles were prepared by a combustion reaction of $Ba(NO_3)_2$, $Si(OC_2H_5)_4$, $Eu(NO_3)_3$, $H_3BO_3$, and $NH_2CONH_2$, followed by calcination at 1000 °C for several hours under a hydrogen/argon atmosphere. Adapted from ref 52. Copyright 2013 MDPI.

phosphors to be ejected from the target.[138] The control over the variables of the laser beam, such as wavelength, repetition rate, peak power, and focal spot size, could be useful in forming crystalline nanophosphors with controlled size and morphology.[138] In contrast to the ball milling method, laser ablation has the advantages of immediacy and minimum sample contamination. A drawback of liquid-phase laser ablation for materials processing is the tendency to evoke formation of a large number of surface defects during the course of target bombardment because the laser irradiation can induce changes to the surface chemistry. These surface defects can act as traps for excitation energy and result in decreased emission efficiencies of the nanophosphors.[139]

Park et al. have reported a laser ablation method for the preparation of $Y_3Al_5O_{12}:Ce^{3+}$ in deionized water.[140] In their study, they used a focused pulsed laser (Nd:YAG, 355 nm, repetition rate: 30 Hz, pulse width: 5−7 ns, and maximum output: 300 mW) to irradiate a $YAG:Ce^{3+}$ target. After ablation for 1 h, the size of the ejected phosphors was characterized to be in the range from 5 to 25 nm in diameter. In addition to the intrinsic parameters of laser beams, the nature of the liquid suspension also has a strong influence on controlling the size distribution of the resulting phosphors. For instance, by replacing deionized water with an aqueous solution of 2-[2-(2-methoxyethoxy)ethoxy]acetic acid, Amans and co-workers have demonstrated that the acetic acid derivative could play a role as chelating agent in dictating the synthesis of $Y_3Al_5O_{12}:Ce^{3+}$ nanophosphors with a relatively narrow size distribution.[141] The researchers also speculated that the difference in binding affinity between the chelating agent and the metal ions could lead to phase separation, as supported by the observation of a mixed product of nanoparticles comprising yttrium aluminum perovskite, yttrium aluminum garnet, and corundum aluminum oxide.

**2.2.2. Microemulsion Route.** Microemulsion is a phenomenon which occurs at the interface of two immiscible liquids on addition of surfactants, namely the emulsifier. The microemulsion route for nanophosphor synthesis is developed based on the concept that microdroplets are readily formed upon accumulation of the surfactants at interfaces. Two major classes may be distinguished: oil-in-water and water-in-oil. The choice and amount of the surfactant are crucial in the formation of emulsion and ultimately in controlling the growth process of the phosphors.

As the majority of microemulsion-based synthesis is performed at room temperature or a temperature below 100 °C, this synthetic strategy merely allows one to prepare nanophosphors with low luminescence efficiencies due to the lack of crystallinity. To address this issue, a high-temperature postannealing step is frequently included and, if necessary, carried out in a reducing atmosphere. Lu and co-workers developed an interesting reverse microemulsion for the preparation of $SrAl_2O_4:Eu^{2+},Dy^{3+}$ nanophosphors.[142] In their synthesis, an emulsion was first prepared by mixing an aqueous solution of nitrates with nonpolar cyclohexane and a binary surfactant mixture (polyoxyethylene-10-octylphenyl ether and 1-hexanol). The microemulsion was then slowly added into heated kerosene (180 °C) for water evaporation to yield phosphor precursors. After annealing at 900 °C, the phosphor precursors were converted into highly crystalline and green-emitting $SrAl_2O_4:Eu^{2+},Dy^{3+}$ nanophosphors. In a following paper, the researchers investigated the synthesis of $YBO_3:Ce^{3+}$ phosphors using a similar strategy.[143] They found that the size of the phosphors can be controlled in the range between 90 and 189 nm by varying the volumetric ratio of water to oil.

**2.2.3. Template-Directed Synthesis.** Another approach that is rapidly gaining momentum for controlled synthesis of nanophosphors is template-directed synthesis. Indeed, this method relies on the spatially confined growth of materials in preformed nanoreactors.[144] Arrays of nanophosphors with specific shape and size can be prepared by employing either an active (soft) or restrictive (hard) template. Soft-template processing involves the self-assembly of small molecules or macromolecules to control the process of crystal growth. In this method, the driving forces are usually weak, such as hydrogen bonding, van der Waals force, or electrostatic interaction. On the other hand, hard-template processing typically requires membranes with well-confined voids in the form of channel, pore, or connected hollow space. The hard-template method is generally more complex than its soft-template counterpart because of the requirement for a post-treatment step to remove the template.

Chen and co-workers showed that the soft-template-directed synthesis is viable for preparing a series of necklacelike aluminate phosphors, including $SrAl_2O_4:Eu^{2+},Dy^{3+}$, $BaAl_2O_4:Eu^{2+},Dy^{3+}$, and $CaAl_2O_4:Eu^{2+},Dy^{3+}$.[145] Alternatively, Tan reported the synthesis of $Sr_2MgSi_2O_7:Eu^{2+},Dy^{3+}$ nanotube arrays through the use of anodic alumina oxide (AAO) membranes as the hard template.[146] In this report, two electrochemical cells containing metal precursors and $Na_2SiO_3$ were connected by an AAO template, allowing the starting materials to be diffused into the channels. After completion of the diffusion in 30 h, an extra step of thermal treatment was carried out at 800 °C in a reducing atmosphere to enable the formation of blue-emitting $Sr_2MgSi_2O_7:Eu^{2+},Dy^{3+}$ nanotubes.

Along with morphological control, hard-template-directed synthesis also allows excellent control over the particle size and hierarchical structure in batch crystallization. For example, the Hong group reported the synthesis of monodispersed $BaAl_2O_4:Eu^{2+}$ nanophosphors using $\gamma$-$Al_2O_3$ nanoparticles as the hard template.[147] Another interesting demonstration can be found in the work of Xu and co-workers, who reported the formation of a core−shell structure through an incomplete


DOI: 10.1021/acs.chemrev.6b00691
Chem. Rev. XXXX, XXX, XXX−XXX

removal of the hard template, as exemplified in the synthesis of $SiO_2$@$SrSi_2O_2N_2$:$Eu^{2+}$ oxynitride phosphors.[148]

**2.2.4. Single-Source Precursor Method.** The single-precursor method is based on the thermal decomposition of a single-source molecular precursor at high temperatures to produce lanthanide-activated nanophosphors. By changing the metal center in the molecular precursor complex, a broad range of nanostructures can be prepared with controlled morphology, size, and composition.

An intriguing example was reported by Song et al., who demonstrated the synthesis of SrS:$Ce^{3+}$ phosphors via the thermal decomposition of M-DDTC (M: Sr or Ce, DDTC: *N*,*N*-diethyldithiocarbamate) under a nitrogen atmosphere.[149] It is important to emphasize that the single-source molecular precursor is easily accessible by addition of Na-DDTC to an aqueous solution of the corresponding metal salts. The insoluble molecular precursor is precipitated and further collected by centrifugation. In fact, the thermal decomposition of single precursors in liquid phase can occur in the presence of ligands. Using this strategy, Meijerink and co-workers reported the synthesis of SrS or CaS nanocrystals (~10 nm) doped with $Ce^{3+}$ or $Eu^{2+}$ ions.[150] The molecular precursors, strontium (or calcium) diisopropyldithiocarbamate and cerium (or europium) diethyldithiocarbamate, were quickly injected into a heated solvent of oleylamine. The researchers discovered that an overgrown shell layer in SrS:$Ce^{3+}$ nanophosphors leads to an enhancement in $Ce^{3+}$ emission, accompanied by a slight redshift due to the change in the local environment of the emitting ion.

A recent work has also demonstrated the use of the single-precursor method for constructing nitridosilicate phases. Red-emitting phosphors of $Sr_2Si_5N_8$:$Eu^{2+}$ and $Ba_{1.5}Sr_{0.5}Si_5N_8$:$Eu^{2+}$ have been reported by thermal decomposition of a single-source precursor mixture obtained from a one-pot reaction of corresponding metal amides in the presence of nanocrystalline silicon; this gave a reported efficiency comparable to the crystalline equivalent prepared by conventional high-temperature processing.[151] In general, this synthetic methodology has one big advantage: the molar ratio of the constituent elements in the host lattices could be tuned with relative ease through changes in precursor concentration.

## 3. EMPIRICAL THEORIES OF 4F-5D TRANSITION

### 3.1. General Consideration

A lanthanide-activated solid phosphor is typically composed of lanthanide ions as emitting centers and an inorganic crystalline host material. A given host lattice (A) can affect the energy difference between the lowest $4f^n$ level and the first $4f^{n-1}5d$ level of the lanthanide dopants, as determined by spectroscopic redshift D(A) and Stokes shift ΔS(A).[17] The redshift is defined as the decrease in the 4f-5d excitation energy of the lanthanides when doped into the host lattice (Figure 6). The Stokes shift is related to the parabola offset Δ*R*, induced by lattice relaxation at the excited states as shown in the configurational coordinate diagram (Figure 7). Hence, the energy of 4f-5d absorption can be derived as

$$E_{abs}(A) = E_{free} - D(A) \quad (1)$$

and the energy of 5d-4f emission is given by

$$E_{em}(A) = E_{free} - D(A) - \Delta S(A) \quad (2)$$

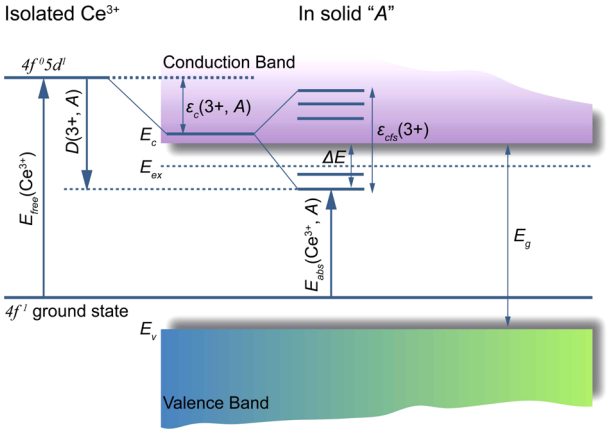


**Figure 6.** Schematic diagram illustrating the influence of the crystalline environment on the 5d energy levels of $Ce^{3+}$ doped in a solid A. The centroid shift $\varepsilon_c$(3+, A), crystal field splitting $\varepsilon_{cfs}$(3+), redshift $D$(3+, A), the lowest 4f-5d transition energy of $Ce^{3+}$ $E_{abs}$($Ce^{3+}$, A), valence band maximum $E_v$ and conduction band minimum $E_c$ of host A, exciton level $E_{ex}$, activation energy Δ$E$ from the lowest 5d level to the bottom of the conduction band are indicated. Adapted with permission from ref 26. Copyright 2013 The ECS Digital Library.

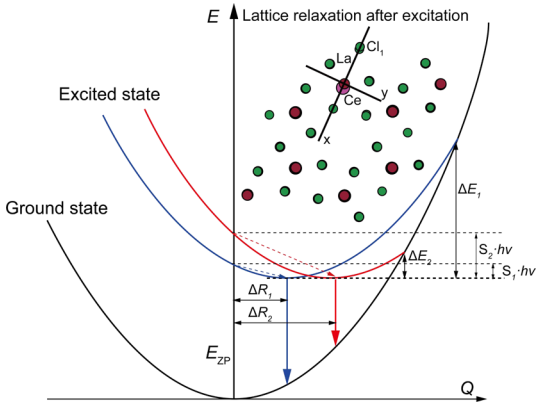


**Figure 7.** Schematic illustration of the configurational coordinate diagram. $E_{ZP}$ is the energy difference between the parabola of the ground state and excited state. $\Delta R_i$ ($i$ = 1, 2) is the parabola offset between the ground and excited states. $S_i$ ($i$ = 1, 2) indicates the Huang–Rhys parameter. $h\nu$ stands for the dominant phonon energy. Δ$E$ is the activation energy associated with thermal quenching. The blue and red parabola curves represent two excited configurations with different parabola offset. Note that a small parabola offset leads to a decrease in Stokes shift and increase in activation energy. The inset shows the atomic displacement observed in a $Ce^{3+}$-doped $LaCl_3$ supercell after relaxation at the lowest 5d state. Adapted with permission from ref 226. Copyright 2007 American Physical Society.

where in both equations $E_{free}$ is a constant with a value close to the 4f-5d transition energy of nondoped lanthanide ions.

A thorough work pertaining to the redshift in over 300 different $Ce^{3+}$-doped inorganic compounds has been presented by Dorenbos et al. using phenomenological data.[152] As shown in Figure 6, the spectroscopic redshift is mainly determined by two factors: centroid shift and crystal field splitting. For instance, one could unravel the redshift D(A) value of $Ce^{3+}$ embedded in host lattice A according to

$$D(A) = \varepsilon_c(A) + \frac{\varepsilon_{cfs}(A)}{r(A)} - 1890\ cm^{-1} \quad (3)$$



DOI: 10.1021/acs.chemrev.6b00691
Chem. Rev. XXXX, XXX, XXX−XXX

where $\varepsilon_c(A)$ and $\varepsilon_{cfs}(A)$ are the corresponding centroid shift and crystal field splitting of the 5d orbitals. $r(A)$ represents the ratio of the crystal field contributing to the redshift. The value of 1890 $cm^{-1}$ refers to the energy difference between the centroid position and the lowest 5d level ($^3D_{3/2}$) of free $Ce^{3+}$ ions.

### 3.2. Centroid Shift of 5d Orbitals

When lanthanides are doped into a host lattice, the nephelauxetic effect is commonly adopted to explain the observed centroid shift of the 5d levels of the lanthanide ion.[153] Note that the strength of the nephelauxetic effect is positively proportional to the covalency (electron sharing) between the luminescent center and its neighboring anions. For example in oxynitride and nitride compounds doped with $Eu^{2+}$ or $Ce^{3+}$ ions, the increase in the covalency can lead to increased centroid shifts.[154] Qualitatively, one could estimate the centroid shift according to the degree of the nephelauxetic effect, which is given in the order of

$$F^- < Cl^- < Br^- < I^- < O^{2-} < S^{2-} \tag{4}$$

It should be noted that the centroid shift of doped lanthanides may contradict the nephelauxetic effect in some host lattices. For instance, one would expect a green emission from SrO:$Eu^{2+}$ phosphors and a red emission from $Sr_2SiO_4$:$Eu^{2+}$ phosphors because of the larger nephelauxetic effect associated with $Sr_2SiO_4$ host lattice.[17] However, this is not the case here as the $Sr_2SiO_4$ phosphor emits green color. To explain the discrepancy between the theory and experimental results, ligand polarization as proposed by Morrison can be taken into consideration.[155] The unexpected centroid shift in the cases of SrO:$Eu^{2+}$ and $Sr_2SiO_4$:$Eu^{2+}$ phosphors is likely due to the combined effect of covalency and ligand polarization.

On the basis of the covalency model, one may assume that the overlapping integral between the lanthanide ion and $N$ coordinating anions varies exponentially with the metal−ligand distance.[156] Thus, the centroid shift can be estimated from

$$\frac{\varepsilon_1}{N} = \frac{\beta}{N}\sum_{i=1}^{N} e^{-(R_i - 1/2\Delta R)/b} \tag{5}$$

where $\varepsilon_1$ is the centroid shift purely determined by the covalency effect, $R_i$ indicates the distance between metal and ligand $i$, $\Delta R$ is introduced to quantify the lattice relaxation around the lanthanide ions, and $b$ is a suitable value obtained by fitting. The parameter $\beta$ should be taken as a measure of the covalency.

Inspired by the pioneering works of Morrison[155] and Aull and Jenssen,[156] the contribution of the ligand polarization to the centroid shift in first approximation can be deduced as

$$\frac{\varepsilon_2}{N} = \frac{\alpha_i e^2}{4\pi\varepsilon_0}(\langle r^2\rangle_{5d} - \langle r^2\rangle_{4f})\frac{1}{R_{eff}^6} \tag{6}$$

$$\frac{1}{R_{eff}^6} = \frac{1}{N}\sum_{i=1}^{N}\frac{1}{\left(R_i - \frac{1}{2}\Delta R\right)^6} \tag{7}$$

where $\varepsilon_2$ is the centroid shift determined through the ligand polarization model and $\alpha_i$ indicates the polarizability of ligand $i$ located at a distance of $R_i$ to the luminescent center in the unrelaxed lattice. Given the highly intractable nature of the covalency $\beta$, the experimentally validated centroid shift $\varepsilon_c$ is commonly adopted to replace $\varepsilon_2$. Here, the parameter $\alpha_i$ shown in eq 6 is redefined as spectroscopic polarizability $\alpha_{sp}$, since it derives from spectroscopic characterization. The correlation of actual polarizability $\alpha$ with the spectroscopic polarizability $\alpha_{sp}$ can thus be described as

$$\alpha_{sp} = \alpha\left(1 + \frac{\varepsilon_1}{\varepsilon_2}\right) \tag{8}$$

The ligand polarization model has been demonstrated as a decisive tool for evaluating centroid shifts because the spectroscopic polarizability comprises the contributions from both microscopic covalency and macroscopic polarization (eq 8). In addition, the spectroscopic polarizability can be quantitatively correlated to the average electronegativity of the cations ($\chi_{av}$) in the host lattices according to the force constant-based theory[157]

$$\alpha_{sp} = \alpha_0(X) + \frac{b(X)}{\chi_{av}^2} \tag{9}$$

$$\chi_{av} = \frac{\sum_i n_i z_i \chi_i}{\sum_i n_i z_i} \tag{10}$$

where $\alpha_0(X)$ and $b(X)$ are the limiting polarizability and the susceptibility of a given anion $X$, respectively; $n_i$ is the number of type $i$ cations; $z_i$ represents valence charge; and $\chi_i$ is the corresponding electronegativity. The experimental data show that the parameter $\alpha_{sp}$ obtained from the observed centroid shift agrees well with the actual polarizability of the anion. Both polarizabilities have a linear correlation with the inverse square of $\chi_{av}$, suggesting the suitability of $\alpha_{sp}$ as an indicator of the centroid shift.[158] Considering that the anion polarizabilities of the crystals can be deduced from macroscopic properties (e.g., dielectric constant or refractive index), one could estimate the values of spectroscopic polarizability and centroid shift through quantum mechanical calculations.

### 3.3. Crystal Field Splitting of 5d Orbitals

In addition to the centroid shift, the crystal field splitting of 5d orbitals also plays a crucial role in determining the redshift due to the highly susceptible nature of the 5d orbitals. In accordance with the phenomenological data, the type of anion coordination polyhedron around the luminescent center dictates the crystal field splitting. For example, the shape of the coordination polyhedron in $Ce^{3+}$-doped materials can be described using a set of geometric parameters. On the other hand, when combined with the point charge electrostatic model,[159] these geometric parameters can also be used to determine the crystal field parameters $B_q^k$. The values of $k$ and $q$ depend on the site symmetry of the luminescent center. Notably, the crystal field splitting has a close correlation with the parameter $B_0^4$, which can be expressed by[159]

$$B_0^4 = f(R)\Theta_0^4 \tag{11}$$

$$\Theta_0^4 = p + \frac{3n}{8} + \frac{m}{4}(35\cos^4\theta_{pr} - 30\cos^2\theta_{pr} + 3) \tag{12}$$

where $\theta_{pr}$ is the angle between the $2m$ prismatic bond and the $m$-fold axis. The parameters $p$, $m$, and $n$ are defined as the respective axial, prismatic, and equatorial position of the anion. Note that the radial part $f(R)$ describes the size effect of the coordination polyhedron, and the angular part $\Theta_0^4$ characterizes the shape effect of the coordination polyhedron. In light of the


DOI: 10.1021/acs.chemrev.6b00691
Chem. Rev. XXXX, XXX, XXX−XXX

ambiguous relationship between the function $f(R)$ and the crystal field splitting, the radial part of the system is not discussed here. Interestingly, the analysis of $Ce^{3+}$ 5d energy states in response to the change in crystalline environment shows a positive correlation of the angular parameter $\Theta_0^4$ with the crystal field splitting.

Dorenbos argued that the crystal field splitting in the 5d orbital of $Ce^{3+}$ is independent of the centroid shift.[22−24,158] Additionally, the magnitude of the crystal field splitting was said to be largely reliant on coordination geometry rather than the type of anions present. An empirical correlation between the shape of the first anion coordination polyhedron and the crystal field splitting can be derived as

$$\varepsilon_{cfs} = \beta_{poly}^{Q} R_{av}^{-2} \tag{13}$$

$$R_{av} = \frac{1}{N}\sum_{i=1}^{N}(R_i - 0.6\Delta R) \tag{14}$$

where $\beta_{poly}^{Q}$ is a constant determined by the type of the coordination polyhedron and the charge valence of the lanthanide. $R_i$ is the bond length between the luminescence center and its $N$ coordinated anions in the unrelaxed lattice. $\Delta R$ indicates the radius difference between the lanthanide dopant and the host cation. Note that $0.6\Delta R$ represents a pseudorelaxation in bond length. Although the level of the crystal field splitting can be quantified using eqs 12 or 13, this method has a major limitation due to the lack of precise information on lattice structures, especially in situations where a charge compensation induces a large distortion in the vicinity of the luminescent center.

Clearly, eqs 3−14 allow for a qualitative estimation of the centroid shift and the crystal field splitting in lanthanide-activated phosphors by measuring the extracted indicators such as $\alpha_{sp}$ and $\Theta_0^4$. In principle, a larger redshift in the 4f-5d transition of lanthanides embedded in inorganic compounds can be expected when any of the following conditions are met: (i) the interaction between the lanthanide and its neighboring anions becomes more covalent in nature, (ii) the polarizability of the anions in the first coordination sphere is increased, (iii) the anion polyhedron becomes more distorted, and (iv) the size of the site accommodating the lanthanide becomes smaller.

## 4. COMPUTATIONAL METHODOLOGIES

### 4.1. Fundamental Principles

Quantum mechanical methods have attracted considerable attention over the past decade due to their ability to unravel many physical and chemical properties of the materials. By taking advantage of high-performance supercomputers, it is now plausible to include the correlation and relativistic effects in quantum calculations, which is essential for accurately describing lanthanide-doped phosphors. In this section, we will briefly discuss two basic theories, Hartree−Fock (HF) theory and density functional theory (DFT), which have been widely applied for materials design.

In principle, the physical and chemical properties of materials can be explained by solving a time-dependent Schrödinger equation of the many-body system.[160] However, a time-independent Schrödinger equation is adequate for depicting most systems in which time-dependent interactions are absent. The examples presented in this review are all based on the time-independent Schrödinger equation, which can be expressed as

$$\hat{H}\Phi = E\Phi, \quad \hat{H} = \sum_l \frac{\hat{P}_l^2}{2m_l} + \frac{1}{2}\sum_{l\neq l'}\frac{q_l q_{l'}}{|r_l - r_{l'}|} \tag{15}$$

where $E$ is the energy eigenvalue, $\Phi$ is the wave function, $\hat{H}$ is the Hamiltonian operator, $m_l$ is the mass of an electron or nucleus, and $q_l$ represents its charge. $P_l$ and $r_l$ are the kinetic momentum and the spatial coordinate, respectively. Note that the summation runs over all electrons and nuclei in the system.

To solve eq 15, a number of approximations need to be employed. By imposing the Born−Oppenheimer approximation,[161] the wave function of electrons and nuclei can be separated, and hence the Schrödinger equation for electrons in the frozen nuclei is given as

$$\hat{H}\Psi(\{r_j\};\{r_\alpha\}) = \left[-\sum_i \frac{\hbar^2\nabla_i^2}{2m} + \frac{1}{2}\sum_i\sum_{j\neq i}\frac{e^2}{|r_i - r_j|} - \sum_i\sum_\alpha \frac{Z_\alpha e^2}{|r_i - r_\alpha|}\right]\Psi(\{r_j\};\{r_\alpha\}) \tag{16}$$

However, the complexity in electron−electron interactions presents an insurmountable obstacle to solving eq 16.

### 4.2. Hartree−Fock-Based Methods

The Hartree approximation has been proposed to solve the problem of many-electron systems.[162] It assumes that each electron moves in an effective potential that represents the attraction of the nuclei and the average repulsive interactions of other electrons. By employing the product of all one-electron wave function (Figure 8), a set of self-consistent Hartree equations can be derived at the single-particle level. However, this approximation may not be reliable as it does not take into consideration the Pauli principle. A feasible solution for

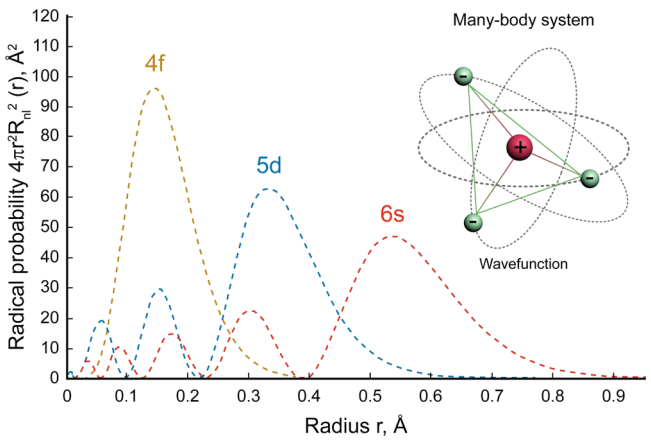


**Figure 8.** Radial parts of the wave functions for Ce (4f, 5d, and 6s) atomic orbitals. The vertical axis represents the probability of finding an electron at a distance of $r$ from the nucleus. The inset depicts complex many-body interactions (electron−electron interactions in solid green lines and electron−nucleus interactions in solid lines with a mixed color of green and rosy). The dotted gray circles indicate the schematic wave function of orbitals. Adapted from ref 168. Copyright 1964 American Chemical Society.



DOI: 10.1021/acs.chemrev.6b00691
Chem. Rev. XXXX, XXX, XXX−XXX

constructing wave functions is to use a Slater determinant of individual orbitals by which the Pauli principle can be satisfied. Such approximation for wave function is known as the Hartree–Fock approximation.[163,164] Hence eq 16 can be rewritten as

$$\varepsilon_i\varphi_i(r) = -\frac{\hbar^2\nabla_i^2}{2m}\varphi_i(r) + V(r)\varphi_i(r) + \varphi_i(r)\int \mathrm{d}r' \sum_{j=1}^{N}\frac{e^2|\varphi_j(r')|^2}{|r-r'|} - \sum_{j=1}^{N}\delta_{xixj}\varphi_i(r)\int \mathrm{d}r'\frac{e^2\varphi_j^*(r')\varphi_i^*(r')}{|r-r'|} \quad (17)$$

The HF approximation can be considered as the simplest form of ab initio approaches in which the electron wave functions can be constructed by adding up all determinants. Note that the electron exchange interaction is considered in the HF equations. However, the electron correlation that describes the instantaneous interaction between electrons is overlooked. This makes the HF approximation unsuited for chemical events dominated by electron correlation interactions.

Currently, three types of HF-based approaches, namely CCSD(T) (coupled-cluster with single, double, and triple perturbative excitations),[165] MP2 (second-order Møller–Plesset perturbation theory),[166] and CASSCF (complete active space self-consistent field)[167] have been widely employed in computational chemistry to study systems having strong electron correlation.[32] Among the three approaches, the CCSD(T) approach provides the best trade-off in accuracy and efficiency by treating triple excitations as perturbation. Considering that the formal scaling with the number of electrons $N$ of CCSD(T) is $N^7$, such calculations are usually limited to small- or medium-sized systems, and supercomputers with parallel processors are necessary.

An alternative method to include electron correlation is the MP2 method, which takes into consideration electron correlation effects by means of Rayleigh–Schrödinger perturbation theory. By adding the first level of the hierarchy of Møller–Plesset energy levels into the HF model, the total energy of a particular system obtained from MP2 calculation becomes the sum of the HF term and a perturbation correction. The formal scaling of the MP2 method down to $N^5$ allows the calculation to be carried out for systems with a few hundred atoms.

The CASSCF method represents one of the multiconfiguration self-consistent field methods by which the occupied orbital space is divided into two sets of inactive (closed-shell) orbitals and active orbitals. This method enables one to evaluate nondynamic electron correlation by distributing active electrons in all possibilities among the active orbitals. Thus, the CASSCF method covers a full range of configuration interactions that only work for active orbitals. The lack of dynamic correlation energy in the CASSCF method can be overcome by introducing the CASPT2 method[169] that gives a second perturbation estimation of the full configuration energy.

Among the aforementioned HF-based methods, the combined CASSCF/CASPT2 approach has seen wide applications in lanthanide-based systems, such as predicting electronic states of $CeCp_3^+$ and magnetic behavior of lanthanides.[170,171] More importantly, with the addition of the ab initio model potential formalism, the effect of crystal environment on the splitting of 5d orbitals can be derived. For a thorough treatment of the details and the application of specific computational models, the readers are encouraged to follow the work of Barandiarán and Seijo.[25]

### 4.3. Density Functional Theory-Based Methods

In DFT-based methods, the electron density is treated as a basic variable in place of the wave function (Figure 9).[173] For a many-body system, the spatial freedom of electrons can be significantly reduced. According to Hohenberg–Kohn theorems, the electron density contains, in principle, all the information that a many-electron wave function can provide. With the help of Kohn–Sham approximation that introduces the concept of effective potential,[174] the electron-associated Schrödinger equation extracted from the Hohenberg–Kohn theorems can be expressed as

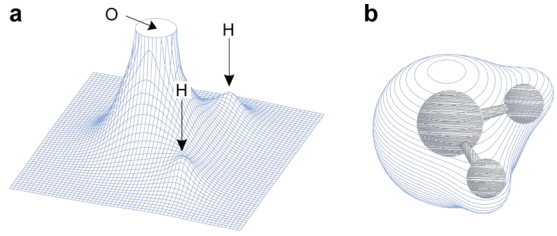


**Figure 9.** Illustration of the electron density distribution of a water molecule. (a) A contour map depicting the values of electron density around the nuclei. Note that height of the peak proportionally represents the value of electron density. (b) Three-dimensional representation of electron density distribution in form of isosurface with an atomic unit of 0.001. Adapted with permission from ref 172. Copyright 2000 Wiley-VCH.

$$\left(-\frac{\hbar^2}{2m}\nabla^2 + V[r,\rho(r)]\right)\psi_i(r) = \varepsilon_i\psi_i(r) \quad (18)$$

where the first and second parts within the left parentheses bracket correspond to the kinetic and potential energies, respectively. $\psi_i(r)$ is the one-electron Kohn–Sham orbital, and $\varepsilon_i$ is the eigenenergy. The potential energy and total density of electrons are given as

$$V[r,\rho] = \frac{\delta}{\delta\rho}(E^{\mathrm{total}}[\rho] - T[\rho]) \quad (19)$$

$$\rho(r) = \sum_i f_i\psi_i^*(r)\psi_i(r) \quad (20)$$

Note that a portion of the potential energy in form of the exchange and correlation interaction is unknown. The local density approximation (LDA)[174,175] and the generalized gradient approximation (GGA)[176,177] can be used to estimate the exchange and correlation interaction. It is important to note that the DFT method is limited to ground-state calculations because Hohenberg–Kohn theorems hold true only for nondegenerate ground states.

Although the standard DFT has been successfully demonstrated in predicting the ground-state electronic properties of materials, the main drawback of LDA/GGA functionals is the significant deviation of bandgap calculations from experimental results. Importantly, LDA/GGA functionals do not suit well for systems with high levels of electron correlation, for example, lanthanide-based materials featuring strongly coupled f electrons. Thus, the important features of the phosphors, including 4f-5d transition energy and the energy gap between


DOI: 10.1021/acs.chemrev.6b00691
Chem. Rev. XXXX, XXX, XXX–XXX

5d level and host conduction band may not be accurately predicted by LDA/GGA functionals.

To address the deficiency of LDA/GGA-based methods, many new functionals have been proposed by including a more precise description of exchange-correlation potential. For example, a newly developed semilocal TB-mBJ functional was put into practice by Tran and Blaha, who utilized kinetic energy density data for the improvement of bandgap calculations.[178] Alternatively, the problem of excessive electron delocalization associated with the LDA/GGA methods can be overcome by introducing a strong intra-atomic Coulombic interaction. This simulation approach is known as the DFT+U method,[179] which enables one to estimate the bandgap within a small error range from the experimental data. To determine the parameter $U$, the experimental results such as bandgap and orbital location have commonly been used as references to ensure a subtle difference between calculations and measured values. It is apparent that the dependence of the empirical parameter $U$ on experimental observation is the major obstacle to its application. Another attractive solution is the use of a hybrid functional that incorporates a portion of exact exchange energy from the HF theory into a local or semilocal density functional. Such a hybrid density functional in the form of PBE0 or HSE06 has been extensively adopted to reduce discrepancy between experiment results and theoretical prediction on bandgap, defect formation, and charge localization in semiconductors and insulators.[180,181]

To probe the excited-state property that is beyond the scope of DFT, a post-DFT method, namely constrained density functional theory, has been proposed to predict the atomic and electronic structures of materials at excited states.[182,183] Note that the constrained DFT is a combination of the standard DFT with additional constraints on the charge density, and it defines an appropriate density functional for systems requiring particular electronic configurations. In addition, the electronic information extracted from DFT calculations can also be utilized as a zero-order solution for many-body perturbation theory within the GW approximation.[184,185] This approach has recently risen to prominence for characterizing the processes of electronic excitation. The combination of the GW approach with the Bethe-Salpeter equation[186] can lead to a quantitative treatment of peak positions, heights, and widths in the absorption and electron energy-loss spectra by taking into account quasi-particle effects and the screened electron−hole interaction.

## 5. DESIGN CRITERIA OF LANTHANIDE-ACTIVATED PHOSPHORS

As described in section 3, host lattices play a significant role in the determination of 5d-4f luminescence features because the 5d orbitals are extremely sensitive to surrounding environment. For instance, nitride hosts are suitable for $Eu^{2+}$- or $Ce^{3+}$-activated phosphors that give rise to emission at long wavelengths as the strong covalency offered by these compounds can produce a large redshift toward 4f-5d transitions.[154] For lanthanide-activated scintillators and persistent phosphors, desirable luminescence features are likely to be obtained in halides,[14,204,205] aluminates, and silicates.[206,207] In addition to 4f-5d transitions, the optical transitions within well-shielded 4f manifolds can also be affected by the local environment. A classic example is revealed in the investigation of hexagonal-phase $NaYF_4$:Yb/Er phosphors that exhibit the most efficient upconversion luminescence as compared to their cubic counterparts and other host materials.[208]

Apart from intrinsic host lattices, lanthanide dopants also need to be considered in the computational model. A typical justification lies in the different optical response from the activators occupying nonequivalent host sites, which leads to multiple emission centers. Note that the difference in the site occupation of the luminescent centers can be ascribed to the substitution of crystallographically independent host cations,[209−211] the distortion of the coordination environment caused by an intentionally introduced codopant,[202,212] and the relaxation of charge-compensating defects.[213] More importantly, the alignment of 4f and 5d levels of lanthanide dopants with respect to host bands is extremely crucial for optical investigations because it can directly affect the occurrence of 5d-4f luminescence and subsequently alter the emission features.[158] Therefore, in the succeeding subsections, we attempt to first discuss the design criteria extracted from the computational cases of intrinsic host lattice then followed by the criteria derived from representative activator-contained examples. These criteria could be useful for evaluating specific characteristics of lanthanide 5d-4f luminescence, including quantum yield, emission color, and decay rate as well as thermal quenching behavior.

### 5.1. Debye Temperature

By virtue of the close correlation of the quantum yield ($\Phi$) with the rigidity of molecules,[214] it seems rational to state that the rigidity of the host lattice could be viewed as an ideal indicator for efficient photoluminescence.[53] In general terms, a large structural rigidity in the host materials should lead to a higher luminescence quantum yield. Unlike in organic phosphors, the identification of structural rigidity in an inorganic crystal is generally difficult to conduct due to its structural anisotropy and the existence of complicated vibrational modes. On the basis of Voigt-Reuss-Hill (VRH) approximations,[215] the rigidity-related elastic parameters such as bulk modulus, shear modulus, Young's modulus, and Poisson ratio can be easily obtained using elastic constants ($C_{ij}$) derived from DFT simulations. However, none of these elastic parameters can describe the degree of rigidity individually because of the versatile structural connectivity of inorganic lattices.

Given the positive correlation of the rigidity with the Debye temperature $\Theta_D$, which is the temperature required to activate the highest energy vibrations in a solid such as diamond and graphite,[216,217] one can infer that the Debye temperature could serve as a useful probe for structural rigidity. Thus, it is reasonable to assume that the Debye temperature could be utilized for qualitatively estimating the quantum yield of the phosphors. On the basis of the quasi-harmonic Debye model,[218,219] the Debye temperature $\Theta_D$, which relies solely on bulk modulus and Poisson ratio, can be extracted from quantum calculations according to the following expressions

$$\Theta_D = \frac{\hbar}{k_B}[6\pi^2 V^{1/2} N]^{1/3} \sqrt{\frac{B_H}{M}} f(\nu) \tag{21}$$

$$f(\nu) = \left\{ 3\left[ 2\left( \frac{2}{3}\frac{1+\nu}{1-2\nu} \right)^{3/2} + \left( \frac{1}{3}\frac{1+\nu}{1-\nu} \right)^{3/2} \right]^{-1} \right\}^{1/3} \tag{22}$$

where $\hbar$ is the Plank constant, $k_B$ is the Boltzmann constant, $M$ is the molecular mass of the unit cell, $N$ is the number of atoms



DOI: 10.1021/acs.chemrev.6b00691
Chem. Rev. XXXX, XXX, XXX−XXX

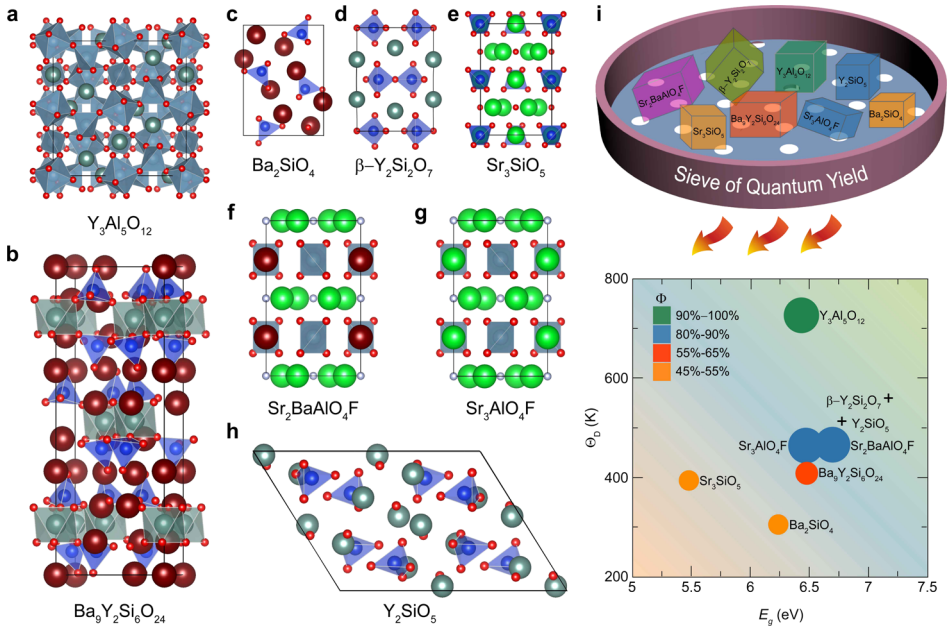


**Figure 10.** (a–h) Crystal structures of eight different inorganic hosts: $Y_3Al_5O_{12}$, $Ba_9Y_2Si_6O_{24}$, $Ba_2SiO_4$, $\beta$-$Y_2Si_2O_7$, $Sr_3SiO_5$, $Sr_2BaAlO_4F$, $Sr_3AlO_4F$, and $Y_2SiO_5$. (i) A schematic showing the capability of using Debye temperature and bandgap parameters for identifying $Ce^{3+}$-activated high-efficiency phosphors. The circle size and color are corresponding to the experimentally measured photoluminescent quantum yield and emission color, respectively. Note that "+" indicates that the quantum yield of such phosphors has yet been reported. Adapted from ref 187. Copyright 2013 American Chemical Society.

in the unit cell, $B_H$ is the bulk modulus of the crystal, $V$ is the unit cell volume, and $\upsilon$ is the Poisson ratio.

Over a decade ago, the Debye temperature $\Theta_D$ obtained in YAG host materials using the elastic constant has been revealed to be in reasonable agreement with that measured by photoluminescence spectroscopy.[220] Despite the marginal overestimation in absolute values, the Debye temperature derived from elastic constants can also capture the trend of weak dependence of $\Theta_D$ on $Er^{3+}$ concentration that reconciles with experimental spectroscopic data. Moreover, the experimental data confirm that there is a positive correlation between $\Theta_D$ and the quantum yield of a YAG host doped with $Er^{3+}$. As all elastic constants can be determined by direct computation, DFT calculations of Debye temperature could provide an effective way to screen vast databases of known inorganic structures in search for materials with a high probability of producing high quantum yield. A representative case is shown in Figure 10, in which eight well-characterized oxide and oxyfluoride systems, including $Ce^{3+}$-activated YAG, were employed for validation.[187] It was found that a high $\Theta_D$ value of the host indeed inclines to lead to a high quantum yield of luminescence. For example, the YAG host lattice has the highest $\Theta_D$ (726 K) among the eight systems under study, consistent with the highest quantum yield (90%) experimentally obtained for $Ce^{3+}$-doped YAG phosphors (Figure 10).[188] Moreover, the high external quantum yield (70%) of $Ce^{3+}$-doped barium yttrium borate materials ($Ba_2Y_5B_5O_{17}$:$Ce^{3+}$) can also be attributed to the high rigidity of the host lattice.[221] In addition to metal oxides and their derivatives, such a close $\Theta_D$–$\Phi$ correlation has been observed in lanthanide-activated nitride phosphors. For example, the temperature-dependent measurements of quantum yield have demonstrated that the remarkable thermal stability of the luminescence observed in $La_{2.82}Ce_{0.18}Si_6N_{11}$ phosphor also originates from its highly rigid lattice, which is in line with its high Debye temperature.[195] This criterion appears to be valuable when no competing mechanism affects the performance of the 5d-4f luminescence, such as thermally activated escape of electrons from the $d$ orbital to the host conduction band.[222]

The capacity of the Debye temperature for predicting quantum yield does not deteriorate even under elevated temperatures, as confirmed by Seshadri and co-workers.[223] In their study, all calculated Debye temperatures of the $Sr_xBa_{2-x}SiO_4$ hosts agree well with the experimental values obtained from neutron scattering data and low-temperature heat capacity measurements. While the Debye temperature is a useful proxy for quantum yield prediction, it remains questionable whether this direct correlation holds true for phosphors with different luminescence mechanisms. In principle, a high Debye temperature means inaccessible high-energy phonon modes, resulting in a decreased number of nonradiative relaxation channels. Hence, it is reasonable to assume that such a temperature parameter can work for a broad spectrum of phosphors as the process of nonradiative relaxation is mainly responsible for luminescence quenching.

Most recently, Debye temperatures of different mixed oxides, including $Ba_2SiO_4$, $BaAl_2O_4$, $SrAl_2O_4$, and $Y_2SiO_5$, have been revisited using DFT calculations and three different experimental techniques.[189] The resulting data shed light on the noticeable difference in rigidity between the average and local crystal structures. This study suggested that the DFT-derived Debye temperature can only be considered as an indicator for the average structural rigidity, whereas the effect of local structural rigidity around emitting ions on the optical properties of the materials should be examined. Some abnormities contradicting the strong $\Theta_D$–$\Phi$ correlation have been reported in $Ca_7Mg(SiO_4)_4$ and $CaMg(SiO_3)_2$ hosts when doped with $Eu^{2+}$ activator.[196] These phosphors with high Debye temperatures exhibited low quantum yields (<30%). Similar anomalous phenomena have also been observed in other


DOI: 10.1021/acs.chemrev.6b00691
Chem. Rev. XXXX, XXX, XXX–XXX

Table 2. Calculated Bandgap and Debye Temperature for A Collection of Host Lattices (Note That the Quantum Yields Experimentally Observed for $Ce^{3+}$- and $Eu^{2+}$-Activated Phosphors Are Also Compiled for Comparison)

| host | crystal system | space group | bandgap $E_g$ (eV) | Debye temperature $\Theta_D$ (K) | emitter and quantum yield $\Phi$ | refs |
|---|---|---|---|---|---|---|
| $Y_3Al_5O_{12}$ | cubic | $Ia\bar{3}d$ | 6.43 | 726 | $Ce^{3+}$, 90% | 187 and 188 |
| $SrAl_2O_4$ | monoclinic | $P2_1$ | 4.479 | 475 | $Eu^{2+}$, 65% | 189−191 |
| $Ba_9Y_2Si_6O_{24}$ | rhombohedral | $R\bar{3}$ | 6.48 | 409 | $Ce^{3+}$, 57% | 187 and 192 |
| $Sr_3AlO_4F$ | tetragonal | $I4/mcm$ | 6.47 | 465 | $Ce^{3+}$, 85% | 187 and 193 |
| $Sr_2BaAlO_4F$ | tetragonal | $I4/mcm$ | 6.7 | 466 | $Ce^{3+}$, 83% | 187 and 194 |
| $Sr_3SiO_5$ | tetragonal | $P4/ncc$ | 5.48 | 394 | $Ce^{3+}$, 52% | 104 and 187 |
| $La_3Si_6N_{11}$ | tetragonal | $P4bm$ | >4 | 660 | $Ce^{3+}$, 100% | 195 |
| $Ba_2SiO_4$ | orthorhombic | Pmcn | 4.27 | 307 | $Eu^{2+}$, 84% | 196−198 |
| $\alpha$-$Sr_2SiO_4$ | orthorhombic | Pmab | 4.489 | 360 | $Eu^{2+}$, 44% | 196 and 199 |
| $\beta$-$Sr_2SiO_4$ | monoclinic | $P2_1/c$ | 4.106 | 428 | $Eu^{2+}$, 75% | 196 and 199 |
| $X_1$-$Y_2SiO_5$ | monoclinic | $P2_1/c$ | 4.73 | 491 | $Ce^{3+}$, 36% | 196 and 200 |
| $X_2$-$Y_2SiO_5$ | monoclinic | $C2/c$ | 4.77 | 512 | $Ce^{3+}$, 45% | 196 and 200 |
| $Ca_7Mg(SiO_4)_4$ | orthorhombic | $Pnn2$ | 6.86 | 601 | $Eu^{2+}$, 30% | 196 |
| $CaMg(SiO_3)_2$ | monoclinic | $C2/c$ | 7.08 | 665 | $Eu^{2+}$, 5% | 196 |
| $SrSiN_2$ | monoclinic | $P2_1/c$ | 2.95 | 375 | $Eu^{2+}$, 25% | 201 and 202 |
| $BaSiN_2$ | orthorhombic | $Cmca$ | 2.92 | 360 | $Eu^{2+}$, 40% | 201 and 202 |
| $CaAlSiN_3$ | orthorhombic | $Cmc2_1$ | 3.40 | 787 | $Eu^{2+}$, 95% | 201 and 203 |

lanthanide-activated phosphors (Table 2), indicating that the screening for highly luminescent phosphors should not solely rest on the analysis of Debye temperature.

Precise color-tuning of phosphors is of paramount importance for various applications requiring a particular emission wavelength.[224] As shown in eq 2, the Stokes shift (related to $\Delta R$ in Figure 7) can affect the 5d-4f emission wavelength. Considering that the Stokes shift varies from nearly zero to a value as large as 1.3 eV,[152,225] the host effect on 5d-4f emission color through changes in Stokes shift also merits special consideration. Although the Stokes shift of $Ce^{3+}$ and $Pr^{3+}$ in ionic compounds has been directly estimated using both HF- and DFT-based approaches,[213,226,227] the extensive lattice relaxation at $4f^{n-1}5d$ excited states, such as the obvious atomic rearrangement of $Ce^{3+}$-doped $LaCl_3$ (Figure 7, inset),[226] poses a significant constraint to these methods.

According to the work of Gettinger and Heeger on *p*-phenylene-vinylene derivatives, a reduction in Stokes shift with increased rigidity of the molecular backbone was observed.[228] In light of the inversely proportional correlation between the Stokes shift and the rigidity of the host lattice,[33] one may also qualitatively speculate that those rigid host structures tend to have small Stokes shifts, thereby giving rise to emissions with short wavelengths.[229] Thus, there is a general consensus that the qualitative estimation on the Stokes shift can be achieved by measuring Debye temperature. To the best of our knowledge, there is no research work in the literature that reports the direct correlation of Stokes shift with Debye temperature. On the contrary, Mikami and co-workers argued that the Stokes shift may not necessarily be linked to the structural rigidity because they recently found that despite having a higher Debye temperature (489 K), $Ba_3Si_6O_9N_4$ doped with $Eu^{2+}$ has a larger Stokes shift ($3.2 \times 10^3$ $cm^{-1}$) than its $Ba_3Si_6O_{12}N_2$ equivalent ($2.8 \times 10^3$ $cm^{-1}$).[230] Such inconsistency may arise from inadequate consideration of the local structural effect on Debye temperature.[189]

Additionally, the bandgap of host materials needs to be taken into consideration because a crystal with high rigidity is usually associated with a small bandgap. As such, the effect of thermal quenching may be increased due to instantaneous concentration of electrons in the conduction band. On the other hand, one should note that the covalency of host lattices has been widely recognized as the major contributor to the redshift of emission wavelength. The increase in covalency should result in highly rigid atomic configurations, as observed in $La_3Si_6N_{11}$ and $SrLiAl_3N_4$ host lattices.[195,231] Therefore, it is generally accepted that the Debye temperature could also serve as an indicator of the redshift in 4f-5d transitions. However, no direct connection between these two parameters has been reported from the perspective of quantum computations.

### 5.2. Dielectric Constant

To explore the underlying mechanisms governing the 5d-4f emission of lanthanide-activated phosphors, a compromise needs to be made among different selection criteria. For example, a material with a large bandgap has the tendency to minimize the interaction between the material's valence/conduction bands and 4f/5d orbitals at the expense of lattice rigidity. In the previous section, we have discussed the association of Debye temperature with quantum efficiency and Stokes shift. In this section, we will emphasize the central role of dielectric constant in predicting the degree of the centroid shift as defined in section 3.

The concept of nephelauxetic effects has been recognized as a major contributor to the centroid shift in the form of covalency ($\varepsilon_1$ as denoted in eq 5) that describes the degree of electron sharing between the emitter and its neighboring anions. Thus, one may expect that $Ce^{3+}$-activated oxynitrides or nitrides emit light at a wavelength longer than that of fluorides due to the presence of a strong covalency in the former. At present, the amount of covalency can be quantitatively calculated by means of single-particle theories, for example, through standard Hartree−Fock-linear combination of atomic orbitals method.[232] It can also be estimated qualitatively by DFT-based analysis of the charge distribution[233] and the orbital hybridization between the emitter and the ligands.[231]

However, an abnormal behavior that contradicts the covalency criterion has been experimentally detected in SrO:Eu and $Sr_2SiO_4$:Eu phosphors, as described in section 3.2. Such an abnormity is likely due to lack of contributions from the dynamic polarizability of anions to both the centroid shift and the crystal field splitting. By applying configuration interaction as an extension of the basic Hartree−Fock LCAO


DOI: 10.1021/acs.chemrev.6b00691
Chem. Rev. XXXX, XXX, XXX−XXX

approach, Andriessen et al. showed that the effect of the dynamic polarizability on the centroid shift ($\varepsilon_2$ as denoted in eq 6) can be validated, thereby enabling one to determine the $\varepsilon_1$ and $\varepsilon_2$ parameters separately.[232]

To construct atomic orbitals, a large basis set is required to evaluate covalency and dynamic polarizability, making the calculations of the centroid shift extremely complex.[232] Considering that spectroscopic polarizability $\alpha_{sp}$ can be treated as an ideal indicator of the centroid shift, one can simply estimate the value of $\alpha_{sp}$ using the dielectric constant. This hypothesis is made possible because Dorenbos observed a subtle distinction between the experimentally extracted spectroscopic polarizability and the polarizability derived from dielectric constant.[157] A commonly used quantum mechanical method for measuring dielectric constants is implemented by combining DFT with Density Functional Perturbation Theory (DFPT),[234] which has been successfully applied to several inorganic host materials, including yttrium oxysulfide,[235] lanthanide borogermanate,[236] and lanthanide sesquioxides and oxysulfides.[237,238] Mikami et al. have demonstrated that the anomalous emission observed in $Eu^{2+}$-doped oxynitride/nitride phosphors can be better explained by the calculated dielectric constants instead of the covalency.[239] Specifically, the researchers obtained the calculated dielectric tensors (3.76, 3.76, 3.76), (3.33, 3.33, 3.35), and (3.16, 3.28, 3.18) for SrO, $Sr_3SiO_5$, and $Sr_2SiO_4$, respectively, which is in line with the centroid shift in the order of $\varepsilon_c(SrO) > \varepsilon_c(Sr_3SiO_5) > \varepsilon_c(Sr_2SiO_4)$.

The Gladstone-Dale relation suggests that the dielectric constants of multinary oxides can be qualitatively derived from the summation of the contribution from constituent binary oxides.[26,240] For instance, $Sr_3SiO_5$ and $Sr_2SiO_4$ can be decomposed into $3SrO + SiO_2$ and $2SrO + SiO_2$, respectively. It is thus reasonable to infer that $Sr_3SiO_5$ with a higher ratio of $SrO/SiO_2$ should have a larger dielectric constant because the $O^{2-}$ anion in SrO is more polarizable than achievable in $SiO_2$.[26] However, such an empirical relation is not applicable to multinary compounds comprising nitrides. With the help of quantum calculations, the dielectric constants of nitridosilicates can rather be easily obtained. A marked centroid shift could be anticipated in nitrides with a large dielectric constant.[239,241] Indeed, the calculated average dielectric constants of $La_3Si_6N_{11}$ (5.46) and $LaSi_3N_5$ (5.32) are supportive of the longer wavelength emission experimentally observed for $La_3Si_6N_{11}:Ce^{3+}$, irrespective of the similarities in chemical formula and the coordination number of the emitting ion.[242]

In view of the difference in ionic nature between $O^{2-}$ and $N^{3-}$ anions, one may manipulate the centroid shift of lanthanide 4f-5d transition by varying the composition ratio of $O^{2-}$ to $N^{3-}$ in the host matrix. As illustrated by Mikami et al. in the investigation of nitridoaluminosilicate and silicon oxynitride, the calculated refractive indices follow the order of $CaAlSiN_3$ (2.17) > $0.75CaAlSiON_3$-$0.25Si_2N_2O$ (2.08) > $Si_2N_2O$ (1.83), which can be seen as an indication of what is predicted for the trend of the centroid shift.[241] The dielectric constant can be approximately estimated from the square of the refractive index. For rare-earth oxysulfides, one may expect large centroid shifts when compared to their corresponding oxides. It is important to note that rare-earth oxysulfides with small bandgaps are subject to luminescence quenching since the f or d orbitals of a given dopant may rest at the energy levels below the valence band maximum or above the conduction band minimum.[243]

Although the knowledge of dielectric constants of host materials is useful in predicting luminescence behavior, it should be noted that the nitrides with similar dielectric constants do not necessarily emit similar colors. For instance, $Sr_2Si_5N_8$:Eu is a well-known red phosphor for white-LEDs, whereas $BaSi_7N_{10}$:Eu and AlN:Eu,Si emit blue-green light.[244,245] Another anomalous observation is the emission of a series of Eu-doped compounds with a basic formula of $Ba_3Si_6O_{15-3x}N_{2x}$ ($x$ = 0, 1, 2, and 3).[26] The calculated refractive indices of these compounds follow the sequence of $BaSi_2O_5$ (1.65) < $Ba_3Si_6O_{12}N_2$ (1.76) < $Ba_3Si_6O_9N_4$ (1.81) < $BaSi_2O_2N_2$ (1.9 or 1.95), whereas the order of the emitted wavelength is $Ba_3Si_6O_9N_4$ (480 nm) < $BaSi_2O_2N_2$ (494 nm) < $BaSi_2O_5$ (500 nm) < $Ba_3Si_6O_{12}N_2$ (530 nm). Therefore, caution needs to be taken when using the dielectric constant to evaluate the effect of the host on the emission color. This is understandable because the centroid shift is not the only factor contributing to the 4f-5d transition energies, as already discussed in section 3.

### 5.3. Geometry of First Coordination Polyhedron

As stated in the previous two sections, Debye temperature and dielectric constant can be used as suitable proxies to measure the quantum yield and centroid shift of a phosphor, but the calculations involving these two descriptors often fail to consider the specific interactions between the lanthanide emitters and their surroundings. This deficiency prompts the need for discovering additional descriptors with characteristics that are largely influenced by the local environment.

By inspection of empirical eqs 5−14, it is apparent that the size and shape of the anion polyhedron around the luminescent center play a crucial role in determining the centroid shift and crystal field splitting. Let us consider the cases of $Sr_2Si_5N_8$:Eu, $BaSi_7N_{10}$:Eu, and AlN:Eu,Si phosphors in an effort to understand how the geometry of the coordination polyhedron can be used to give a quick qualitative prediction toward the shift of emission wavelength.[26] By examining the local geometries of the crystal structure, it was found that the coordination number of $Eu^{2+}$ dopant varies from 12 to 13 as evidenced in the hosts of AlN and $BaSi_7N_{10}$. The availability of large coordination numbers makes the $Eu^{2+}$ ion loosely coordinated, leading to a small centroid shift and crystal field splitting. The decreased redshift observed for $BaSi_7N_{10}$ and AlN hosts is responsible for the emission of $Eu^{2+}$ at a wavelength shorter than that in the $Sr_2Si_5N_8$ host lattice. Meijerink and co-workers systematically studied the emission of $Eu^{2+}$ ions embedded in a series of strontium aluminates.[246] Similarly, they found that the increase in coordination number indeed leads to a reduced centroid shift and crystal field splitting and ultimately a short emission wavelength. This perspective also holds true for $Y_3Al_{5-x}Ga_xO_{12}$:Ce phosphors in which the blue shifts in both excitation and emission spectra originate from a less distorted coordination polyhedron around $Ce^{3+}$.[247] Conversely, an increased distortion of the coordination polyhedron usually boosts a redshift in the 4f-5d transition, as exemplified in $Y_3Al_{5-x}(Mg,Si)_xO_{12}$:Ce and $CaSrSi_{1-x}Al_xO_4$:Ce,Li phosphors.[248,249] The accurate prediction of luminescent properties, however, remains challenging, largely due to the hypothetic nature of the lattice relaxation parameter $\Delta R$ presented in eqs 5, 7, and 14.

The splitting of the lanthanide's 5d orbitals highly depends on the coordination environment. For example, within an octahedral coordination $O_h$ geometry, the 5d orbitals can split into double degenerate high-energy levels and triple degenerate



DOI: 10.1021/acs.chemrev.6b00691
Chem. Rev. XXXX, XXX, XXX−XXX

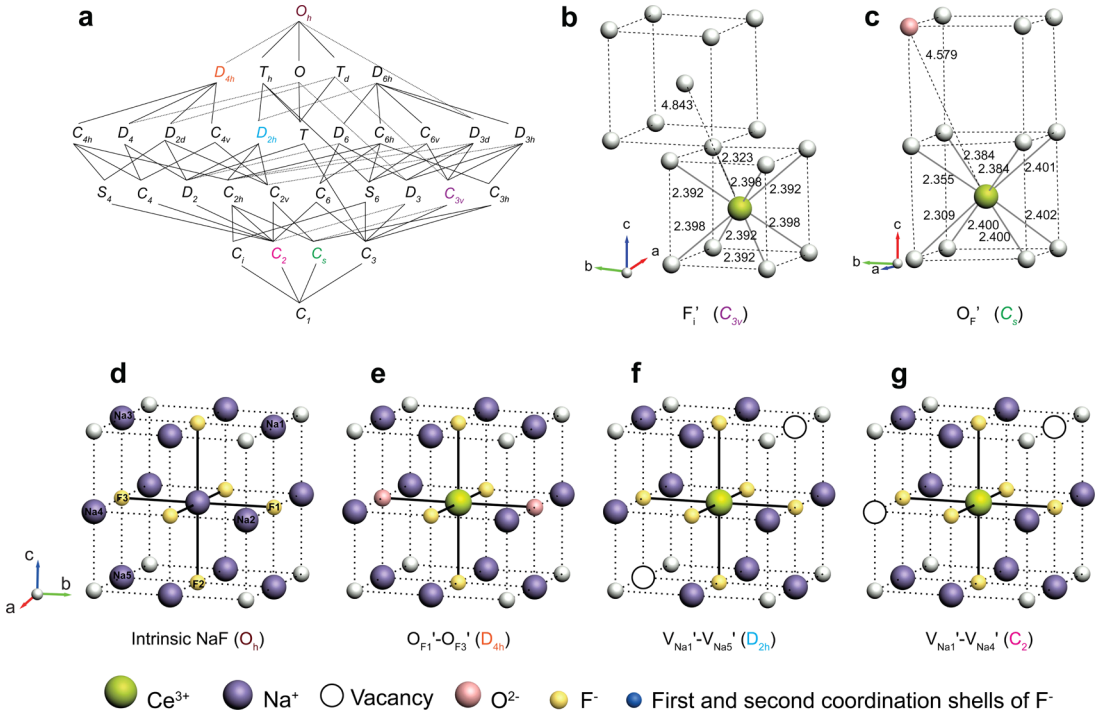


**Figure 11.** (a) Branching rules of the 32 point groups. (b and c) Optimized local structures of $Ce^{3+}$ when incorporated into $CaF_2$ with local charge compensations of interstitial $F^-$ and substituent $O_F$. (d) Local structure of $Na^+$ in NaF lattice. (e–g) Schematic illustrations of local structures of $Ce^{3+}$ when incorporated into the NaF lattice. The charge compensation is achieved by two sets of $O_F$ substitutions or $V_{Na}$ vacancies. All point group symmetries of the optimized structures are highlighted in (a). Adapted with permission from ref 7. Copyright 2013 Royal Society of Chemistry. Adapted from ref 258. Copyright 2012 American Chemical Society.

low-energy levels, while a reversed energy alignment is typically observed for a tetrahedral coordination $T_d$ geometry (Figure 11a). Extended X-ray absorption fine structure (EXAFS) experiments on $Ce^{3+}$-doped garnets are able to provide two Ce–O distances,[250] but the details of full structural parameters of the $CeO_8$ moiety remain unclear. It is thus a general practice for researchers to investigate optical properties of a material on the basis of undoped crystal structures. As such, the structural distortion induced by the mismatch in ionic radius between the dopant and the host cation is usually not included. It is plausible that the host geometry can be used to predict the redshift of 4f-5d transitions because the dopant-induced lattice expansion is normally smaller than the mismatch in ionic radii. Moreover, the dopant-induced lattice distortion has limited impact on lattice structures located beyond the first and second coordination spheres.

However, for a large collection of $Ce^{3+}$-doped garnets, HF-based calculations indicate that particular deformations of a $CeO_8$ moiety with a $D_2$ symmetry such as bond compression and bending in complexes with octahedral ($O_h$) and square planar ($D_{4h}$) symmetries can lead to a redshift of the lowest 4f-5d transition with different contributions from centroid energy and crystal field splitting.[251,252] Meanwhile, the unrelaxed host effect defined as the interactions between $Ce^{3+}$ and the unrelaxed second and more distant coordination shells also gives a redshift of the first 4f-5d transition, in which the centroid shift energy dominates the redshift in all garnets and the crystal field splitting can either increase or reduce the redshift depending on the nature of the garnet.[252] Clearly, one could observe that both the pseudodistortion around emitters and the interactions between emitters and distant neighbors indeed affect the redshift of the transitions. Thus, the lattice relaxation should not be ignored when studying the luminescent properties of phosphors, especially in the materials possessing significant lattice distortions.

In contrast to the experimental techniques and the HF-based approach, DFT simulations can efficiently provide more accurate geometric information on pure and doped crystals.[27] Mikami presented an overview of the capability of DFT simulations to predict both ordered and disordered crystal structures of pure *oxo*-nitridoalumino silicates hosts. These include $CaAlSiN_3$ and its derivatives, $Sr_3Al_{10-x}Si_{1+x}O_{20-x}N_x$ and $Ba_3Si_6O_{12}N_2$.[26] All optimized lattice structures and the experimental crystallographic parameters are within an acceptable error range of 1–2%. Muñoz-García and Seijo used DFT simulations to probe the atomic structure or crystal lattice of materials with the replacement of a single $Y^{3+}$ ion by $Ce^{3+}$ or $La^{3+}$ or with the substitution of two $Y^{3+}$ ions by a pair of $Ce^{3+}$/$La^{3+}$ ions.[253] The as-simulated Ce–O distances are in good agreement with the EXAFS results.[250]

In 2005, Stephan et al. demonstrated the inclusion of local lattice relaxation as a prerequisite for establishing a good agreement between the calculated 4f-5d excitation energies and the experimental data within an error of 0.3 eV.[257] Large lattice distortions in coordination environment could be expected when the formation of defect clusters induced by charge compensators begins to take place. For example, an excess positive charge is generated when $Ce^{3+}$ replaces $Ca^{2+}$ in $CaF_2$ crystals. The charge imbalance can be neutralized by adding an interstitial fluoride $F_i'$ (Figure 11b) or substituting a fluoride anion with oxygen $O_F'$ (Figure 11c). Note that both charge compensators will lead to a lowered symmetry around $Ce^{3+}$.[258] The calculated structure of Ce–F(O) clusters can be employed to estimate the contribution of centroid shift and crystal field


DOI: 10.1021/acs.chemrev.6b00691
Chem. Rev. XXXX, XXX, XXX–XXX

splitting to the redshift of the 4f-5d transition. Furthermore, these specific defect clusters are also helpful for the assignment of experimentally observed absorption spectra as different coordination environments would give rise to different transition intensity patterns.[259] Additionally, $Ce^{3+}$-doped NaF has also been studied in understanding the effect of the locally distorted coordination polyhedron on spectral profiles.[260] It is obvious that oxygen substitutions and sodium vacancies serving as charge compensators can introduce large lattice distortion, driving the original $O_h$-symmetry of $Na^+$ to lower site symmetries such as $D_{4h}$, $D_{2h}$, and $C_2$ (Figure 11, panels d–g). The formation of defect clusters caused by spontaneous charge compensation is almost inevitable and hardly controllable while intentional addition of codopants provides a common approach to varying the local structure of luminescent centers for controlled color modulation.[12,261,262]

By first employing DFT for structure optimization, the HF-based method can provide more accurate estimates of the effects of local environments on the absorption and emission energies of 4f-5d transitions. In studying $CaF_2:Ce^{3+}$ and $NaF:Ce^{3+}$ phosphors,[258,260] Ning and co-workers ascribed the experimental observation of 4f-5d excitation bands to the effect of local lattice relaxation. In a separate work on $LiYF_4:Ce^{3+}$ phosphor, Watanabe and Ogasawara also demonstrated that by considering the lattice relaxation the experimental spectrum can be well-reproduced by the calculation.[263] In their study, a symmetry reduction from $S_4$ to $C_2$ was observed. In partial fulfillment of the previous work on the first neighborhood effect[251] and the host embedding effect,[252] Seijo and co-workers recently investigated the influence of lattice relaxation on the lowest 4f-5d transition of $Ce^{3+}$ embedded in several garnet materials by combining DFT simulations with the ab initio embedded cluster approach.[264] Their calculations show that the effect of lattice relaxation occurring either locally or over a relatively long distance can contribute to the blue shift of the 4f-5d transition. This study provided further insights on how different substitution sites can be identified. The same approach has also been used to unravel the mechanism governing the shift of transition energies in $YGA:Ce^{3+}$ phosphors codoped with $La^{3+}$ or $Ga^{3+}$.[254,255] Despite the added anisotropic lattice expansion around the $Ce^{3+}$ ions caused by codoping of $La^{3+}$ or $Ga^{3+}$, the observed redshift in the lowest $Ce^{3+}$ 4f-5d transition in $YGA:La^{3+},Ce^{3+}$ phosphor is believed to arise jointly from the $La^{3+}$-reinforced ligand field effect on 5d orbitals and the decreased energy gap between the energy centroid of the 5d and 4f configurations, whereas the blue shift of the transition upon $Ga^{3+}$ codoping stems solely from the reduction in the ligand splitting of the 5d orbitals due to induced lattice distortions.

Recently, geometrical parameters, including the continuous symmetry, the shape measures,[243] and the tetrahedral distortion parameter,[265] have been proposed to represent the deviation of coordination distortion from an ideal polyhedron shape. For a cubic $Y_2O_3$ host, large values in the shape and symmetry operation measures indicate a large distortion of $Y^{3+}$ ions from their ideal octahedral positions, as manifested by lowered symmetry operations of $C_2$ and $C_3$ point groups. Although quantum calculations have clearly sketched an unambiguous picture of coordination distortion around the luminescent center, the general trend of how the distortion influences optical properties remains unexplored. Up to now, the corroboration between the coordination distortion and the redshift of 4f-5d transitions is randomly chosen and only analyzed on a case-by-case basis. To systematically study the effect of atomic structures on luminescence, modern HF- and DFT-based methods can be combined with empirical models. By adopting the DFT-optimized geometry parameters and the Dorenbos model, Jia et al. reported the investigations of $LaSi_3N_5:Ce^{3+}$ and $La_3Si_6N_{11}:Ce^{3+}$ phosphors with calculated redshifts in good agreement with the experimental results.[266]

The HF- and DFT-based approaches can also be combined with conventional crystal field (CF) models to calculate the absorption and emission spectra of lanthanides adopting $4f^{n-1}5d$ configurations.[267] For example, Burdick and Reid used HF-based methods for estimating the atomic parameters and radial integrals of CF models,[268] which allows an accurate prediction of absorption and emission spectra. Other examples include the utilization of DFT-generated effective potentials for constructing crystal field parameters[269,270] or DFT-based orbital-free embedding formalism for calculating ligand field splitting energies.[271,272] A successful application of the combined DFT-CF method has also been demonstrated in $Ca_2(Al_{1-x}Mg_x)(Al_{1-x}Si_{1+x})O_7:Eu^{2+}$ phosphors, by which the correlation of 5d crystal field splitting of $Eu^{2+}$ with its local environment was clearly revealed.[273]

### 5.4. Energy Level Alignment

In the previous section, we discussed the effect of the coordination geometry of a dopant on emission profiles. By choosing the appropriate geometry of the coordination polyhedron, precise control of activator emission can be achieved. There is also experimental evidence that the Debye temperature and dielectric constant are useful proxies for luminescence assessment. There are situations, however, in which these parameters are of little utility. The major concern, in this regard, is to recognize that not all lanthanides have emission on excitation. If the emission profiles are predictable through energy level and transition intensity calculations then the design of inorganic phosphors will be quite straightforward. In this section, we briefly discuss the absolute position of the 4f and 5d energy levels and their location relative to the energy bands of the host. It is an important study that shows that the emission process, absorption/emission energies, emission bandwidth, and decay rate, as well as thermal quenching behavior of the materials, could be well-rationalized.

**5.4.1. Emission Criteria.** The attempt to explain the origin of luminescence in inorganic phosphors with configurational-coordinate diagram-based models could be dated back to the late 1930's. With the aid of the Mott-Seitz, Seitz, and Dexter-Klick-Russell models, one could determine whether a particular lanthanide ion can be activated or not by examining the distance between the excited and the ground states at equilibrium ($\Delta R$ as shown in Figure 7).[274] A close examination shows that the $\Delta R$ is roughly assumed to be equal to the difference between the orbital distances for electrons around the atomic nucleus. While fairly successful for its implementation, the usefulness of the parameter is diminished by the requirement of a precise and comprehensive assessment of the conditions under which quantitatively predictive results can be obtained.

In the case of scintillators presented in Figure 2, the 4f and 5d levels of doped lanthanides need to be inserted inside the bandgap of the host material in order to trap holes and electrons for efficient radiative emission. By constructing binding energy schemes for more than 1000 different inorganic compounds, Dorenbos has developed a complex empirical


DOI: 10.1021/acs.chemrev.6b00691
Chem. Rev. XXXX, XXX, XXX–XXX

model endowed with considerable predictive power.[158,275] However, access to such comprehensive data requires a tedious process. In addition, the approximation nature of the given model makes it unrealistic for quantitative predictions.

DFT-based ground-state calculations have been regarded as a primary quantum tool because it is a time-efficient way of realizing lattice relaxation and has the ability to provide insight into the electronic structures of materials, especially with regard to the orbital alignment of doped systems. As discussed in section 4.3, the standard DFT simulations usually give underestimated bandgaps and inaccurate or even wrong positions of 4f energy levels due to the intrinsic self-interaction error of the DFT method and the highly correlated nature of the 4f orbitals.[276−279] Such problems can be largely alleviated by utilizing advanced DFT+U and hybrid DFT approaches. For example, pure DFT-GGA calculation derived the 4f-VBM gap, defined as the energy gap between the lowest 4f level and the host valence band maximum, to be 2 eV in a $LaBr_3$:$Ce^{3+}$ system. This result significantly deviates from the experimentally measured 4f-VBM gap of 0.9 ± 0.4 eV. Such a large discrepancy can be diminished using the DFT+U method with $U_{eff}$ = 2.5 eV.[277] For the $\gamma$-$Ca_2SiO_4$:$Ce^{3+}$ phosphor, the occupied 4f states of $Ce^{3+}$ in the presence of $Ce_{Ca}$-$Al_{Si}$ defects were wrongly merged with the conduction band.[278] Upon introduction of a hybrid functional, the positions of the occupied 4f states can be correctly relocated in the bandgap.

Once the specific positions of the 4f and 5d levels relative to the host energy bands are available, one could qualitatively measure the occurrence of the 4f-5d transitions. Recently, a series of research activities have been implemented by Ibrahim and Benco and their co-workers in $LaSi_3N_5$-based phosphors to study the relative energy levels of 4f and 5d orbitals for Ce, Pr, Nd, Pm, Sm, and Eu dopants.[280−283] The calculated 4f energy levels and the experimental data of the dopants with different oxidation states are compiled in Figure 12. The researchers found that the lowest 4f energy levels can locate either above or in close proximity to the host VBM, or deeply embedded in the host valence band. The unoccupied 4f energy levels were found to mostly locate at the bottom of the conduction band. Compared to the well-defined and localized 4f orbitals, the 5d orbitals of lanthanide ions are rather dispersed and highly mixed with the conduction band. On the basis of the energy level diagram displayed in Figure 12, one could only expect the occurrence of 4f-5d transitions in $LaSi_3N_5$:$Ce^{3+}$ phosphor because the 4f orbitals of $Ce^{3+}$ locate well above the VBM. On the contrary, the 4f orbitals of other $Ln^{3+}$ ions are well-localized within the valence band, indicating that charge transfer from p to 4f orbitals is responsible for the electronic transition in $LaSi_3N_5$-based systems.[283] It is plausible that the 5d-4f emission of $LaSi_3N_5$ doped with divalent lanthanides can occur since the occupied 4f orbitals reside in the bandgap. However, the luminescence of $LaSi_3N_5$:$Ln^{2+}$ was not observed experimentally, which could be attributed to the thermal quenching induced by highly destabilized 5d states of the divalent lanthanides.

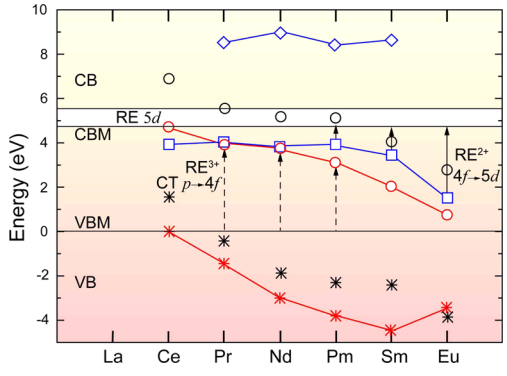


**Figure 12.** Representative energy levels of a series of divalent and trivalent rare-earth (RE) ions when doped in $LaSi_3N_5$ host lattice. * and ○ labels refer to the occupied and unoccupied 4f states of $RE^{3+}$, respectively. □ and ◇ labels refer to the occupied and unoccupied 4f states of $RE^{2+}$, respectively. Note that gray-colored circle and asterisk symbols stand for the experimentally observed 4f ground states. The dashed and solid arrows indicate charge transfer to trivalent lanthanides and f-d transition in divalent lanthanides, respectively. Adapted with permission from ref 283. Copyright 2015 Elsevier B. V.

The existence of the 4f-VBM gap has been identified in an array of $Ce^{3+}$- and $Eu^{2+}$-doped host materials, making them suitable candidates for use as scintillators.[277,284] Interestingly, Watras and co-workers predicted that the 4f-5d transitions in a $KCa(PO_3)_3$ host could take place only within the ultraviolet spectral region when the Ca vacancy-mediated generation of $Eu^{3+}$ occurs.[285] Their band structure calculations suggest the absence of 5d-4f transition of $Eu^{2+}$. Importantly, the theoretical results are consistent with the experimental data, which show the missing of $Eu^{2+}$ emission bands. Therefore, the observed red light in the emission spectrum is most likely due to the 4f-4f transition of $Eu^{3+}$.

As noted earlier, advanced DFT calculations can be used to determine the relative position of 4f energy bands to the host VBM. For more dispersive 5d orbitals, the mapping of their relative position, however, could offer a set of challenges for the method developer. In general, ground-state DFT calculations show high levels of hybridization between the 5d orbital of the lanthanide emitter and the conduction band of the host, even for well-known phosphors. These simulation results are contradictory to the fact that the lowest 5d state of the emitter must rest well below the conduction band to realize the process of emission. This contradiction can be well-clarified by analyzing the electronic structures of excited $4f^{n-1}5d^1$ states with the help of constrained DFT methods.[277,284,286−288] The excited states can be mimicked by manually pumping one 4f electron to the first energy level of 5d orbitals. In $Ce^{3+}$- and $Eu^{2+}$-doped phosphors, removal of one 4f electron can shift the lowest 5d energy level within the bandgap due to hole−electron attractions. Consequently, the lowest 5d energy level resides well below the host CBM, which is necessary for achieving 5d-4f emission.

Although the constrained DFT methods enable one to qualitatively derive 5d-CBM gaps, they are not workable when the 5d-CBM gaps are close to zero or the 5d states resonate with the host CBM. Hence a parameter needs to be developed to examine the relative position of the first excited 5d state. As an illustration, Canning et al. proposed that the degree of the localization in the lowest excited d orbital can be used to investigate the origin of the lowest conduction band, either from a host or a doped emitter (Figure 13).[277,284,289] By considering the bandgap, 4f-VBM gap, and degree of 5d orbital localization, the researchers theoretically and experimentally discovered several bright $Ce^{3+}$- and $Eu^{2+}$-based scintillators when screening for hundreds of targets. The implementation of those key selection criteria is more likely to lead to a significant cut in the production cost of phosphors.

**5.4.2. Emission Redshift.** In addition to the ability to predict the occurrence of 5d-4f luminescence, DFT simulations


DOI: 10.1021/acs.chemrev.6b00691
Chem. Rev. XXXX, XXX, XXX−XXX

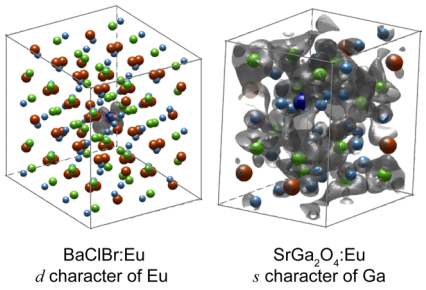


**Figure 13.** Lowest excited 5d state plots of $Eu^{2+}$-doped BaClBr and $SrGa_2O_4$ scintillators. The excited state has a pure d character of Eu for $BaClBr:Eu^{2+}$ compound. The excited state shows significant electron delocalization in the nonluminescent $SrGa_2O_4:Eu^{2+}$ compound with a predominant s character of Ga. Adapted with permission from ref 284. Copyright 2014 American Physical Society.

can also provide the quantitative estimate of 4f-5d transition energies. Schmidt and co-workers reported that the experimentally observed 4f-5d excitation energies linearly depend on the energy difference between the 4f and 5d ground-state orbital energies for a variety of trivalent lanthanide-doped fluorides and oxides.[257] With the help of the fitted parameters, the researchers found that the transition energies obtained at the ground state agree well with the experimental validation[290] or the energy values directly calculated at excited states.[291] In a separate work, Yao et al. investigated lanthanide-doped hexagonal $NaYF_4$ crystals and found that the orbital energies obtained from constrained DFT calculations can be used to predict the 4f-5d transition energies.[292,293] Compared to the calculation at the excited state, the ground-state DFT simulation is a more efficient approach for investigating electronic structures and qualitatively interpreting luminescent behavior of phosphors. By taking $BaO-SiO_2:Eu^{2+}$ phosphors as an example, Hong and co-workers analyzed DFT-calculated band structures of the phosphors with different compositions and found a bandwidth broadening in the 5d state of $Eu^{2+}$ in the order: $Ba_{0.95}Eu_{0.05}Si_2O_5$ (0.771 eV) < $Ba_{0.95}Eu_{0.05}SiO_3$ (0.784 eV) < $Ba_{2.95}Eu_{0.05}SiO_5$ (1.039 eV).[294] Such ordering is congruous with the increase in the wavelength of 5d-4f emission measured for these three phosphors. Most recently, Fang and Biswas examined the luminescence behavior of a collection of halide-hosted phosphors, including $CsBa_2I_5:Eu^{2+}$, $KBa_2I_5:Eu^{2+}$, and $KSr_2I_5:Eu^{2+}$, by DFT calculations.[295] Their calculations on orbital energies and electronic structures suggest that the $Eu^{2+}$ dopants tend to form a sublattice structure only in $Ba^{2+}$-containing hosts. Importantly, the researchers also found that the 4f-CBM gap decreases with increasing $Eu^{2+}$ concentration as a result of the formation of subdomains. This result provides a rational explanation for the redshift of 5d-4f emission experimentally recorded for samples with a high doping concentration of $Eu^{2+}$ (5%).

Considering that the 4f-5d optical transition occurs between the ground and excited states in a given system, one should carefully validate the suitability of the ground-state orbital energy for representing the 4f-5d transition energy. HF-based approaches can be used to calculate the precise energy levels of the 4f and 5d orbitals at excited states. This attribute enables one to further estimate the 4f-5d transition energies, predict absorption and emission spectra, and evaluate the oscillator strength of the 4f-5d transition. $Ce^{3+}$ ion has the simplest form of electron configuration ($4f^1$), and its 4f-5d transition is most studied among all divalent and trivalent lanthanides. As an illustration, the centroid shift of $Ce^{3+}$ in various hosts, including $BaF_2$, $LaAlO_3$, and $LaCl_3$, has been directly evaluated by Andriessen et al. through ab initio cluster calculations at the Hartree−Fock level.[232] Moreover, the researchers pointed out that a good agreement between theoretical and experimental results on the centroid shift of $Ce^{3+}$ can be achieved by including the effects of anion dipole polarization and dynamic correlation during the calculation.[296]

Alternatively, a different ab initio approach, namely ab initio model potential embedded-cluster calculation has also been employed to study the 4f and 5d energy levels of lanthanide emitting ions. Seijo and co-workers used this method to investigate 4f-5d optical transitions occurring in $YAG:Ce^{3+}$, $Lu_2O_3:Pr^{3+}$, $BaF_2:Tb^{3+}$, and $CsCaBr_2:Yb^{2+}$ phosphors.[297−300] In a further attempt to obtain a comprehensive understanding of the 4f-5d transition, the same group calculated the vertical absorption and emission of $(LnCl_6)^{3-}$ clusters (Ln = Ce to Tb) embedded in a cubic elpasolite $Cs_2NaYCl_6$.[301] On the basis of the calculated absorption and emission profiles and relative transition intensities, the researchers are able to assign the experimentally observed absorption and emission lines, directly calculate the Stokes shift, and predict the hidden transitions that cannot be detected using current experimental techniques. As illustrated in Figure 14, the calculated lowest $4f^8$ and $4f^7$5d levels of $Tb^{3+}$ in $BaF_2$ host are qualitatively in line with the experimental validation.

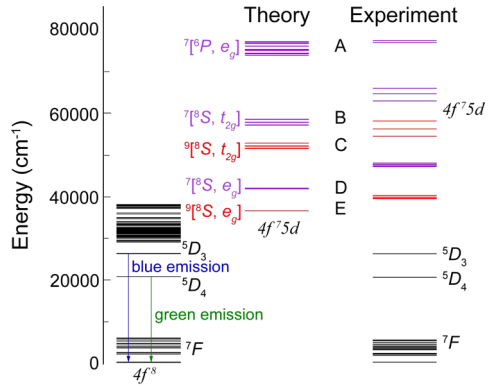


**Figure 14.** Schematic calculated energy diagram of the lowest $4f^8$ and $4f^7$5d levels of $BaF_2:Tb^{3+}$ using wave function-based ab initio embedded cluster method and experimentally detected excitation and emission spectra. Adapted with permission from ref 299. Copyright 2014 Elsevier B. V.

As discussed in section 5.3, DFT-based ground state calculations can effectively reach the genuine lattice relaxation of doped materials, thus proving qualitatively estimation on 4f-5d transitions through the size and the shape of coordination environment around the emitters. To directly probe the optical properties such as redshift and Stokes shift, HF-based methods are commonly suggested to include the effect of lattice relaxation by adopting DFT-optimized crystal structures as calculation input. This is because the HF-based approaches become extremely resource-demanding when the effects of lattice relaxation are considered.[251,302] By employing the combined DFT-HF method, one could expect a better agreement between the calculated transition profiles and the experimental data. For instance, by optimizing the crystal lattice of Ce-doped $La_2CaB_{10}O_{19}$, the experimentally observed J and K bands have been successfully assigned to the lowest $4f_1$-$5d_1$


DOI: 10.1021/acs.chemrev.6b00691
Chem. Rev. XXXX, XXX, XXX−XXX

transition of $Ce_{La}$ and the lowest $4f_1$-$5d_1$ transition of $Ce_{Ca}$ with a charge compensator of $Na_{Ca}$ (Figure 15), respectively.[276]

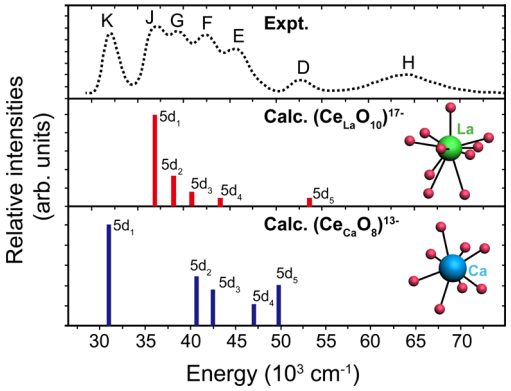


**Figure 15.** Calculated $4f_1$-$5d_i$ ($i$ = 1−5) transition energies and relative oscillator strengths for $Ce^{3+}$ ions doped in $La_2CaB_{10}O_{19}$. Experimental excitation spectrum is shown in the top panel for comparison. Insets shown in middle and bottom panels correspond to the coordination polyhedra of $Ce^{3+}$ ions occupying La and Ca sites, respectively. Adapted from ref 276. Copyright 2013 American Chemical Society.

Additionally, small differences between the 4f-5d transition in $Y_3Al_5O_{12}$:$Ce^{3+}$ and $Lu_3Al_5O_{12}$:$Ce^{3+}$ phosphors can be directly calculated by including the structural relaxation.[264] In this study, the maximum energy differences could reach 180 and 1895 $cm^{-1}$ for the 4f and 5d orbitals when the calculations use unrelaxed[297] and optimized[254] structures of $(CeO_8)^{13-}$ clusters. Importantly, the different local structures induced by the presence of charge compensators, codopants, or antisite defects can be easily retrieved through DFT-based structure optimization, rendering more accurate energy levels of $Ce^{3+}$ ion (Table 3).[254−256,258,260] Moreover, the calculated 4f-$5d_i$ ($i$ = 1−5) transition energies can be used to unambiguously distinguish the contribution of the centroid shift and the crystal field splitting to the total redshift, shedding light on the underlying mechanism of the experimentally observed variation in emission wavelength. It is believed that the directly calculated transition energies can provide new insights into the manipulation in the wavelength of emissions.[258,276,279,303,304]

**5.4.3. Emission Bandwidth.** Unlike f-f transitions, the 5d-4f transitions are characterized by broad absorption and emission spectroscopic bands as a result of the large difference in the susceptibility of 4f and 5d orbitals to the surrounding environment. The width of the spectral bands, defined as full-width at half-maximum (fwhm), is typical of 100 nm for $Ce^{3+}$-activated phosphors. Recent advances in phosphors with broad- or narrow-band emissions make them potential contenders in electronics and lighting markets for applications as displays, fluorescent lighting, and white LEDs.[305] For example, the fabrication of single-phosphor-[306] and multiphosphor-based[19] white-LEDs with high color rendition requires the emission bandwidth to be substantially broad and narrow, respectively.

To manipulate the bandwidth of a particular emission, an important issue relating to the factors that affect bandwidth needs to be addressed first. In accordance with the configuration coordinate diagram as shown in Figure 7, broad spectral bands can be ascribed to the large difference in energy states at equilibrium and also the high probability of radiative transitions between numerous vibrational levels.[274] Clearly, the narrow-band emission is achievable if the two factors can be mitigated. Because the local structural relaxation around the emitter and the level of high-energy vibration are closely associated with the rigidity of the host lattice, the use of a highly rigid host structure may yield phosphors with desired narrow-band emission. Very recently, $Eu^{2+}$-activated $Sr[LiAl_3N_4]$ red-emitting phosphor has been demonstrated by Pust et al. to be a promising candidate for the next generation of white-LEDs because of its narrow-band emission centered at 650 nm (fwhm: ∼ 50 nm).[19] The authors linked the narrow-band emission to the limited freedom for geometrical relaxation at

**Table 3. Relative Energies and Energy Shifts Calculated for Many-Electron Levels of the Ce's $4f^1$, $5d^1$, and $6s^1$ Configurations in YAG:$Ce_Y$ in the Absence and Presence of Codoped $La^{3+}$, $Ga^{3+}$, or Antisite Defects (AD)[254−256a]**

| host | $Ce_Y$ | | $Ce_Y$,$La_Y$ | | | $Ce_Y$,$Ga_{Al}$(Oct) | | $Ce_Y$,$Ga_{Al}$(Tet) | | $Ce_Y$,1AD | | $Ce_Y$,2AD | |
|---|---|---|---|---|---|---|---|---|---|---|---|---|---|
| | $D_2$ | energy | $C_1$ | energy | shift | energy | shift | energy | shift | energy | shift | energy | shift |
| $4f^1$ levels | $^2B_2$ | 0 | $^2A$ | 0 | – | 0 | – | 0 | – | 0 | 0 | 0 | 0 |
| | $^2B_3$ | 38 | $2^2A$ | 62 | 24 | 51 | 13 | 64 | 26 | 63 | 26 | 36 | −2 |
| | $^2B_1$ | 202 | $3^2A$ | 248 | 46 | 244 | 42 | 231 | 29 | 159 | −43 | 271 | 69 |
| | $^2A$ | 416 | $4^2A$ | 490 | 74 | 421 | 5 | 409 | −7 | 433 | 17 | 461 | 45 |
| | $^2B_1$ | 443 | $5^2A$ | 541 | 98 | 473 | 30 | 445 | 2 | 488 | 45 | 492 | 49 |
| | $^2B_2$ | 516 | $6^2A$ | 620 | 104 | 524 | 8 | 529 | 13 | 571 | 55 | 624 | 108 |
| | $^2B_3$ | 2419 | $7^2A$ | 2422 | 4 | 2420 | 1 | 2390 | −29 | 2316 | −102 | 2320 | −98 |
| $5d^1$ levels | $^2A$ | 23853 | $8^2A$ | 23633 | −220 | 23927 | 74 | 24064 | 211 | 24314 | 461 | 24645 | 792 |
| | $^2B_3$ | 30169 | $9^2A$ | 30756 | 586 | 30247 | 76 | 30278 | 109 | 31093 | 923 | 30505 | 336 |
| | $^2A$ | 48112 | $10^2A$ | 47659 | −454 | 48328 | 216 | 47884 | −228 | 47904 | −208 | 46695 | −1418 |
| | $^2B_2$ | 48700 | $11^2A$ | 49267 | 567 | 49080 | 380 | 48990 | 290 | 49318 | 618 | 47379 | −1321 |
| | $^2B_1$ | 52221 | $12^2A$ | 51376 | −845 | 51555 | −666 | 51719 | −502 | 50218 | −2003 | 52497 | 276 |
| $6S^1$ level | $^2A$ | 61214 | $13^2A$ | 63110 | 1896 | 61957 | 743 | 61627 | 413 | 58984 | −2230 | 64190 | 2976 |
| $\Delta E_{centroid}$ ($4f^1 \rightarrow 5d^1$) | – | 40035 | – | 39912 | −123 | 40037 | 2 | 40006 | −29 | 39994 | −41 | 39743 | −292 |
| $\Delta E_{ligand\text{-}field}$ ($1^2A \rightarrow 8^2A$) | – | −16182 | – | −16279 | −97 | −16110 | 72 | −15942 | 240 | −15680 | 502 | −15098 | 1084 |
| $\Delta E_{LF}$ ($4f^1 - 1^2A$) | – | 576 | – | 626 | 50 | 591 | 15 | 581 | 5 | 576 | 0 | 601 | 25 |
| $\Delta E_{LF}$ ($5d^1 - 8^2A$) | – | 16758 | – | 16905 | 147 | 16701 | −57 | 16523 | −235 | 16256 | −502 | 15699 | −1059 |

[a]Note that the MS-CASPT2 calculations are based on a $(CeO_8Al_2O_4)^{15-}$-embedded cluster without the effect of spin−orbital coupling. The unit for all numbers is in per centimeter.



DOI: 10.1021/acs.chemrev.6b00691
Chem. Rev. XXXX, XXX, XXX−XXX

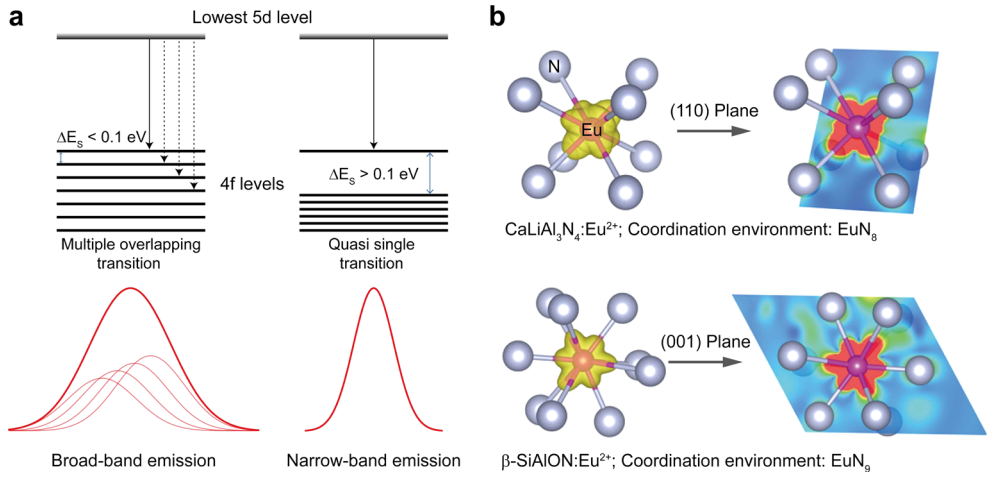


**Figure 16.** (a) Schematic illustration showing the correlation of emission bandwidth with the 4f substate splitting of $Eu^{2+}$. $\Delta E_S$ represents the energy splitting between the two highest $4f^7$ levels of $Eu^{2+}$. (b) Three dimensional and cross-sectional partial charge density calculated for the highest 4f band of $Eu^{2+}$ when doped in $CaLiAl_3N_4$ (top panel) and $\beta$-SiAlON (bottom panel) host materials. Adapted from ref 201. Copyright 2016 American Chemical Society.

excited states and suppressed electron−phonon coupling, imposed by the rigid framework of the host lattice. It is noteworthy that the Debye temperature can be treated as a condition equivalent to the rigidity or strength of the crystal lattice, as discussed in section 5.1. As such, it is now common practice to predict the emission bandwidth using the Debye temperature. For example, doped systems with high Debye temperatures tend to produce narrow-band emissions.

Besides the rigidity factor, the number of nonequivalent emission centers also plays an important role in regulating emission bandwidth because a broad-band emission can also originate from the overlapping of multiple 5d-4f emissions. For multinary compounds such as $SrLiAl_3N_4$,[19] $Y_3Si_5N_9O$,[306] $Ca_4F_2Si_2O_7$,[82] and $Ba_3Si_6O_9N_4$[307] phosphors, not merely one nonequivalent cation site is available for lanthanide substitution. If these nonequivalent sites have a significantly different coordination environment, the lanthanide's d orbital would give rise to different values of centroid shift and crystal field splitting, leading to overlapped emissions. In the case of narrow-band emitting $SrLiAl_3N_4:Eu^{2+}$ phosphor, the two coordination polyhedrons of $Eu^{2+}$ have indeed proven to be nearly identical.[19] The calculated density of states also showed similar covalency features between those two nonequivalent Eu sites.[231] Furthermore, the observed narrow-band signature in $SrMg_3SiN_4:Eu^{2+}$ (fwhm of ∼43 nm) was also ascribed to the lone site occupied by the Eu emitter.[308,309] It is worth noting that the experimentally observed narrow-band emission is usually associated with a more symmetric coordination environment around the dopant, as seen in $SrLiAl_3N_4$,[19] $SrMg_3SiN_4$,[308] and $BaSi_2N_2O_2$[310] lattices with the cuboidal coordination. These symmetric coordination features can be identified by comparing the density of state of the non-equivalent nitrogen sites.[231,309,311] Conversely, nonequivalent substitution sites featuring an asymmetric coordination polyhedron are likely to generate broad-band emissions. The observation of two nonequivalent Y sites with different electronic structures in $Y_3Si_5N_9O$ phosphor is in accordance with the broadband emission recorded for the phosphors upon $Ce^{3+}$ doping.[306] To modulate the distribution of the emitters occupied at the nonequivalent sites, one useful strategy is to introduce codopants. For instance, the codoping of $Ca^{2+}$ ions into $Sr_2Si_5N_8:Eu^{2+}$ phosphors leads to broadband emission because of the balancing in the substitution of two different strontium sites by $Eu^{2+}$.[312] Another demonstration was shown in the case of $Ba_3Si_6O_{12}N_2:Eu^{2+}$ phosphors in which a narrow-band emission (fwhm: 68.1 nm) was achieved by codoping $Mg^{2+}$ ions at a concentration of 0.3%.[313]

Due to the shielding effect of 5d and 6s orbitals, the splitting of 4f orbital is generally assumed to be insensitive to the host environment, thereby hardly contributing to the variation in the 5d-4f emission profile. However, both experimental results[314] and HF-based quantum calculations[315] showed that the splitting of $Ce^{3+}$ 4f orbital in some garnet-based materials could reach an energy of ∼4000 $cm^{-1}$, a level that is comparable to the splitting induced by effective field or spin−orbital coupling. Hence, it is imperative to include the effect of the host on the splitting pattern of 4f orbital in situations where the emission bandwidth needs to be precisely controlled. In 2016, an interesting phenomenon was reported by Wang et al., who demonstrated that a large splitting ($\Delta E_s$ > 0.1 eV) between two highest $Eu^{2+}$ $4f^7$ bands can theoretically be realized by doping $Eu^{2+}$ into hosts of $CaLiAl_3N_4$, $SrLiAl_3N_4$, $SrMg_3SiN_4$, and $BaLiAl_3N_4$ (Figure 16a).[201] These phosphors were found to exhibit narrow-band emissions experimentally. By comparison, a series of well-known broad-band emitting phosphors were generally characterized by small splitting values ($\Delta E_s$ < 0.1 eV).[201] On the basis of charge density analysis, the researchers argued that the large splitting of the 4f orbital in narrow-band emitting samples arises from the strong interaction between the "lobe"-like alignment of 4f level and the nitride anions (Figure 16b). Given that the degree of spectral overlap between multiple emissions is sensitive to the splitting pattern, the parameter $\Delta E_s$ thus could serve as a suitable descriptor for predicting emission bandwidth.

**5.4.4. Thermal Quenching Behavior.** Another important property of lanthanide ions is the inverse relationship between temperature and the intensity of luminescence arising from 5d-4f optical transitions. This property can be harnessed for temperature sensing or probing thermal transport in the micro- and nanodomains.[316] Blasse, Happek, and their co-workers discovered in silicate, borates, and oxides that the quenching could take place even at a low temperature, leading to a


DOI: 10.1021/acs.chemrev.6b00691
Chem. Rev. XXXX, XXX, XXX−XXX

significant reduction in quantum efficiency.[317−319] However, there are some exceptions. Lin et al. reported remarkable thermal stability in the luminescence of $KBPO_4:Eu^{2+}$ (B = Sr, Ba) and $LiSrPO_4:Eu^{2+}$ phosphors up to 250 °C.[320]

The correlation between the intensity $I(T)$ of 5d-4f luminescence and temperature T is given

$$I(T) = \frac{I(0)}{1 + \frac{\Gamma_0}{\Gamma_v}\exp\left(\frac{-\Delta E}{k_B T}\right)} \tag{23}$$

where $\Gamma_v$ is the radiative decay rate corresponding to the 5d state of the lanthanide, $\Gamma_0$ is the attempt rate of the thermal quenching process, $k_B$ is Boltzmann's constant, and $\Delta E$ is the energy barrier for thermal quenching. By adopting empirical parameters in eq 23, one could derive the thermal quenching barrier through

$$\Delta E = \frac{T_{0.5}}{680}\ \text{eV} \tag{24}$$

where $T_{0.5}$ is the quenching temperature, at which the emission intensity drops to 50% of its original intensity. Obviously, this empirical model suggests that the energy barrier for thermal quenching is an important parameter in determining the thermal stability of phosphors.

Four types of mechanisms have been proposed to explain the thermal quenching behavior observed for different types of lanthanide-activated phosphors. As shown in Figure 17, type I is based on the 4f-5d crossing model involving using a configuration coordination diagram.[33,321,322] Type II mechanism suggests that excitation of holes from lanthanide ions to the valence band of the host could also result in the thermal quenching of luminescence.[323] In the type III mechanism, the process of thermal quenching is shown to be likely induced by the presence of luminescent emitters with mixed valence charges ($Eu^{2+}$-$Eu^{3+}$ or $Ce^{3+}$-$Ce^{4+}$ pairs), as experimentally observed in phosphate- or YAG-based phosphors, respectively.[320,324] Type IV mechanism, also known as the thermal ionization model proposed by Dorenbos, describes that the 5d electron can be thermally excited to the host conduction band if the energy gap ($E_{dc}$) between the 5d level and the CBM is small.[325−327] The existence of small $E_{dc}$ values in $Ce^{3+}$-activated $Y_3Al_5O_{12}$[222] and $Y_3Si_5N_9O$[306] compounds has been verified by thermoluminescence excitation spectroscopy. By approximating the energy barrier $\Delta E$ with the measured energy gap $E_{dc}$, the stability of phosphors in relation to thermal variation can be assessed.

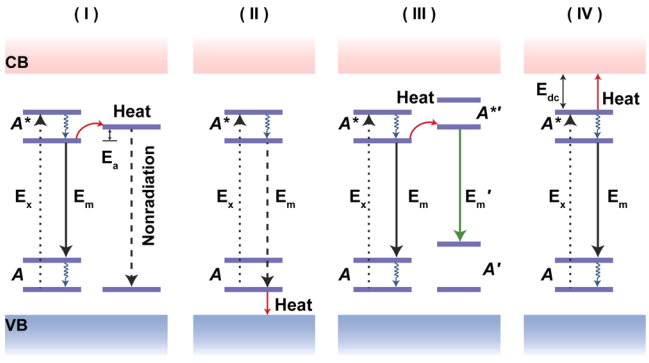


**Figure 17.** Schematic illustration of thermal effects on lanthanide luminescence by four different mechanisms. Type I: thermal quenching through nonradiative emission (4f-5d crossing model); type II: thermal quenching induced by the excitation of holes from the activator to the host valence bands; type III: thermal quenching through multiwavelength emission from activators with mixed valence charges; type IV: thermal quenching induced by the excitation of electrons to the host conduction band, a process also known as thermal ionization model. A and A* indicate the respective ground and excited states of the activator. A′ and A*′ represent the ground and excited states, respectively, of the activator with mixed valence charges. VB and CB stand for the valence and conduction bands of the host, respectively. $E_a$ is the activation energy needed to reach 5d-4f interconfigurational crossover. $E_{dc}$ is the energy barrier of the electrons ionized from the excited 5d substates to the conduction band. The dotted, solid, and dashed arrows represent photon excitation, emission, and nonradiation processes, respectively.

DFT-based simulations have been extensively utilized as a high throughput screening tool for thermal stable phosphors. Both the bandgap of the host and the relative location of 5d orbitals are relevant to the determination of $E_{dc}$. A host material with a large bandgap can provide sufficient space to accommodate 4f and 5d energy states and effectively decrease the probability of the overlapping between the lowest 5d state and the host CBM. For example, the difference in thermal quenching behavior between $Ba_3Si_6O_{12}N_2:Eu^{2+}$ (weak thermal quenching) and $Ba_3Si_6O_9N_4:Eu^{2+}$ (strong thermal quenching) phosphors could be explained using the thermal ionization model, whereby the large bandgap of $Ba_3Si_6O_{12}N_2$ may render a large value of $E_{dc}$.[230] The gap difference between these two compounds was further confirmed to be around 0.43 eV by more accurate quasiparticle calculations.[328] Similarly, in a recent study of thermal quenching behavior in $Y_3Si_5N_9O:Ce^{3+}$, Zhu et al. also attributed the small value of $E_{dc}$ (~0.023 eV) to the small bandgap of the host.[306] The same underlying mechanism has also been used to support the observation of different $E_{dc}$ values in two red-emitting phosphors, namely $SrLiAl_3N_4:Eu^{2+}$ and $SrMg_3SiN_4:Eu^{2+}$, with the former being about twice the value of the latter.[309]

The bandgap of a given phosphor and its associated $E_{dc}$ value are largely dependent on doping concentration. By taking $Eu^{2+}$-doped $CaAlSiN_3$ phosphors for instance, Chen et al. observed a decrease of 0.03 eV in bandgap with a doping concentration of 0.5% as shown in Figure 18a.[329] The researchers also found that the increase in $Eu^{2+}$ concentration leads to a large splitting of 5d orbitals, accompanied by a concurrent decrease in the value of $E_{dc}$. Surprisingly, they noticed that both the bandgap and the $E_{dc}$ of the phosphors under study vanish when the doping concentration of $Eu^{2+}$ reached 5%. Such phenomena indicate that the thermal ionization-based luminescence quenching is highly sensitive to the emitter's concentration. Unlike the well-defined 5d-CBM gap in $CaAlSiN_3:Eu^{2+}$ phosphors, the ground state-based quantum calculations suggest that the 5d orbitals are usually resonant with the conduction band or even located above the host CBM.

The constrained-DFT approach[183] can be used to study the electronic properties of doped systems at excited states through manipulation of the orbital occupation. For $Ba_3Si_6O_{12}N_2:Eu^{2+}$ and $Ba_3Si_6O_9N_4:Eu^{2+}$ oxynitrides, one can find that all $Eu^{2+}$ 5d levels are located well below the host CBM at the ground state, irrespective of the substitution site and the type of the host lattice.[307] However, only one substitution site in each host of chosen can produce the 5d-CBM gap at the excited state. Moreover, the $Ba_3Si_6O_{12}N_2:Eu^{2+}$ phosphor has a larger $E_{dc}$ value than its $Ba_3Si_6O_9N_4:Eu^{2+}$ counterpart, attributable to high luminescence thermal stability of the former (Figure 18, panels


DOI: 10.1021/acs.chemrev.6b00691
Chem. Rev. XXXX, XXX, XXX−XXX

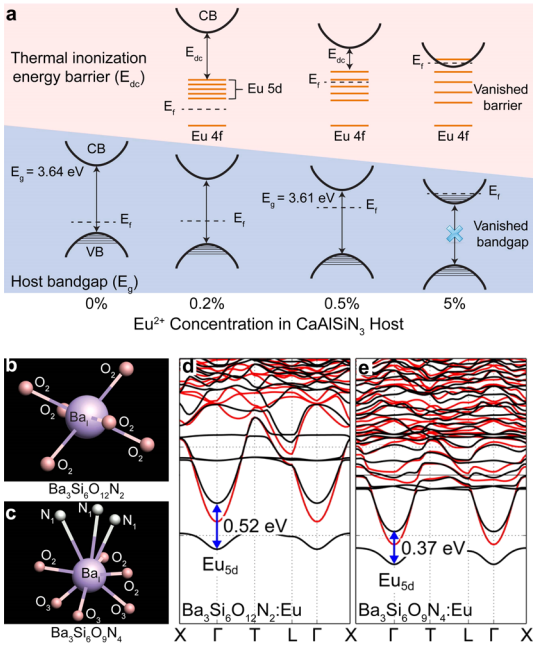


**Figure 18.** (a) Schematic illustration showing the correlation of 5d-CBM ($E_{dc}$) and bandgap ($E_g$) of $CaAlSiN_3$ material with $Eu^{2+}$ concentration. (b and c) Schematic representation of the coordination environment of the barium ion in $Ba_3Si_6O_{12}$ and $Ba_3Si_6O_9N_4$ lattices, respectively. Note that the 5d-CBM gap exists when the $Ba^{2+}$ ion in the host lattice is substituted by $Eu^{2+}$. (d and e) The corresponding spin-polarized (spin-up in black and spin-down in red) band structures of $Eu^{2+}$-doped $Ba_3Si_6O_{12}$ and $Ba_3Si_6O_9N_4$ phosphors, respectively. Adapted from ref 307. Copyright 2016 American Chemical Society.

b–e). Another case requiring the involvement of excited states pertains to $Ce^{3+}$-activated $LaSi_3N_5$ and $La_3Si_6N_{11}$ phosphors, in which the 5d-CBM gap vanishes at the ground state but exists at the excited state.[266]

As stated in section 5.4.1, Canning and co-workers have pointed out that the localization of the lowest d character at excited states can be used as a descriptor to differentiate the origin of the lowest unoccupied band.[277,284] Such a descriptor not only enables one to detect the event of 5d-4f emission but also potentially allows for the assessment of luminescence thermal stability. In principle, the predicted $E_{dc}$ value is likely to be small in those phosphors without a clear boundary between the host CBM and the lowest 5d level, leading to a low quenching temperature.

**5.4.5. Emission Decay Kinetics.** The rate of spontaneous emission, also defined as luminescence lifetime, is a kinetic characteristic of optical transitions. The 5d-4f emission within $Eu^{2+}$ and $Ce^{3+}$ ions is typically associated with a very fast dynamic process, featuring a decay time in the range of tens to hundreds of nanoseconds.[330,331] Such a fast decay rate makes the $Eu^{2+}$- or $Ce^{3+}$-doped phosphors promising for applications in lighting and scintillation. On the other hand, the decay time of the 5d-4f emission could be controlled over seconds to hours, as demonstrated in persistent phosphor $SrAl_2O_4$:$Eu^{2+}$,$Dy^{3+}$.[206] The phosphors featuring long lasting luminescence are also found attractive to various applications including display and imaging.

It is well-known that the variation in decay rate could benefit the study of energy transfer and reabsorption processes in a given phosphor containing sensitizer-activator pairs.[332] Thus, it is fundamentally crucial to understand the factors that dictate the decay rate. For any given optical species with similar decay rate, the decay curve can be obtained according to[333]

$$I(t) = C \times \Gamma_{rad} \exp[-(\Gamma_{rad} + \Gamma_{nr})t] \quad (25)$$

where $\Gamma_{rad}$ and $\Gamma_{nr}$ are the radiative and nonradiative decay rate, respectively, $t$ indicates time, and the constant $C$ is determined by the intrinsic properties of the instrument and the excited species. To obtain the luminescence lifetime, the diagram representing $I(t)$ versus $t$ is usually plotted. The slope of the plotted curve is considered as an experimentally determined decay rate. Note that the obtained decay rate is a summation of radiative and nonradiative decay rate.

It is believed that absolute measurement of luminescence quantum efficiency could be troublesome and laborious. As an additional benefit, luminescence lifetime can also serve as an alternative access to the estimation of the quantum efficiency. For a single-exponential decay curve, the decay time $t$ equals the reciprocal of the experimentally obtained decay rate

$$t = \frac{1}{\Gamma_{rad} + \Gamma_{nr}} \quad (26)$$

Considering that the nonradiative decay rate highly depends on the temperature while the radiative part is irrelevant to the temperature, one can estimate the quantum efficiency at high temperatures through

$$\Phi(T) = \frac{I(T)}{I_{lowT}} = \frac{t(T)}{t_{lowT}} \quad (27)$$

where $I_{lowT}$ and $t_{lowT}$ represent the luminescence intensity and the lifetime measured at low temperatures, respectively.

Apparently, an accurate mapping of decay rate could be very helpful for a better understanding of the underlying mechanisms that control luminescence processes of the phosphors. However, the measurement of luminescence lifetime is likely to be complicated by a multitude of factors. For example, different detectors are needed for measuring different ranges of decay times. Moreover, additional mathematical post-treatments may be necessary for accurate measurement of lifetimes for optical transitions between degenerate energy levels. More importantly, the experimental techniques for lifetime measurement are not able to differentiate the decay contribution between the radiative and nonradiative processes, thus incapable of resolving the issue pertaining to the dissipation of excitation energies. It is plausible that the existence of multiple decay rates in one optical system may pose a further constraint to the lifetime measurement.

DFT-based techniques are unable to predict dynamic optical properties at excited states. Despite the limitation, they can provide qualitative estimation of luminescence lifetime based on the ground-state electronic structures. For illustration, let us consider lanthanide-activated scintillators. In principle, there are three competing decay channels existing in a given lanthanide-activated scintillator, namely fast, intermediate, and slow decay channels (Figure 19).[20,334,335] Fast decay is often associated with direct 5d-4f emission of lanthanide emitter after sequential capture of holes and electrons during ionization. For intermediate decay, the lifetime is prolonged due to trapping of electrons at impurity levels, leading to delayed electron migration to lanthanide emitters. By comparison, slow decay generally features long lifetimes up to microseconds, arising from the formation of self-trapped excitons. Such excitons may


DOI: 10.1021/acs.chemrev.6b00691
Chem. Rev. XXXX, XXX, XXX–XXX

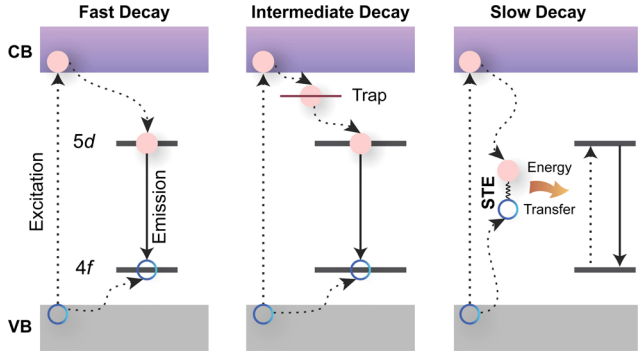


**Figure 19.** Schematic illustration of three scintillating processes characterized by different decay rates. VB and CB stand for the valence and conduction bands of the host, respectively. STE refers to self-trapped exciton. Pink dot and blue circle represent electron and hole carries, respectively. The dotted and solid straight arrows represent photon excitation and emission processes, respectively. Note that curved dotted arrows represent the transporting pathways of the carriers.

produce radiative emission to excite the emitters. These excitons can also migrate to the emitters, resulting in nonradiative energy transfer and direct emission of the emitters. Both emission processes are characterized by prolonged decay rates. Taken together, the decay rate of the scintillators is not only determined by the intrinsic lifetime of the excited 5d states but also affected by the diffusion rate of the holes, electrons, and exciton, as well as the lifetime of the excitons.

To address the issue of scintillation response, Du and Wei and their co-workers theoretically investigated carrier transport in a series of elpasolite-hosted scintillators, including $Cs_2LiYCl_6:Ce^{3+}$, $Cs_2AgYCl_6:Ce^{3+}$, and $Cs_2NaRBr_3I_3:Ce^{3+}$ (R = La, Y).[286,287,335] On the basis of the calculated electronic structures, the energetics of charge carriers, and the carrier-trapping ability of Ce activators, they found that combining more electronegative host cations with less electronegative host anions should result in more dispersive valence and conduction bands. An increased dispersity of the energy bands indicates reduced binding energies in the electrons, holes, and the excitons, which enables one to enhance the efficiency of transfer from self-trapped carriers to $Ce^{3+}$. As anticipated, fast decay rates are observed in those above-mentioned scintillators.

In another independent investigation related to self-activated scintillators, Shi and Du pointed out that the discrete electronic bands in $Cs_2NaInBr_6$, $Cs_2NaBiCl_6$, and $Tl_2NaBiCl_6$ crystals can stabilize self-trapped and dopant-bound excitons and also boost the radiative emission of excitons.[336] The discontinuity of the energy bands in these crystals was ascribed to two factors. One is driven by the large difference in electronegativity of host atoms. The second arises from the large distance between nearest-neighboring ions in the host lattice. As a result, fast decay rate could be achieved through manipulation of host atoms with small difference in electronegativity and short nearest-neighboring distance. The level of band dispersion and continuity can thus be recognized as a proper descriptor for the qualitative estimation of the scintillator's decay rate.

As described early, the shallow impurity levels in scintillators are able to trap free charge carriers, giving rise to prolonged luminescence lifetime. Similarly, frequency conversion phosphors, typically used as major components in white-LEDs, also display defect-induced slow decay rates.[337] These shallow traps within the band gap are usually caused by point defects and impurities, as evidenced in $Lu_3Al_5O_{12}:Ce^{3+}$ phosphors with antisite defects.[338,339] It should be noted that the formation energies of the antisite defects were determined to be considerably low according to the DFT calculations.[340−345] Lithium vacancies may appear when the replacement of $Ce^{3+}$ with $Ca^{2+}$ occurs in $LiCaAlF_6$ lattices.[346] Moreover, fluorine vacancies may exist in the $LiCaAlF_6$ crystal upon X-ray or gamma-ray irradiation.[347,348] Both types of vacancies can lead to reduced decay rates due to shallow trapping of charge carriers. Even high performance $LaBr_3:Ce^{3+},Sr^{2+}$ scintillators suffer from decreased decay rates, which can be attributed to the generation of neutral $V_{Br}$-$Sr_{La}$ complexes.[288]

To enhance the decay rate of phosphors, the most straightforward strategy is to effectively remove those shallow traps. Co-doping of extrinsically added ions has been well-adopted in an effort to mitigate the formation of shallow traps.[347,349,350] As a powerful tool, DFT can be used for the identification and characterization of defects.[351−354] For example, Du and Singh analyzed the electronic structure of $LiCaAlF_6$ host material comprising charge carrier traps by means of DFT calculations.[355] The authors found that a fluorine vacancy induces one localized defect level within the bandgap, capable of trapping one or two electrons.

In 2011, Stanek and co-workers pointed out that the delayed luminescence of $Lu_3Al_5O_{12}:Ce^{3+}$ phosphors originates from the cation antisite-caused electron trapping.[356] By assessing the electronic structure of the doped system, they found that additional doping of $Ga^{3+}$ can independently shift the valence and conduction bands toward each other. The shifting at work can lead to a swallow of the antisite-induced trap by the conduction band, thereby disabling the trapping capacity of the defects. In a following paper, they confirmed theoretically the mechanism of $Ga^{3+}$-enhanced decay rate, which is reliant on the change in the electronic structure rather than reduced concentration of the antisite defects.[357] Importantly, the same group of researchers systematically performed DFT calculations on band structures of multicomponent garnets, including $Lu_3B_5O_{12}$ (B = Al, Ga, In, As, and Sb) and $R_3Al_5O_{12}$ (R = Lu, Gd, Dy, and Er).[358] Their theoretical results suggest that varying R ions merely affects the band structure of the host crystal, while type B ions play a predominant role in the determination of the band structure. Specifically, incorporation of $Ga^{3+}$ and $In^{3+}$ dopants decreases the bandgap by lowering the conduction band minimum, while doping of $As^{3+}$ and $Sb^{3+}$ leads to a reduction in bandgap by raising the valence band maximum. It should be noted that carrier trapping can also play a positive role in enhancing the decay rate of the phosphors. As illustrated in the case of $Lu_3Al_5O_{12}:Ce^{3+},Mg^{2+}$ phosphors, a localized hole trap originating from an $O^-$ center is responsible for stabilizing a $Ce^{4+}$ transient state, providing a new channel for direct electron−hole recombination.[359]

Also of note is the recent efforts in developing phosphors exhibiting long lasting luminescence. The presence of charge carrier traps in these phosphors endows them with persistent luminescence by gradually releasing charge carriers from the impurity levels under external stimulation.[360] In general, the persistent luminescence could last several hours to even a few days, dependent on the depth of the trap levels within the band gap. An effective strategy for controlling the trap depth is through codoping of a particular ion.[361−364] Thus, the relative position of the trap level to the host's band can also be considered as a proxy for estimating the decay rate of phosphors under study.


DOI: 10.1021/acs.chemrev.6b00691
Chem. Rev. XXXX, XXX, XXX−XXX

Recently, Rega and co-workers directly calculated the fluorescence lifetime and quantum yield of rhodamine derivatives using a time-dependent DFT method.[365] They predicted the spontaneous radiative decay rate $k_r$ for $S_1 \rightarrow S_0$ transition according to

$$k_r = \frac{3}{4}\frac{\Delta E^3}{c^3}\mu_{10}^2 \tag{28}$$

where $\Delta E$, c, and $\mu_{10}^2$ are the transition energy, the speed of light, and the transition dipole strength, respectively. By combing the calculated radiative decay rate with the experimentally determined decay rate, the researchers estimated the quantum yield by calculating the radiative fraction of the total decay rate from

$$\Phi = \frac{k_r}{k_r + k_{nr}} = \frac{\tau_{exp}}{\tau_r} \tag{29}$$

where $k_r$ and $k_{nr}$ are the radiative and nonradiative decay rate, respectively. $\tau_r$ refers to the calculated decay time, and $\tau_{exp}$ is the decay time experimentally determined. On the basis of the theoretical and experimental results, the authors suggested that the radiative decay rate is highly dependent on the specific structure of rhodamine moieties. Considering that the HF-method is able to calculate the energy and dipole strength of 4f-5d transitions, it is plausible to extend the model to an inorganic phosphor for quantitatively investigating the correlation between the decay rate and materials composition.

## 6. APPLICATIONS

As already mentioned in the introduction part, lanthanide-activated phosphors based on 4f-5d transitions have been widely used as luminescent materials for optoelectronic and imaging applications. In this section, we will briefly summarize recent advances in applications of these phosphors, notably as lighting and scintillating materials. We will also highlight a number of long persistent phosphors and put them into the context of emerging applications such as temperature and pressure sensing, combined imaging and theranostics, photocatalysis, and photovoltaics.

### 6.1. Solid State Lighting

White light emitting diodes comprising inorganic phosphors have been touted as the third generation of solid state lighting devices (Figure 20). When compared to traditional incandescent and fluorescent lamps, the LED-based technology offers a number of advantages, including high efficiency, low consumption of energy, long operating lifetime, fast switching, and low production cost. Notably, the phosphor is an indispensable component of the white light emitting devices commercially

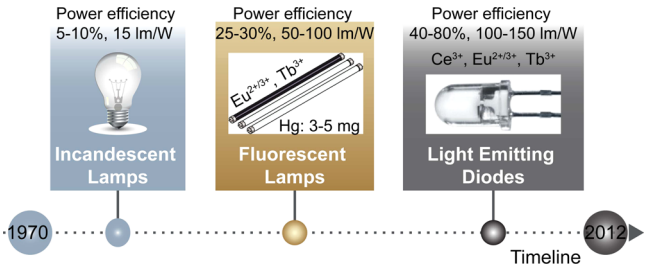


**Figure 20.** Historical development of white-light emitting devices since 1970.

available. By leveraging the electrical dipole allowed 4f-5d optical transition, the associated optical features, such as high absorption rate and fast emission time, have enabled the development of $Ce^{3+}$- and $Eu^{2+}$-based phosphors for application as active components in white light emitting devices.[246,366,367]

In 1995, $Ce^{3+}$-doped YAG phosphors were first developed to generate white light emission by combing a LED-enabled blue light with broad yellow emission from the $Ce^{3+}$-activated YAG phospohrs.[368] Such phosphors feature broadband emissions in the visible spectral region (500−700 nm), efficient absorptions for blue light (420−480 nm), high quantum efficiencies (>90%), and high thermal quenching temperatures (~700 K), as well as fast decay rates (~63 ns).[188,337,369,370] However, the lack of red-emitting component of YAG phosphors in the visible leads to a poor color rendering index (CRI = 70−80) and a high correlated color temperature (CCT = 7750 K), making them unsuitable for illumination-grade lighting. By codoping of $Mg^{2+}$ and $Si^{4+}$ ions, the emission maximum of YAG:$Ce^{3+}$ phosphors can be shifted to around 600 nm, allowing a warm white emission with higher CRI values to be realized.[371,372] In addition, red-emitting components with peaks located in the range from 590 to 660 nm were observed in nitride-based phosphors, such as $(Ba,Sr)_2Si_5N_8:Eu^{2+}$ and $(Ca,Sr)SiAlN_3:Eu^{2+}$, which also find applications for illumination-grade white light emitting diodes.[203,373−375]

For those red-emitting phosphors featuring broadband emission, a considerable portion of light is typically emitted beyond 650 nm, which is insensitive to the naked eye. Apparently, the broadband emission significantly limits the overall efficiency of the illuminating device. In 2010, Xia et al. investigated a series of sulfide-based red-emitting phosphors such as $SrS:Eu^{2+}$, $CaS:Eu^{2+}$, and $Ca_{1-x}Sr_xS:Eu^{2+}$ with narrow-band emission (fwhm: ~ 70 nm).[376] Unfortunately, these phosphors exhibit a strong concentration and thermal quenching behavior, have limited stability against moisture, and require a toxic gas during the synthesis.

Very recently, Schnick and co-workers discovered a new type of red-emitting phosphor in the form of $Sr[LiAl_3N_4]:Eu^{2+}$, which has an emission peak centered at 650 nm with a fwhm of 50 nm.[19] The quantum efficiency of phosphor can be retained above 95% even under heating at a temperature of 200 °C. Compared to commercially available white LEDs without the phosphors, the phosphor-embedded equivalents show an increased luminous efficacy by 14%, combined with an excellent CRI. Nonetheless, it is important to stress that red-emitting phosphors eligible for high luminous white LEDs are still very rare due to the strong demand on the brightness of these phosphors. This is because the eye has a varying sensitivity over the visual spectrum, being relatively insensitive to red light emitted under low light conditions.

UV-emitting LEDs can also be used to generate white light by exciting a mixture of blue, green-yellow, and orange-red emitting phosphors.[377−381] Apart from the multicomponent approach, the method involving single-component white-emitting phosphors has recently attracted much attention as they enable one to achieve high luminous efficiencies and excellent color rendering indices.[44,382−385] When selecting different excitation sources, one must take into account the difference in performance criteria required for the phosphors under investigation.

It is worth noting that a lanthanide-doped phosphor not only can participate as an active component in illumination-grade lighting but also can serve as a spectral converter attractive for


DOI: 10.1021/acs.chemrev.6b00691
Chem. Rev. XXXX, XXX, XXX−XXX

use in horticulture and photovoltaics. For example, high-efficiency $(Ba,Sr)_3MgSi_2O_8:Eu^{2+},Mn^{2+}$ phosphors have been synthesized and used for promoting photosynthesis in living organisms.[386−389] These phosphors feature a dual-peak emission centered at 660 and 430 nm, both of which are suitable for triggering photosynthetic reactions. Note that these phosphors, prepared either in particle, thin film, or bulk forms, could be excited by sunlight or many types of LEDs.

Given the ability to absorb light exposure in a broad wavelength range, $Ce^{3+}$, $Eu^{2+}$, and $Yb^{2+}$ ions are usually used as sensitizers in photoconverting systems to offset the mismatch between the solar emission and the absorption window of Si solar cells.[390] Typical sensitizer−activator pairs are $Ce^{3+}$−$Yb^{3+}$, $Eu^{2+}$−$Yb^{3+}$, $Yb^{2+}$−$Yb^{3+}$, and $Ce^{3+}$−$Pr^{3+}$, and $Eu^{2+}$−$Pr^{3+}$.[391−396] Despite the enticing prospects of the approach, we have faced the problem of limited external quantum efficiency associated with the phosphor convertors in practical applications. Scientists have been working hard to come up with a solution, and one of the results is the coupling of plasmonic resonance.[397]

### 6.2. Scintillation

Scintillation is a special type of photoluminescence for which minute flashes of light are generated by certain materials when exposed to ionizing radiation. These materials are known as scintillators and able to convert high-energy X-rays or gamma-rays (typically from KeV to GeV) into photons in the UV−visible range. A scintillator detector usually consists of an electronic light sensor that converts the light emitted by the scintillator into an electrical pulse via the photoelectric effect. The quality of the scintillator material is important as it affects both the efficiency and the resolution of the detector. Research on scintillators could be traced back to 1895 when Wilhelm Roentgen discovered the possibility of using electromagnetic radiation to create X-rays.[398] It was subsequently recognized that $CaWO_4$- and ZnS-based powders could be introduced as scintillators for X-ray detection.[399] In the late 1940's, NaI:Tl and CsI:Tl in the form of single crystals were first put in place as scintillators, followed by the advent of oxide-based $CdWO_4$ and $Bi_4Ge_3O_{12}$ scintillators for versatile applications in the field of high-energy physics.[400−403]

As summarized in Figure 21, lanthanide-doped inorganic crystals have become prevalent for use in scintillation purposes since the 1980's. Current investigations are focused on $Ce^{3+}$, $Pr^{3+}$, $Nd^{3+}$, and $Eu^{2+}$ with dipole allowed 5d-4f optical transitions, which enable a fast decay rate in favor of the scintillation process.[404−407] There are several key criteria for evaluating the scintillator's performance such as luminescence efficiency, light yield, energy resolution, response time, and chemical stability.[18] The selection criteria for scintillators vary slightly depending on different applications. For advanced imaging and thermoluminescence dosimetry, for example, $Ce^{3+}$- and $Pr^{3+}$-activated scintillators with fast decay time (10−60 ns) and high quantum yield are often chosen because their fast response and high light yield dominate the overall performance of the systems.[408−410] For positron emission tomography, $Lu_2SiO_5:Ce^{3+}$ scintillators are selected due to their relatively high light yield (~30000 ph/MeV), fast decay time (40 ns), large effective atomic number (66), and high materials density (7.4 g/cm$^3$).[411−414] To suit the need of time-of-flight positron emission tomography, one may consider $LaBr_3:Ce^{3+}$ scintillators as they show a ultrashort decay time (16 ns), an excellent energy resolution (3% at 662 keV) and a high light yield (61000 ph/MeV).[415] However, $LaBr_3:Ce^{3+}$ scintillators are not quite suitable for advanced application in radio astronomy detection because the radioactivity of one lanthanum isotope ($^{138}La$) can interfere with the detection process.[416] A better candidate would be $CeBr_3$ crystals having intrinsic radioactivity 1 order of magnitude lower than its $LaBr_3$ counterpart.[417]

Although the decay rate of $Eu^{2+}$ is 1 order of magnitude slower than that of $Ce^{3+}$ emitter, the high light yield and energy resolution characteristics of the former stimulate the application of $Eu^{2+}$-based scintillators for security checking with a tolerance of scintillation response time up to few microseconds.[418,419] At present, the most studied $Eu^{2+}$-related scintillating materials are $SrI_2:Eu^{2+}$ crystals, which have very high light yields in the range of 80000−120000 ph/MeV and energy resolutions between 2.6−3.7% under 662 keV. The main drawbacks of these materials are the risk of high reabsorption and low resistance against moisture.[420] The subsequently developed $Eu^{2+}$-doped ternary crystals such as $CsBa_2I_5$ and $Cs(SrBa)I_3$ show better resistance to moisture, while keeping a very good energy resolution of 3.9% and a high light yield around 80000 ph/MeV.[421]

By codoping $Ga^{3+}$ ions into $Lu_3Al_5O_{12}:Pr^{3+}$ scintillators, the scintillation response can be substantially accelerated.[422] The codoping strategy through the use of $Gd^{3+}$ and $Ga^{3+}$ ions to modify $Lu_3Al_5O_{12}:Ce^{3+}$ and $Y_3Al_5O_{12}:Ce^{3+}$ scintillators can lead to increased light yield up to 40000 and 44000 ph/MeV, respectively.[423,424] Moreover, divalent cations such as $Ca^{2+}$ and $Mg^{2+}$, once infused in $Lu_2SiO_5:Ce^{3+}$, $Gd_3Ga_3Al_2O_{12}:Ce^{3+}$ and $Lu_3Al_3O_{12}:Ce^{3+}$ lattices, are found to be effective in eliminating the afterglow of the scintillators. This improvement can dramatically enhance the strength of the signals in biomedical imaging.[425−429] For research work concerning how to optimize the characteristics of scintillators through composition manipulation, the reader is referred to the literature for details of the optimization.[18,406,410,430]

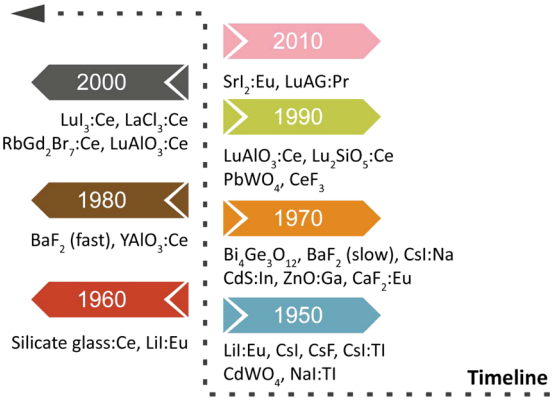


**Figure 21.** Historical development of scintillating materials since 1950.

### 6.3. Persistent Luminescence

Upon stimulation either thermally, optically, or mechanically, persistent phosphors are able to glow light in the dark lasting from minutes to days. The phenomenon of persistent luminescence discovered from ancient luminous pearls, also known as luminous jades, is fascinating as they show afterglow activity long after the excitation has ended. The mechanism underlying this phenomenon is not fully understood. It was not until the beginning of the 17th century that the researchers realized barium sulfide containing impurities as the origin of


DOI: 10.1021/acs.chemrev.6b00691
Chem. Rev. XXXX, XXX, XXX−XXX

persistent luminescence in luminous jades. In the mid-1990's, the use of lanthanide-activated persistent phosphors began to dominate the consumer market, including display, safety signage, and decoration. These materials are much safer than ZnS-based products. The lanthanide-doped phosphors also exhibit high luminescence intensity and long-lasting activity, as exemplified by Matsuzawa et al. in the cases of blue-emitting $CaAl_2O_4:Eu^{2+},Nd^{3+}$ and green-emitting $SrAl_2O_4:Eu^{2+},Dy^{3+}$ phosphors.[56] Findings from this study suggest that the prolonged emission lifetime is likely to be governed by the slow liberation of trapped charged carriers.

Depending on the mode of charge trapping and release, the prospect of long persistent phosphors can be harnessed for temperature or stress sensing, biological imaging, and detection of high-energy rays. For instance, Ricci and co-workers found that synthetic $(Lu,Y)_2SiO_5:Ce^{3+}$ phosphors display optically stimulated luminescence with signal strength comparable to the commercial ones.[431] In 2015, Chiriu et al. systematically investigated $(Lu,Y)AlO_3:Ce^{3+}$ phosphors comprising multilevel traps for charge carriers. They demonstrated the feasibility of controlling and engineering such carrier traps in rare-earth aluminum perovskites for optical memory storage.[432] On a separate note, Liu et al. reported that codoping significantly enhances the photosensitivity of $Sr_3SiO_5:Eu^{2+},Tm^{3+}$ phosphors to near-infrared light through various mechanisms.[433] A low threshold power density ($\sim$54 $\mu W/cm^2$) was required for the generation of persistent luminescence. Remarkably, the light storage time was extended beyond 10 days. By harnessing the effect of mechanoluminescence in $SrAl_2O_4:Eu^{2+}$-based phosphors, prototype devices could be fabricated to monitor the stress distribution of buildings and large structures, potentially providing early warning of impending earthquakes.[434,435]

More recently, lanthanide-activated persistent phosphors with near-infrared emission have been implemented for in vivo imaging applications.[436−442] For example, using a small amount of silica-modified $SrMgSi_2O_6:Eu^{2+},Dy^{3+}$ phosphors, Li et al. discovered that the afterglow signal could be detected in a living mouse even 1 h after peritoneal injection of the phosphors.[443] In a parallel study, Yan et al. demonstrated that by conjugating with $\alpha$-fetoprotein-antibody-decorated gold nanoparticles, hardystonite-based phosphors with a formula of $(Ca,Mg)_2ZnSi_2O_7:Eu^{2+},Dy^{3+}$ can be engineered as a highly selective photoluminescent probe toward $\alpha$-fetoprotein.[444] By its very long-lasting nature, it means that this afterglow probe enables imaging without external illumination and thus provides significantly enhanced signal-to-noise ratio for biological detection.

Persistent luminescence plays a role that may turn out to be vital to the developing field of photocatalysis and photovoltaics. The expanding interest in these domains is largely stimulated by economical and ecological advantages of using solar light as an abundant source of energy.[445−448] The Wang group synthesized $CaAl_2O_4:Eu^{2+},Nd^{3+}@TiO_2$ composite phosphors by a sol−gel method and validated their suitability for the degradation of nitrogen monoxide gas.[447] This studies also support the idea that the phosphors can amass a considerable amount of the UV or visible light to be used for triggering photocatalytic reactions in the dark. Though the underpinning of photovoltaics through the use of persistent phosphors was not fully examined, $SrAl_2O_4:Eu^{2+},Dy^{3+}$ phosphors have been reported for effective energy harvesting to drive silicon solar cells in the dark, with a maximal increase of 4.6% in conversion efficiency under one sun illumination relative to the one with pure glass.[448]

## 7. BROADER IMPLICATIONS AND OUTLOOK

Lanthanide-activated phosphors have a range of optical properties that scientists are investigating, driven by both curiosity and new opportunities for developing a multitude of technologies across a wide spectral range. Theoretical modeling of these materials is crucial, as it leads to improved mechanistic understanding and provides experimentalists with a blueprint to design and make new optical systems and devices that have characteristics easily tailorable for specialized applications. In this review, we summarize some of the latest synthetic developments, particularly for phosphors featuring 4f-5d optical transitions, and the emerging computational approaches that combine phenomenological theories with quantum mechanical calculations for accurate prediction of luminescence properties. Although a particular emphasis is placed on $Ce^{3+}$- and $Eu^{2+}$-activated phosphors, we believe that these theoretical approaches should be readily expandable to other lanthanide-doped systems with the characteristics of 4f-5d optical transitions. We also examine a specific set of parameters employed to design customized high performance phosphors and how they result in considerable difference in the optical properties. These include Debye temperature, dielectric constant, coordination environment around the luminescent center, and accurate energies of 4f and 5d levels, as well as the parameter associated with the relative position of 4f and 5d levels to the host's valence and conduction bands.

In addition to the general guidelines described above, there may be specific requirements that need to be satisfied. For example, in the context of a fast scintillation process, the cross-luminescence induced by radiative electronic transitions from the mainly anion-related valence band to the outermost cation core band must be taken into account.[449] This cross-luminescence phenomenon along with the general criteria for rational design of luminescent materials can be predicted surprisingly well using HF- and DFT-based quantum calculations. Impressive progress has been made using HF as a basis when calculating the excited state energy of phosphors and constructing their absorption and emission spectra. Unfortunately, the HF method is unsuitable to handle systems with dopant-induced lattice distortion. It also has trouble describing the position of the energy levels of the dopant ions relative to the valence and conduction bands of the host material. The main advantage of DFT-based methods is that they are applicable to calculations of ground state characteristics of perfect or even defective solids comprising many interacting atoms. Consequently, DFT can establish an exact energy-band landscape of doped systems. Despite its ubiquity, DFT has some serious shortcomings as we progress toward realistic luminescent systems. This is particularly the case for the calculation of doped systems that involve electron−hole interactions. DFT simulations are thus unable to be used to study the optical properties of solids at the excited states. As this review helps illustrate, an effective solution is to combine the strengths of both HF and DFT methods, providing chemists with a platform that enables optical transition approximation while simultaneously allowing atomic structures to be predicted with high accuracy.

Recently, tremendous interest has been devoted to the development of novel optical nanomaterials through lanthanide doping because of its exquisite control over the characteristics


DOI: 10.1021/acs.chemrev.6b00691
Chem. Rev. XXXX, XXX, XXX−XXX

of optical emissions at single particle levels.[450,451] It should be noted that the parameters implemented for phosphor design under current study are all tested on bulk structures. For that reason, it remains questionable whether the general criteria considered thus far hold true at the nanoscale. For nanophosphors comprising large surface areas or high densities of interfacial boundaries, the coordination polyhedron of a doped emitter is usually more distorted than that present in the bulk lattice.[452,453] The surface ligands typically introduced during the crystal growth process can add more complexity to the situation.[451,454−458] Nonetheless, the subtle details on luminescence properties of nanophosphors and the corresponding bulk materials could be elucidated by taking advantages of HF- and DFT-based modeling. The combined computational approach also provides a powerful tool that may allow additional parameters acting on the surface effect to be extracted. Beyond facilitating high-throughput materials design, the applications exemplified and the strategies outlined in this review are expected to stimulate the search for a whole new set of phosphors for fundamental studies and potential applications in a wide range of fields.

## AUTHOR INFORMATION

### Corresponding Authors

*E-mail: chmqinx@nus.edu.sg.
*E-mail: iamwhuang@njtech.edu.cn.
*E-mail: marco.bettinelli@univr.it.
*E-mail: chmlx@nus.edu.sg.

### ORCID

Wei Huang: 0000-0001-7004-6408
Xiaogang Liu: 0000-0003-2517-5790

### Notes

The authors declare no competing financial interest.

### Biographies

Xian Qin earned her B.S. degree (2007) in Mechanical Engineering from Sichuan University. She received her Ph.D. degree under the supervision of Prof. Qingyuan Meng in 2013 from Harbin Institute of Technology, P. R. China. She subsequently carried out postdoctoral training in Chemistry Department at National University of Singapore and also Institute of Materials Research and Engineering (IMRE) at A*STAR, Singapore. Her current research is focused on molecular optoelectronics, low-dimensional systems design and Brownian motion, as well as quantum and classical methodologies for understanding optical properties of luminescent nanomaterials.

Xiaowang Liu earned his B.S. (2004) and M.S. (2007) degrees in Physical Chemistry from Anhui Normal University, under the supervision of Prof. Baoyou Geng. After working on the teaching staff at Anhui Normal University for four years, he joined the group of Prof. Xiaogang Liu and received his Ph.D. degree in 2016 at National University of Singapore, where his research has focused on the design, synthesis, and assembly of inorganic nanocrystals. He is currently Associate Professor of Chemistry at Anhui Normal University.

Wei Huang received his B.S., M.S., and Ph.D. degrees in Chemistry from Peking University, P. R. China, in 1983, 1988, and 1992, respectively. In 1993, he began his postdoctoral training at National University of Singapore, where he participated in the founding of the Institute of Materials Research and Engineering, Singapore. In 2001, he became a chair professor at Fudan University, where he founded and chaired the Institute of Advanced Materials. In June 2006, he was appointed as the Deputy President of Nanjing University of Posts and Telecommunications, where he initiated the Institute of Advanced Materials and the Key Laboratory for Organic Electronics and Information Displays. In July 2012, he was appointed as the President of Nanjing University of Technology. He is an academician of the Chinese Academy of Sciences and the editor-in-chief of npj Flexible Electronics. His research interests include organic optoelectronics, nanomaterials, polymer chemistry, plastic electronics, and bioelectronics.

Marco Bettinelli received his doctoral degree in Chemistry (1981) at the University of Parma, Italy. He was an Assistant Professor at the University of Padova (1983−1992) and an Associate Professor at the University of Salerno (1992−1993). In October 1993, he moved to the University of Verona, where he is a Full Professor of Inorganic Chemistry (since 2002) in the Luminescent Materials Laboratory, Department of Biotechnology. Currently, he serves as the editor-in-chief for Journal of Luminescence. His scientific interests deal with numerous aspects of luminescent materials, and in particular, with the synthesis, characterization, and spectroscopic properties of crystalline, nanocrystalline, and amorphous systems containing lanthanide and transition metal ions.

Xiaogang Liu earned his B.E. degree (1996) in Chemical Engineering from Beijing Technology and Business University, P. R. China. He received his M.S. degree (1999) in Chemistry from East Carolina University under the direction of Prof. John Sibert and completed his Ph.D. (2004) at Northwestern University under the supervision of Prof. Chad Mirkin. He then became a postdoctoral fellow in the group of Prof. Francesco Stellacci at MIT. He joined the faculty of the National University of Singapore in 2006. He holds a joint appointment with the Institute of Materials Research and Engineering, Agency for Science, Technology and Research. Currently, he sits as an Associate Editor for Nanoscale and serves on the editorial boards of Chemistry−An Asian Journal, Advanced Optical Materials, and Journal of Luminescence. His research encompasses optical nanomaterials and energy transfer and explores the use of luminescent nanocrystals for photocatalysis, sensing, and biomedical applications.

## ACKNOWLEDGMENTS

This work is supported by the Singapore Ministry of Education (Grants R143000627112 and R143000642112), Agency for Science, Technology and Research (A*STAR) under the contracts of 122-PSE-0014 and 1231AFG028 (Singapore), National Research Foundation, Prime Minister's Office, Singapore under its Competitive Research Program (CRP Award no. NRF-CRP15-2015-03), National Basic Research Program of China (973 Program, Grant 2015CB932200), National Natural Science Foundation of China (Grant 21471109), Nano Projects of Soochow City (Grant ZXG201412), and the CAS/SAFEA International Partnership Program for Creative Research Teams.

## REFERENCES

(1) Eliseeva, S. V.; Bünzli, J.-C. G. Rare Earths: Jewels for Functional Materials of the Future. *New J. Chem.* **2011**, *35*, 1165−1176.
(2) Bünzli, J.-C. G.; Piguet, C. Taking Advantage of Luminescent Lanthanide Ions. *Chem. Soc. Rev.* **2005**, *34*, 1048−1077.
(3) Li, G.; Tian, Y.; Zhao, Y.; Lin, J. Recent Progress in Luminescence Tuning of $Ce^{3+}$ and $Eu^{2+}$-Activated Phosphors for pc-WLEDs. *Chem. Soc. Rev.* **2015**, *44*, 8688−8713.
(4) Zhou, B.; Shi, B.; Jin, D.; Liu, X. Controlling Upconversion Nanocrystals for Emerging Applications. *Nat. Nanotechnol.* **2015**, *10*, 924−936.
(5) Auzel, F. Upconversion and Anti-Stokes Processes with f and d Ions in Solids. *Chem. Rev.* **2004**, *104*, 139−174.


DOI: 10.1021/acs.chemrev.6b00691
*Chem. Rev.* XXXX, XXX, XXX−XXX

(6) Liu, G. Advances in the Theoretical Understanding of Photon Upconversion in Rare-Earth Activated Nanophosphors. *Chem. Soc. Rev.* **2015**, *44*, 1635−1652.
(7) Liu, Y.; Tu, D.; Zhu, H.; Chen, X. Lanthanide-Doped Luminescent Nanoprobes: Controlled Synthesis, Optical Spectroscopy, and Bioapplications. *Chem. Soc. Rev.* **2013**, *42*, 6924−6958.
(8) Dong, H.; Du, S.-R.; Zheng, X.-Y.; Lyu, G.-M.; Sun, L.-D.; Li, L.-D.; Zhang, P.-Z.; Zhang, C.; Yan, C.-H. Lanthanide Nanoparticles: From Design toward Bioimaging and Therapy. *Chem. Rev.* **2015**, *115*, 10725−10815.
(9) van der Ende, B. M.; Aarts, L.; Meijerink, A. Near-Infrared Quantum Cutting for Photovoltaics. *Adv. Mater.* **2009**, *21*, 3073−3077.
(10) Hehlen, M. P.; Brik, M. G.; Krämer, K. W. 50th Anniversary of the Judd−Ofelt Theory: An Experimentalist's View of the Formalism and Its Application. *J. Lumin.* **2013**, *136*, 221−239.
(11) van Pieterson, L.; Reid, M. F.; Wegh, R. T.; Meijerink, A. $4f^n \leftrightarrow 4f^{n-1}5d$ Transitions of the Trivalent Lanthanides: Experiment and Theory. *J. Lumin.* **2001**, *94*−*95*, 79−83.
(12) Blasse, G.; Bril, A. Investigation of Some $Ce^{3+}$-Activated Phosphors. *J. Chem. Phys.* **1967**, *47*, 5139−5145.
(13) Jüstel, T.; Nikol, H.; Ronda, C. New Developments in the Field of Luminescent Materials for Lighting and Displays. *Angew. Chem., Int. Ed.* **1998**, *37*, 3084−3103.
(14) van Loef, E. V. D.; Dorenbos, P.; van Eijk, C. W. E.; Krämer, K.; Güdel, H. U. High-Energy-Resolution Scintillator: $Ce^{3+}$ activated $LaBr_3$. *Appl. Phys. Lett.* **2001**, *79*, 1573−1575.
(15) Shah, K. S.; Glodo, J.; Klugerman, M.; Higgins, W.; Gupta, T.; Wong, P.; Moses, W. W.; Derenzo, S. E.; Weber, M. J.; Dorenbos, P. $LuI_3$:Ce-A New Scintillator for Gamma Ray Spectroscopy. *IEEE Trans. Nucl. Sci.* **2004**, *51*, 2302−2305.
(16) Glodo, J.; van Loef, E. V. D.; Higgins, W. M.; Shah, K. S. Mixed Lutetium Iodide Compounds. *IEEE Trans. Nucl. Sci.* **2008**, *55*, 1496−1500.
(17) Dorenbos, P. Energy of the First $4f^7 \rightarrow 4f^6 5d$ Transition of $Eu^{2+}$ in Inorganic Compounds. *J. Lumin.* **2003**, *104*, 239−260.
(18) Nikl, M.; Yoshikawa, A. Recent R&D Trends in Inorganic Single-Crystal Scintillator Materials for Radiation Detection. *Adv. Opt. Mater.* **2015**, *3*, 463−481.
(19) Pust, P.; Weiler, V.; Hecht, C.; Tücks, A.; Wochnik, A. S.; Henß, A.-K.; Wiechert, D.; Scheu, C.; Schmidt, P. J.; Schnick, W. Narrow-Band Red-Emitting $Sr[LiAl_3N_4]:Eu^{2+}$ as A Next-Generation LED-Phosphor Material. *Nat. Mater.* **2014**, *13*, 891−896.
(20) Dorenbos, P. Scintillation Mechanisms in $Ce^{3+}$ Doped Halide Scintillators. *Phys. Status Solidi A* **2005**, *202*, 195−200.
(21) van der Kolk, E.; de Haas, J. T. M.; Bos, A. J. J.; van Eijk, C. W. E.; Dorenbos, P. Luminescence Quenching by Photoionization and Electron Transport in A $LaAlO_3:Ce^{3+}$ Crystal. *J. Appl. Phys.* **2007**, *101*, 083703.
(22) Dorenbos, P. 5d-Level Energies of $Ce^{3+}$ and the Crystalline Environment. I. Fluoride Compounds. *Phys. Rev. B: Condens. Matter Mater. Phys.* **2000**, *62*, 15640−15649.
(23) Dorenbos, P. 5d-Level Energies of $Ce^{3+}$ and the Crystalline Environment. II. Chloride, Bromide, and Iodide Compounds. *Phys. Rev. B: Condens. Matter Mater. Phys.* **2000**, *62*, 15650−15659.
(24) Dorenbos, P. 5d-Level Energies of $Ce^{3+}$ and the Crystalline Environment. III. Oxides Containing Ionic Complexes. *Phys. Rev. B: Condens. Matter Mater. Phys.* **2001**, *64*, 125117−125129.
(25) Barandiarán, Z.; Seijo, L. 4f, 5d, 6s, and Impurity-Trapped Exciton States of Lanthanides in Solids. *In Computational Methods in Lanthanide and Actinide Computational Chemistry*; Dolg, M., Ed.; John Wiley & Sons, 2015, pp 217−240.
(26) Mikami, M. Computational Chemistry Approach for White LED (Oxy)Nitride Phosphors. *ECS J. Solid State Sci. Technol.* **2013**, *2*, R3048−R3058.
(27) Du, M.-H. Using DFT Methods to Study Activators in Optical Materials. *ECS J. Solid State Sci. Technol.* **2016**, *5*, R3007−R3018.
(28) Park, W. B.; Singh, S. P.; Sohn, K.-S. Discovery of a Phosphor for Lighting Emitting Diode Applications and Its Structural Determination, $Ba(Si,Al)_5(O,N)_8:Eu^{2+}$. *J. Am. Chem. Soc.* **2014**, *136*, 2363−2373.
(29) Park, W. B.; Hong, S. U.; Singh, S. P.; Pyo, M.; Sohn, K.-S. Systematic Approach to Calculate the Band Gap Energy of A Disordered Compound with A Low Symmetry and Large Cell Size via Density Functional Theory. *ACS Omega* **2016**, *1*, 483−490.
(30) Curtarolo, S.; Hart, G. L. W.; Nardelli, M. B.; Mingo, N.; Sanvito, S.; Levy, O. The High-Throughput Highway to Computational Materials Design. *Nat. Mater.* **2013**, *12*, 191−201.
(31) Setyawan, W.; Gaume, R. M.; Lam, S.; Feigelson, R. S.; Curtarolo, S. High-Throughput Combinatorial Database of Electronic Band Structures for Inorganic Scintillator Materials. *ACS Comb. Sci.* **2011**, *13*, 382−390.
(32) Wang, D.; van Gunsteren, W. F.; Chai, Z. Recent Advances in Computational Actinoid Chemistry. *Chem. Soc. Rev.* **2012**, *41*, 5836−5865.
(33) Blasse, G.; Grabmaier, B. C. *Luminescent Materials*; Springer-Verlag: Berlin, 1994.
(34) Salah, N.; Habib, S. S.; Khan, Z. H. Quantum Effect on the Energy Levels of $Eu^{2+}$ Doped $K_2Ca_2(SO_4)_3$ Nanoparticles. *J. Fluoresc.* **2010**, *20*, 1009−1015.
(35) Terraschke, H.; Wickleder, C. UV, Blue, Green, Yellow, Red, and Small: Newest Developments on $Eu^{2+}$-Doped Nanophosphors. *Chem. Rev.* **2015**, *115*, 11352−11378.
(36) Li, Y.; Gecevicius, M.; Qiu, J. Long Persistent Phosphors−from Fundamentals to Applications. *Chem. Soc. Rev.* **2016**, *45*, 2090−2136.
(37) Zhang, C.; Lin, J. Defect-Related Luminescent Materials: Synthesis, Emission Properties and Applications. *Chem. Soc. Rev.* **2012**, *41*, 7938−7961.
(38) Liu, X.; Qiu, J. Recent Advances in Energy Transfer in Bulk and Nanoscale Luminescent Materials: from Spectroscopy to Applications. *Chem. Soc. Rev.* **2015**, *44*, 8714−8746.
(39) Bril, A.; Blasse, G.; de Poorter, J. A Fast-Decay Phosphors. *J. Electrochem. Soc.* **1970**, *117*, 346−348.
(40) Barry, T. L. Luminescent Properties of $Eu^{2+}$ and $Eu^{2+}$+$Mn^{2+}$ Activated $BaMg_2Si_2O_7$. *J. Electrochem. Soc.* **1970**, *117*, 381−385.
(41) Ronda, C. R. Phosphors for Lamps and Displays: An Applicational View. *J. Alloys Compd.* **1995**, *225*, 534−538.
(42) Kaczmarek, A. M.; Van Hecke, K.; Van Deun, R. Nano- and Micro-Sized Rare-Earth Carbonates and Their Use as Precursors and Sacrificial Templates for the Synthesis of New Innovative Materials. *Chem. Soc. Rev.* **2015**, *44*, 2032−2059.
(43) Li, C.; Lin, J. Rare Earth Fluoride Nano-/Microcrystals: Synthesis, Surface Modification and Application. *J. Mater. Chem.* **2010**, *20*, 6831−6847.
(44) Shang, M.; Li, C.; Lin, J. How to Produce White Light in A Single-Phase Host? *Chem. Soc. Rev.* **2014**, *43*, 1372−1386.
(45) Stevels, A. L. N.; Schrama-de Pauw, A. D. M. $Eu^{2+}$ Luminescence in Hexagonal Aluminates Containing Large Divalent or Trivalent Cations. *J. Electrochem. Soc.* **1976**, *123*, 691−697.
(46) Palilla, F. C.; Levine, A. K.; Tomkus, M. R. Fluorescent Properties of Alkaline Earth Aluminates of the Type $MAl_2O_4$ Activated by Divalent Europium. *J. Electrochem. Soc.* **1968**, *115*, 642−644.
(47) Xie, R. J.; Hirosaki, N. Silicon-Based Oxynitride and Nitride Phosphors for White LEDs-A Review. *Sci. Technol. Adv. Mater.* **2007**, *8*, 588−600.
(48) Song, H. J.; Yim, D. K.; Roh, H.-S.; Cho, I. S.; Kim, S.-J.; Jin, Y.-H.; Shim, H.-W.; Kim, D.-W.; Hong, K. S. $RbBaPO_4:Eu^{2+}$: A New Alternative Blue-Emitting Phosphor for UV-Based White Light-Emitting Diodes. *J. Mater. Chem. C* **2013**, *1*, 500−505.
(49) Kim, M.; Kobayashi, M.; Kato, H.; Yamane, H.; Sato, Y.; Kakihana, M. Crystal Structures and Luminescence Properties of $Eu^{2+}$-Activated New $NaBa_{0.5}Ca_{0.5}PO_4$ and $Na_3Ba_2Ca(PO_4)_3$. *Dalton Trans.* **2015**, *44*, 1900−1904.
(50) Nair, G. B.; Dhoble, S. J. Highly Enterprising Calcium Zirconium Phosphate $[CaZr_4(PO_4)_6:Dy^{3+}, Ce^{3+}]$ Phosphor for White Light Emission. *RSC Adv.* **2015**, *5*, 49235−49247.
(51) Yin, L.-J.; Chen, G.-Z.; Zhou, Z.-Y.; Jian, X.; Xu, B.; He, J.-H.; Tang, H.; Luan, C.-H.; Xu, X.; van Ommen, J. R.; et al. Improved Blue-


DOI: 10.1021/acs.chemrev.6b00691
*Chem. Rev.* XXXX, XXX, XXX−XXX

Emitting AlN:$Eu^{2+}$ Phosphors by Alloying with GaN. *J. Am. Ceram. Soc.* **2015**, *98*, 3897−3904.
(52) Streit, H.; Kramer, J.; Suta, M.; Wickleder, C. Red, Green, and Blue Photoluminescence of $Ba_2SiO_4$:M (M = $Eu^{3+}$, $Eu^{2+}$, $Sr^{2+}$) Nanophosphors. *Materials* **2013**, *6*, 3079−3093.
(53) Piao, X.; Machida, K.-i.; Horikawa, T.; Hanzawa, H.; Shimomura, Y.; Kijima, N. Preparation of $CaAlSiN_3$:$Eu^{2+}$ Phosphors by the Self-Propagating High-Temperature Synthesis and Their Luminescent Properties. *Chem. Mater.* **2007**, *19*, 4592−4599.
(54) Zhang, P.; Xu, M. X.; Zhao, J. W.; Qin, Y. X.; Lv, Y. W. Preparation of a New Red Long Afterglow Phosphor Strontium Aluminate Composition. *Key Eng. Mater.* **2007**, *336*−*338*, 616−618.
(55) Singh, S. K. Red and Near Infrared Persistent Luminescence Nano-Probes for Bioimaging and Targeting Applications. *RSC Adv.* **2014**, *4*, 58674−58698.
(56) Yamamoto, H.; Matsuzawa, T. Mechanism of Long Phosphorescence of $SrAl_2O_4$:$Eu^{2+}$, $Dy^{3+}$ and $CaAl_2O_4$:$Eu^{2+}$, $Nd^{3+}$. *J. Lumin.* **1997**, *72*-*74*, 287−289.
(57) Clabau, F.; Rocquefelte, X.; Jobic, S.; Deniard, P.; Whangbo, M.-H.; Garcia, A.; Le Mercier, T. Mechanism of Phosphorescence Appropriate for the Long-Lasting Phosphors $Eu^{2+}$-Doped $SrAl_2O_4$ with Codopants $Dy^{3+}$ and $B^{3+}$. *Chem. Mater.* **2005**, *17*, 3904−3912.
(58) Zhang, S.; Nakai, Y.; Tsuboi, T.; Huang, Y.; Seo, H. J. Luminescence and Microstructural Features of Eu-Activated $LiBaPO_4$ Phosphor. *Chem. Mater.* **2011**, *23*, 1216−1224.
(59) Chen, Y.; Li, Y.; Wang, J.; Wu, M.; Wang, C. Color-Tunable Phosphor of $Eu^{2+}$ and $Mn^{2+}$ Codoped $Ca_2Sr(PO_4)_2$ for UV Light-Emitting Diodes. *J. Phys. Chem. C* **2014**, *118*, 12494−12499.
(60) Ianoş, R.; Lazău, I.; Păcurariu, C.; Barvinschi, P. Fuel Mixture Approach for Solution Combustion Synthesis of $Ca_3Al_2O_6$ Powders. *Cem. Concr. Res.* **2009**, *39*, 566−572.
(61) Chen, Z.; Yan, Y. Nano-Sized PDP Phosphors Prepared by Solution Combustion Method. *J. Mater. Sci.* **2006**, *41*, 5793−5796.
(62) Zand, S. K.; Baghshahi, S.; Rajabi, M. Synthesis of $Sr_4Al_{14}O_{25}$:$Eu^{2+}$ Green Emitting Luminescent Nano-Pigment by Solution Combustion Method. *J. Mater. Sci.: Mater. Electron.* **2014**, *25*, 4412−4417.
(63) Qiu, Z.; Zhou, Y.; Lü, M.; Zhang, A.; Ma, Q. Combustion Synthesis of Long-Persistent Luminescent $MAl_2O_4$:$Eu^{2+}$,$R^{3+}$ (M = Sr, Ba, Ca, R = Dy, Nd and La) Nanoparticles and Luminescence Mechanism Research. *Acta Mater.* **2007**, *55*, 2615−2620.
(64) Krishna, R. H.; Nagabhushana, B. M.; Sherikar, B. N.; Murthy, N. S.; Shivakumarae, C.; Thomas, T. Luminescence Enhancement in Monoclinic $CaAl_2O_4$:$Eu^{2+}$, $Cr^{3+}$ Nanophosphor by Fuel-Blend Combustion Synthesis. *Chem. Eng. J.* **2015**, *267*, 317−323.
(65) Fu, Z.; Zhou, S.; Yu, Y.; Zhang, S. Combustion Synthesis and Luminescence Properties of Nanocrystalline Monoclinic $SrAl_2O_4$:$Eu^{2+}$. *Chem. Phys. Lett.* **2004**, *395*, 285−289.
(66) Yu, X.; Zhou, C.; He, X.; Peng, Z.; Yang, S.-P. The Influence of Some Processing Conditions on Luminescence of $SrAl_2O_4$:$Eu^{2+}$ Nanoparticles Produced by Combustion Method. *Mater. Lett.* **2004**, *58*, 1087−1091.
(67) Shang, M.; Li, G.; Geng, D.; Yang, D.; Kang, X.; Zhang, Y.; Lian, H.; Lin, J. Blue Emitting $Ca_8La_2(PO_4)_6O_2$:$Ce^{3+}$/$Eu^{2+}$ Phosphors with High Color Purity and Brightness for White LED: Soft-Chemical Synthesis, Luminescence, and Energy Transfer Properties. *J. Phys. Chem. C* **2012**, *116*, 10222−10231.
(68) Sameie, H.; Salimi, R.; Sabbagh Alvani, A. A.; Sarabi, A. A.; Moztarzadeh, F.; Tahriri, M. Evaluation of Sol−Gel Derived $Eu^{2+}$ Activated $SrMgAl_2SiO_7$ as A Novel Nanostructure Luminescent Pigment. *Phys. B* **2010**, *405*, 4796−4800.
(69) Ji, H.; Xie, G.; Lv, Y.; Lu, H. A New Phosphor with Flower-Like Structure and Luminescent Properties of $Sr_2MgSi_2O_7$: $Eu^{2+}$, $Dy^{3+}$ Long Afterglow Materials by Sol−Gel Method. *J. Sol-Gel Sci. Technol.* **2007**, *44*, 133−137.
(70) Lee, K. N.; Moon, J. H.; Oh, J. H.; Do, Y. R. Sol−Gel Synthesis of an Efficient Blue $CaMgSi_2O_6$: $Eu^{2+}$ Thin-Film Phosphor with Two-Dimensional Triangular-Lattice $SiN_x$ Air-Hole Photonic Crystal. *J. Electrochem. Soc.* **2009**, *156*, J283−J287.
(71) Miao, F.; He, D.; Wang, Y.; Fu, M.; Wu, Y.; Li, Y. Luminescence Properties of Nano-Sized $Sr_2MgSiO_5$:$Eu^{2+}$,$Mn^{2+}$ Phosphors Prepared by the Sol-Gel Method. *J. Nanosci. Nanotechnol.* **2011**, *11*, 9833−9835.
(72) Zhang, Y.; Feng, J.; Sai, Q.; Ma, M.; Yang, J.; Liu, Y. Sol-Gel Synthesis and Photoluminescence Characterization of $Ba_2SiO_4$:$Eu^{2+}$ Green Phosphors for White-LED Application. *Integr. Ferroelectr.* **2014**, *154*, 128−134.
(73) Wu, Z. C.; Shi, J. X.; Gong, M. L.; Wang, J.; Su, Q. Nanosized $LiSrPO_4$:$Eu^{2+}$ Phosphor with Blue-Emission Synthesized by the Sol−Gel Method. *Mater. Chem. Phys.* **2007**, *103*, 415−418.
(74) Yan, B.; Wu, J. Sol−Gel Composition of Multicomponent Hybrid Precursors to Long Afterglow of $Ca_xSr_{1-X}Al_2O_4$: $Eu^{2+}$ Phosphors. *Mater. Lett.* **2007**, *61*, 4851−4853.
(75) Peng, T.; Liu, H.; Yang, H.; Yan, C. Synthesis of $SrAl_2O_4$:Eu,Dy Phosphor Nanometer Powders by Sol−Gel Processes and Its Optical Properties. *Mater. Chem. Phys.* **2004**, *85*, 68−72.
(76) Hwang, K.-S.; Kang, B.-A.; Kim, S.-D.; Hwangbo, S.; Kim, J.-T. Cost-Effective Electrostatic-Sprayed $SrAl_2O_4$:$Eu^{2+}$ Phosphor Coatings by Using Salted Sol−Gel Derived Solution. *Bull. Mater. Sci.* **2011**, *34*, 1059−1062.
(77) Fan, L.; Zhao, X.; Zhang, S.; Ding, Y.; Li, Z.; Zou, Z. Enhanced Luminescence Intensity of $Sr_3B_2O_6$:$Eu^{2+}$ Phosphor Prepared by Sol−Gel Method. *J. Alloys Compd.* **2013**, *579*, 432−437.
(78) Hench, L. L.; West, J. K. The Sol-Gel Process. *Chem. Rev.* **1990**, *90*, 33−72.
(79) Ciriminna, R.; Fidalgo, A.; Pandarus, V.; Béland, F.; Ilharco, L. M.; Pagliaro, M. The Sol−Gel Route to Advanced Silica-Based Materials and Recent Applications. *Chem. Rev.* **2013**, *113*, 6592−6620.
(80) Wu, Y.-C.; Wang, D.-Y.; Chen, T.-M.; Lee, C.-S.; Chen, K.-J.; Kuo, H.-C. A Novel Tunable Green- to Yellow-Emitting $\beta$-YFS:$Ce^{3+}$ Phosphor for Solid-State Lighting. *ACS Appl. Mater. Interfaces* **2011**, *3*, 3195−3199.
(81) Saradhi, M. P.; Varadaraju, U. V. Photoluminescence Studies on $Eu^{2+}$-Activated $Li_2SrSiO_4$-a Potential Orange-Yellow Phosphor for Solid-State Lighting. *Chem. Mater.* **2006**, *18*, 5267−5272.
(82) Arunkumar, P.; Kim, Y. H.; Im, W. B. Versatile $Ca_4F_2Si_2O_7$ Host from Defect-Induced Host Emission to White-Light-Emitting $Ce^{3+}$-Doped $Ca_4F_2Si_2O_7$ Phosphor for Near-UV Solid-State Lighting. *J. Phys. Chem. C* **2016**, *120*, 4495−4503.
(83) Fu, X.; Lü, W.; Jiao, M.; You, H. Broadband Yellowish-Green Emitting $Ba_4Gd_3Na_3(PO_4)_6F_2$:$Eu^{2+}$ Phosphor: Structure Refinement, Energy Transfer, and Thermal Stability. *Inorg. Chem.* **2016**, *55*, 6107−6113.
(84) Xiao, W.; Zhang, X.; Hao, Z.; Pan, G.; Luo, Y.; Zhang, L.; Zhang, J. Blue-Emitting $K_2Al_2B_2O_7$:$Eu^{2+}$ Phosphor with High Thermal Stability and High Color Purity for Near-UV-Pumped White Light-Emitting Diodes. *Inorg. Chem.* **2015**, *54*, 3189−3195.
(85) Gwak, S. J.; Arunkumar, P.; Im, W. B. A New Blue-Emitting Oxohalide Phosphor $Sr_4OCl_6$:$Eu^{2+}$ for Thermally Stable, Efficient White-Light-Emitting Devices under Near-UV. *J. Phys. Chem. C* **2014**, *118*, 2686−2692.
(86) Sun, W.; Jia, Y.; Pang, R.; Li, H.; Ma, T.; Li, D.; Fu, J.; Zhang, S.; Jiang, L.; Li, C. $Sr_9Mg_{1.5}(PO_4)_7$:$Eu^{2+}$: A Novel Broadband Orange-Yellow-Emitting Phosphor for Blue Light-Excited Warm White LEDs. *ACS Appl. Mater. Interfaces* **2015**, *7*, 25219−25226.
(87) Seibald, M.; Rosenthal, T.; Oeckler, O.; Maak, C.; Tücks, A.; Schmidt, P. J.; Wiechert, D.; Schnick, W. New Polymorph of the Highly Efficient LED-Phosphor $SrSi_2O_2N_2$:$Eu^{2+}$−Polytypism of a Layered Oxonitridosilicate. *Chem. Mater.* **2013**, *25*, 1852−1857.
(88) Li, Y. Q.; Hirosaki, N.; Xie, R. J.; Takeda, T.; Mitomo, M. Yellow-Orange-Emitting $CaAlSiN_3$:$Ce^{3+}$ Phosphor: Structure, Photoluminescence, and Application in White LEDs. *Chem. Mater.* **2008**, *20*, 6704−6714.
(89) Wang, X.-M.; Wang, C.-H.; Kuang, X.-J.; Zou, R.-Q.; Wang, Y.-X.; Jing, X.-P. Promising Oxonitridosilicate Phosphor Host $Sr_3Si_2O_4N_2$: Synthesis, Structure, and Luminescence Properties Activated by $Eu^{2+}$ and $Ce^{3+}$/$Li^+$ for pc-LEDs. *Inorg. Chem.* **2012**, *51*, 3540−3547.


DOI: 10.1021/acs.chemrev.6b00691
*Chem. Rev.* XXXX, XXX, XXX−XXX

(90) Atuchin, V. V.; Beisel, N. F.; Galashov, E. N.; Mandrik, E. M.; Molokeev, M. S.; Yelisseyev, A. P.; Yusuf, A. A.; Xia, Z. Pressure-Stimulated Synthesis and Luminescence Properties of Microcrystalline $(Lu,Y)_3Al_5O_{12}:Ce^{3+}$ Garnet Phosphors. *ACS Appl. Mater. Interfaces* **2015**, *7*, 26235−26243.
(91) Luo, Y.; Xia, Z. Effect of Al/Ga Substitution on Photoluminescence and Phosphorescence Properties of Garnet-Type $Y_3Sc_2Ga_{3-x}Al_xO_{12}:Ce^{3+}$ Phosphor. *J. Phys. Chem. C* **2014**, *118*, 23297−23305.
(92) Li, K.; Shang, M.; Lian, H.; Lin, J. Photoluminescence Properties of Efficient Blue-Emitting Phosphor $\alpha$-$Ca_{1.65}Sr_{0.35}SiO_4:Ce^{3+}$: Color Tuning via the Substitutions of Si by Al/Ga/B. *Inorg. Chem.* **2015**, *54*, 7992−8002.
(93) Xia, Z.; Miao, S.; Chen, M.; Molokeev, M. S.; Liu, Q. Structure, Crystallographic Sites, and Tunable Luminescence Properties of $Eu^{2+}$ and $Ce^{3+}/Li^+$-Activated $Ca_{1.65}Sr_{0.35}SiO_4$ Phosphors. *Inorg. Chem.* **2015**, *54*, 7684−7691.
(94) Lv, W.; Jia, Y.; Zhao, Q.; Lü, W.; Jiao, M.; Shao, B.; You, H. Synthesis, Structure, and Luminescence Properties of $K_2Ba_7Si_{16}O_{40}:Eu^{2+}$ for White Light Emitting Diodes. *J. Phys. Chem. C* **2014**, *118*, 4649−4655.
(95) Xia, Z.; Wang, X.; Wang, Y.; Liao, L.; Jing, X. Synthesis, Structure, and Thermally Stable Luminescence of $Eu^{2+}$-Doped $Ba_2Ln(BO_3)_2Cl$ (Ln = Y, Gd and Lu) Host Compounds. *Inorg. Chem.* **2011**, *50*, 10134−10142.
(96) Yi, H.; Wu, L.; Wu, L.; Zhao, L.; Xia, Z.; Zhang, Y.; Kong, Y.; Xu, J. Crystal Structure of High-Temperature Phase $\beta$-$NaSrBO_3$ and Photoluminescence of $\beta$-$NaSrBO_3:Ce^{3+}$. *Inorg. Chem.* **2016**, *55*, 6487−6495.
(97) Huang, C.-H.; Chen, T.-M.; Liu, W.-R.; Chiu, Y.-C.; Yeh, Y.-T.; Jang, S.-M. A Single-Phased Emission-Tunable Phosphor $Ca_9Y(PO_4)_7:Eu^{2+},Mn^{2+}$ with Efficient Energy Transfer for White-Light-Emitting Diodes. *ACS Appl. Mater. Interfaces* **2010**, *2*, 259−264.
(98) Xia, Z.; Liu, R.-S. Tunable Blue-Green Color Emission and Energy Transfer of $Ca_2Al_3O_6F:Ce^{3+},Tb^{3+}$ Phosphors for Near-UV White LEDs. *J. Phys. Chem. C* **2012**, *116*, 15604−15609.
(99) Kim, D.; Jang, J.; Ahn, S. I.; Kim, S.-H.; Park, J.-C. Novel Blue-Emitting $Eu^{2+}$-Activated LaOCl:Eu Materials. *J. Mater. Chem. C* **2014**, *2*, 2799−2805.
(100) Anoop, G.; Lee, D. W.; Suh, D. W.; Wu, S. L.; Ok, K. M.; Yoo, J. S. Solid-State Synthesis, Structure, Second-Harmonic Generation, and Luminescent Properties of Noncentrosymmetric $BaSi_7N_{10}:Eu^{2+}$ Phosphors. *J. Mater. Chem. C* **2013**, *1*, 4705−4712.
(101) Tao, Z.; Huang, Y.; Seo, H. J. Blue Luminescence and Structural Properties of $Ce^{3+}$-Activated Phosphosilicate Apatite $Sr_5(PO_4)_2(SiO_4)$. *Dalton Trans.* **2013**, *42*, 2121−2129.
(102) Miao, S.; Xia, Z.; Molokeev, M. S.; Zhang, J.; Liu, Q. Crystal Structure Refinement and Luminescence Properties of Blue-Green-Emitting $CaSrAl_2SiO_7:Ce^{3+},Li^+,Eu^{2+}$ Phosphors. *J. Mater. Chem. C* **2015**, *3*, 8322−8328.
(103) Dai, W. B. Investigation of the Luminescent Properties of $Ce^{3+}$ Doped and $Ce^{3+}/Mn^{2+}$ Co-doped $CaAl_2Si_2O_8$ Phosphors. *RSC Adv.* **2014**, *4*, 11206−11215.
(104) Luo, H.; Liu, J.; Zheng, X.; Han, L.; Ren, K.; Yu, X. Enhanced Photoluminescence of $Sr_3SiO_5:Ce^{3+}$ and Tuneable Yellow Emission of $Sr_3SiO_5:Ce^{3+},Eu^{2+}$ by $Al^{3+}$ Charge Compensation for W-Leds. *J. Mater. Chem.* **2012**, *22*, 15887−15893.
(105) Cheng, B.; Zhang, Z.; Han, Z.; Xiao, Y.; Lei, S. $SrAl_2O_4:Eu^{2+},Dy^{3+}$ Nanobelts: Synthesis by Combustion and Properties of Long-Persistent Phosphorescence. *J. Mater. Res.* **2011**, *26*, 2311−2315.
(106) Peng, T.; Yang, H.; Pu, X.; Hu, B.; Jiang, Z.; Yan, C. Combustion Synthesis and Photoluminescence of $SrAl_2O_4$:Eu,Dy Phosphor Nanoparticles. *Mater. Lett.* **2004**, *58*, 352−356.
(107) Nguyen, M. S.; Ho, V. T.; Pham, N. T. T. The Synthesis of $BaMgAl_{10}O_{17}:Eu^{2+}$ Nanopowder by a Combustion Method and Its Luminescent Properties. *Adv. Nat. Sci.: Nanosci. Nanotechnol.* **2011**, *2*, 045005.
(108) Pradal, N.; Chadeyron, G.; Thérias, S.; Potdevin, A.; Santilli, C. V.; Mahiou, R. Investigation on Combustion Derived $BaMgAl_{10}O_{17}:Eu^{2+}$ Phosphor Powder and Its Corresponding PVP/$BaMgAl_{10}O_{17}:Eu^{2+}$ Nanocomposite. *Dalton Trans.* **2014**, *43*, 1072−1081.
(109) Zhao, C.; Chen, D.; Yuan, Y.; Wu, M. Synthesis of $Sr_4Al_{14}O_{25}:Eu^{2+},Dy^{3+}$ Phosphor Nanometer Powders by Combustion Processes and Its Optical Properties. *Mater. Sci. Eng., B* **2006**, *133*, 200−204.
(110) Stefani, R.; Maia, A.; de, S.; Kodaira, C. A.; Teotonio, E. E. S.; Felinto, M. C. F. C.; Brito, H. F. Highly Enhanced Luminescence of $SrB_4O_7:Eu^{2+}$ Phosphor Prepared by the Combustion Method Using Glycine as Fuel. *Opt. Mater.* **2007**, *29*, 1852−1855.
(111) Lei, B.; Machida, K.-i.; Horikawa, T.; Hanzawa, H. Facile Combustion Route for Low-Temperature Preparation of $Sr_2SiO_4:Eu^{2+}$ Phosphor and Its Photoluminescence Properties. *Jpn. J. Appl. Phys.* **2010**, *49*, 095001.
(112) Kim, J. S.; Mho, S. W.; Park, Y. H.; Kim, G. S.; Choi, J. C.; Park, H. L. White-Light-Emitting $Eu^{2+}$ and $Mn^{2+}$-Codoped Silicate Phosphors Synthesized through Combustion Process. *Solid State Commun.* **2005**, *136*, 504−507.
(113) Song, Y.; You, H.; Yang, M.; Zheng, Y.; Liu, K.; Jia, G.; Huang, Y.; Zhang, L.; Zhang, H. Facile Synthesis and Luminescence of $Sr_5(PO4)_3Cl:Eu^{2+}$ Nanorod Bundles via a Hydrothermal Route. *Inorg. Chem.* **2010**, *49*, 1674−1678.
(114) Zou, H.; Yan, M.; Wang, G.; Yuan, B.; Huang, J.; Gao, F.; Sheng, Y.; Zheng, K.; Song, Y. $Sr_5(PO_4)_3Cl:Eu^{2+}$ with Multiform Morphologies and Sizes: Hydrothermal Synthesis and Luminescent Properties. *Powder Technol.* **2014**, *254*, 579−582.
(115) Li, Y.; Xiao, L.; Liu, Y.; Ai, P.; Chen, X. Synthesis of Monodisperse Spherical Core-Shell $SiO_2$-$SrAl_2Si_2O_8:Eu^{2+}$ Phosphors by Hydrothermal Homogeneous Precipitation Method. *Sci. Technol. Adv. Mater.* **2010**, *11*, 045003.
(116) Kutty, T. R. N.; Jagannathan, R.; Rao, R. P. Luminescence of $Eu^{2+}$ in Strontium Aluminates Prepared by the Hydrothermal Method. *Mater. Res. Bull.* **1990**, *25*, 1355−1362.
(117) Zhu, G.; Xie, M.; Yang, Q.; Liu, Y. Hydrothermal Synthesis and Spectral Properties of $Ce^{3+}$ and $Eu^{2+}$ Ions Doped $KMgF_3$ Phosphor. *Opt. Laser Technol.* **2016**, *81*, 162−167.
(118) Lu, Z.; Weng, L.; Song, S.; Zhang, P.; Luo, X.; Ren, X. Controlled Synthesis of $Eu^{2+}$-Doped Barium Silicate Nanostructures and Their Optical Properties. *Ceram. Int.* **2012**, *38*, 5305−5310.
(119) Chen, W.; Malm, J.-O.; Zwiller, V.; Huang, Y.; Liu, S.; Wallenberg, R.; Bovin, J.-O.; Samuelson, L. Energy Structure and Fluorescence of $Eu^{2+}$ in ZnS:Eu Nanoparticles. *Phys. Rev. B: Condens. Matter Mater. Phys.* **2000**, *61*, 11021−11024.
(120) Chen, W.; Malm, J.-O.; Zwiller, V.; Wallenberg, R.; Bovin, J.-O. Size Dependence of $Eu^{2+}$ Fluorescence in $ZnS:Eu^{2+}$ Nanoparticles. *J. Appl. Phys.* **2001**, *89*, 2671−2675.
(121) Chang, C.; Xu, J.; Jiang, L.; Mao, D.; Ying, W. Luminescence of Long-Lasting $CaAl_2O_4:Eu^{2+},Nd^{3+}$ Phosphor by Co-Precipitation Method. *Mater. Chem. Phys.* **2006**, *98*, 509−513.
(122) Birkel, A.; Denault, K. A.; George, N. C.; Doll, C. E.; Héry, B.; Mikhailovsky, A. A.; Birkel, C. S.; Hong, B.-C.; Seshadri, R. Rapid Microwave Preparation of Highly Efficient $Ce^{3+}$-Substituted Garnet Phosphors for Solid State White Lighting. *Chem. Mater.* **2012**, *24*, 1198−1204.
(123) Zhang, P.; Xu, M.-X.; Zheng, Z.-T.; Sun, B.; Zhang, Y.-H. Microwave Synthesis and Characterization of New Red Long Afterglow Phosphor $Sr_3Al_2O_6$:Eu. *Trans. Nonferrous Met. Soc. China* **2006**, *16*, s423−s425.
(124) Zhang, P.; Li, L.; Xu, M.; Liu, L. The New Red Luminescent $Sr_3Al_2O_6:Eu^{2+}$ Phosphor Powders Synthesized via Sol−Gel Route by Microwave-Assisted. *J. Alloys Compd.* **2008**, *456*, 216−219.
(125) Du, H.; Sun, J.; Xia, Z.; Sun, J. Luminescence Properties of $Ba_2Mg(BO_3)_2:Eu^{2+}$ Red Phosphors Synthesized by a Microwave-Assisted Sol-Gel Route. *J. Electrochem. Soc.* **2009**, *156*, J361−J366.
(126) Xu, X.; Tang, J.; Nishimura, T.; Hao, L. Synthesis of Ca-$\alpha$-SiAlON Phosphors by a Mechanochemical Activation Route. *Acta Mater.* **2011**, *59*, 1570−1576.


DOI: 10.1021/acs.chemrev.6b00691
*Chem. Rev.* XXXX, XXX, XXX−XXX

(127) Yin, L.-J.; Xie, W.-J.; Jian, X.; Feng, Y.-Y.; Tang, H.; Luan, C.-H.; Liang, Y.-L.; Wang, C.; Xu, X. Luminescent Properties of a Novel $Al_{10}O_3N_8:Eu^{2+}$ Phosphor by a Mechanochemical Activation Route. *Opt. Mater.* **2015**, *42*, 511−515.
(128) Wang, X.; Riesen, H. Mechanochemical Synthesis of an Efficient Nanocrystalline $BaFBr:Eu^{2+}$ X-Ray Storage Phosphor. *RSC Adv.* **2015**, *5*, 85506−85510.
(129) McMillen, C. D.; Kolis, J. W. Hydrothermal Synthesis as a Route to Mineralogically-Inspired Structures. *Dalton Trans.* **2016**, *45*, 2772−2784.
(130) Wang, F.; Liu, X. Recent Advances in the Chemistry of Lanthanide-Doped Upconversion Nanocrystals. *Chem. Soc. Rev.* **2009**, *38*, 976−989.
(131) Wang, G.; Peng, Q. Tunable Photoluminescence of $NaYF_4:Eu$ Nanocrystals by $Sr^{2+}$ Codoping. *J. Solid State Chem.* **2011**, *184*, 59−63.
(132) Su, Y.; Li, L.; Li, G. $NaYF_4:Eu^{2+}$ Microcrystals: Synthesis and Intense Blue Luminescence. *Cryst. Growth Des.* **2008**, *8*, 2678−2683.
(133) Rauf, A.; Farshori, N. N. *Microwave-Induced Synthesis of Aromatic Heterocycles*; SpringerBriefs in Molecular Science. Green Chemistry for Sustainability; Springer: Dordrecht, 2012.
(134) McNaught, A. D.; Wilkinson, A. Pure; International Union of Pure and Applied Chemistry. *Compendium of Chemical Terminology: IUPAC Recommendations*, 2nd ed.; Blackwell Science: Oxford, England, 1997.
(135) Baláž, P.; Achimovičová, M.; Baláž, M.; Billik, P.; Cherkezova-Zheleva, Z.; Criado, J. M.; Delogu, F.; Dutková, E.; Gaffet, E.; Gotor, F. J.; et al. Hallmarks of Mechanochemistry: from Nanoparticles to Technology. *Chem. Soc. Rev.* **2013**, *42*, 7571−7637.
(136) Ashoori, R. C. Electrons in Artificial Atoms. *Nature* **1996**, *379*, 413−419.
(137) Gai, S.; Li, C.; Yang, P.; Lin, J. Recent Progress in Rare Earth Micro/Nanocrystals: Soft Chemical Synthesis, Luminescent Properties, and Biomedical Applications. *Chem. Rev.* **2014**, *114*, 2343−2389.
(138) Yoshimura, F.; Nakamura, K.; Wakai, F.; Hara, M.; Yoshimoto, M.; Odawara, O.; Wada, H. Preparation of Long-Afterglow Colloidal Solution of $Sr_2MgSi_2O_7$: $Eu^{2+}$,$Dy^{3+}$ by Laser Ablation in Liquid. *Appl. Surf. Sci.* **2011**, *257*, 2170−2175.
(139) Yoshimura, F.; Ishizaki, M.; Wakai, F.; Hara, M.; Odawara, O.; Wada, H. Optical Properties of Afterglow Nanoparticles $Sr_2MgSi_2O_7:Eu^{2+}$,$Dy^{3+}$ Capped with Polyethylene Glycol. *Adv. Opt. Technol.* **2012**, *2012*, 10.1155/2012/814745.
(140) Park, G. S.; Kim, K. M.; Mhin, S.; Koshizaki, N.; Eun, J. W.; Shim, K. B.; Ryu, J. H. Simple Route for $Y_3Al_5O_{12}:Ce^{3+}$ Colloidal Nanocrystal via Laser Ablation in Deionized Water and Its Luminescence. *Electrochem. Solid-State Lett.* **2008**, *11*, J23−J26.
(141) Amans, D.; Malaterre, C.; Diouf, M.; Mancini, C.; Chaput, F.; Ledoux, G.; Breton, G.; Guillin, Y.; Dujardin, C.; Masenelli-Varlot, K.; et al. Synthesis of Oxide Nanoparticles by Pulsed Laser Ablation in Liquids Containing a Complexing Molecule: Impact on Size Distributions and Prepared Phases. *J. Phys. Chem. C* **2011**, *115*, 5131−5139.
(142) Lu, C.-H.; Chen, S.-Y.; Hsu, C.-H. Nanosized Strontium Aluminate Phosphors Prepared via a Reverse Microemulsion Route. *Mater. Sci. Eng., B* **2007**, *140*, 218−221.
(143) Syu, J.-R.; Kumar, S.; Das, S.; Lu, C.-H. Microemulsion-Mediated Synthesis and Characterization of $YBO_3:Ce^{3+}$ Phosphors. *J. Am. Ceram. Soc.* **2012**, *95*, 1814−1817.
(144) Liu, Y.; Goebl, J.; Yin, Y. Templated Synthesis of Nanostructured Materials. *Chem. Soc. Rev.* **2013**, *42*, 2610−2653.
(145) Chen, X.; Ma, C.; Li, X.; Shi, C.; Li, X.; Lu, D. Novel Necklace-like $MAl_2O_4:Eu^{2+}$,$Dy^{3+}$(M = Sr, Ba, Ca) Phosphors via a CTAB-Assisted Solution-Phase Synthesis and Postannealing Approach. *J. Phys. Chem. C* **2009**, *113*, 2685−2689.
(146) Tan, X. Fabrication and Properties of $Sr_2MgSi_2O_7:Eu^{2+}$,$Dy^{3+}$ Nanostructures by an AAO Template Assisted Co-Deposition Method. *J. Alloys Compd.* **2009**, *477*, 648−651.
(147) Park, I. J.; Roh, H.-S.; Song, H. J.; Kim, D. H.; Kim, J. S.; Seong, W. M.; Kim, D.-W.; Hong, K. S. $\gamma$-$Al_2O_3$ Nanospheres-Directed Synthesis of Monodispersed $BaAl_2O_4:Eu^{2+}$ Nanosphere Phosphors. *CrystEngComm* **2013**, *15*, 4797−4801.
(148) Tang, J.-Y.; Yang, X.-F.; Cheng, Z.; Hao, L.-Y.; Xu, X.; Zhang, W.-H. Synthesis and Luminescence Properties of Highly Uniform Spherical $SiO_2@SrSi_2O_2N_2:Eu^{2+}$ Core-Shell Structured Phosphors. *J. Mater. Chem.* **2012**, *22*, 488−494.
(149) Song, Y.; Li, Z.; Ma, C. A Novel Single-Source Precursor Route for the Synthesis of Blue-Green Phosphor $SrS:Ce^{3+}$. *Bull. Korean Chem. Soc.* **2014**, *35*, 2148−2150.
(150) Zhao, Y.; Rabouw, F. T.; van Puffelen, T.; van Walree, C. A.; Gamelin, D. R.; de Mello Donegá, C.; Meijerink, A. Lanthanide-Doped CaS and SrS Luminescent Nanocrystals: A Single-Source Precursor Approach for Doping. *J. Am. Chem. Soc.* **2014**, *136*, 16533−16543.
(151) Zeuner, M.; Schmidt, P. J.; Schnick, W. One-Pot Synthesis of Single-Source Precursors for Nanocrystalline LED Phosphors $M_2Si_5N_8:Eu^{2+}$(M = Sr, Ba). *Chem. Mater.* **2009**, *21*, 2467−2473.
(152) Dorenbos, P. The 5d Level Positions of the Trivalent Lanthanides in Inorganic Compounds. *J. Lumin.* **2000**, *91*, 155−176.
(153) Jørgensen, C. K. *Modern Aspects of Ligand Field Theory*; Elsevier: New York, 1971.
(154) van der Kolk, E.; Dorenbos, P.; Vink, A. P.; Perego, R. C.; van Eijk, C. W. E.; Lakshmanan, A. R. Vacuum Ultraviolet Excitation and Emission Properties of $Pr^{3+}$ and $Ce^{3+}$ in $MSO_4$ (M = Ba, Sr, and Ca) and Predicting Quantum Splitting by $Pr^{3+}$ in Oxides and Fluorides. *Phys. Rev. B: Condens. Matter Mater. Phys.* **2001**, *64*, 195129.
(155) Morrison, C. A. Host Dependence of the Rare-Earth Ion Energy Separation $4f^N-4f^{N-1}$ *nl*. *J. Chem. Phys.* **1980**, *72*, 1001−1002.
(156) Aull, B. F.; Jenssen, H. P. Impact of Ion-Host Interactions on the 5d-4f Spectra of Lanthanide Rare-Earth-Metal Ions. I. A Phenomenological Crystal-Field Model. *Phys. Rev. B: Condens. Matter Mater. Phys.* **1986**, *34*, 6640−6646.
(157) Dorenbos, P. Relating the Energy of the $[Xe]5d^1$ Configuration of $Ce^{3+}$ in Inorganic Compounds with Anion Polarizability and Cation Electronegativity. *Phys. Rev. B: Condens. Matter Mater. Phys.* **2002**, *65*, 235110.
(158) Dorenbos, P. A Review on How Lanthanide Impurity Levels Change with Chemistry and Structure of Inorganic Compounds. *ECS J. Solid State Sci. Technol.* **2013**, *2*, R3001−R3011.
(159) Görller-Walrand, C.; Binnemans, K. *In Handbook on the Physics and Chemistry of Rare Earths*; Gschneidner, K. A., Eyring, L., Eds.; Elsevier Science BV: Amsterdam, 1998.
(160) Marder, M. P. *Condensed Matter Physics*; John Wiley & Sons: New York, 2000.
(161) Tully, J. C. Perspective on "Zur Quantentheorie der Molekeln. In *Theoretical Chemistry Accounts: New Century Issue*; Cramer, C. J., Truhlar, D. G., Eds.; Springer: New York, 2001; Vol. *103*, 173−176.
(162) Hartree, D. R. The Wave Mechanics of an Atom with a Non-Coulomb Central Field. Part I. Theory and Methods. *Math. Proc. Cambridge Philos. Soc.* **1928**, *24*, 89−110.
(163) Fock, V. Näherungsmethode zur Lösung des quantenmechanischen Mehrkörperproblems. *Eur. Phys. J. A* **1930**, *61*, 126−148.
(164) Slater, J. C. Note on Hartree's Method. *Phys. Rev.* **1930**, *35*, 210−211.
(165) Friesner, R. A. Ab Initio Quantum Chemistry: Methodology and Applications. *Proc. Natl. Acad. Sci. U. S. A.* **2005**, *102*, 6648−6653.
(166) Head-Gordon, M.; Pople, J. A.; Frisch, M. J. MP2 Energy Evaluation by Direct Methods. *Chem. Phys. Lett.* **1988**, *153*, 503−506.
(167) Roos, B. O.; Taylor, P. R.; Si≐gbahn, P. E. M. A Complete Active Space SCF Method (CASSCF) Using a Density Matrix Formulated Super-CI Approach. *Chem. Phys.* **1980**, *48*, 157−173.
(168) Friedman, H. G., Jr.; Choppin, G. R.; Feuerbacher, D. G. The Shapes of the f Orbitals. *J. Chem. Educ.* **1964**, *41*, 354.
(169) Andersson, K.; Malmqvist, P.-Å.; Roos, B. O. Second-Order Perturbation Theory with a Complete Active Space Self-Consistent Field Reference Function. *J. Chem. Phys.* **1992**, *96*, 1218−1226.
(170) Coates, R.; Coreno, M.; DeSimone, M.; Green, C. J.; Kaltsoyannis, N.; Kerridge, A.; Narband, N.; Sella, A. A Mystery Solved? Photoelectron Spectroscopic and Quantum Chemical Studies of the Ion States of $CeCP_3^+$. *Dalton Trans.* **2009**, 5943−5953.


DOI: 10.1021/acs.chemrev.6b00691
*Chem. Rev.* XXXX, XXX, XXX−XXX

(171) Luzon, J.; Sessoli, R. Lanthanides in Molecular Magnetism: so Fascinating, so Challenging. *Dalton Trans.* **2012**, *41*, 13556−13567.
(172) Koch, W.; Holthausen, M. C. *A Chemist's Guide to Density Functional Theory*; Wiley-VCH: Weinheim, 2000.
(173) Parr, R. G.; Yang, W. *Density-Functional Theory of Atoms and Molecules*; Oxford University: New York, 1989.
(174) Kohn, W.; Sham, L. J. Self-Consistent Equations Including Exchange and Correlation Effects. *Phys. Rev.* **1965**, *140*, A1133−A1138.
(175) Perdew, J. P.; Zunger, A. Self-Interaction Correction to Density-Functional Approximations for Many-Electron Systems. *Phys. Rev. B: Condens. Matter Mater. Phys.* **1981**, *23*, 5048−5079.
(176) Perdew, J. P.; Wang, Y. Accurate and Simple Analytic Representation of the Electron-Gas Correlation Energy. *Phys. Rev. B: Condens. Matter Mater. Phys.* **1992**, *45*, 13244−13249.
(177) Perdew, J. P.; Burke, K.; Ernzerhof, M. Generalized Gradient Approximation Made Simple. *Phys. Rev. Lett.* **1996**, *77*, 3865−3868.
(178) Tran, F.; Blaha, P. Accurate Band Gaps of Semiconductors and Insulators with a Semilocal Exchange-Correlation Potential. *Phys. Rev. Lett.* **2009**, *102*, 226401.
(179) Anisimov, V. I.; Aryasetiawan, F.; Lichtenstein, A. I. First-Principles Calculations of the Electronic Structure and Spectra of Strongly Correlated Systems: The LDA + U Method. *J. Phys.: Condens. Matter* **1997**, *9*, 767.
(180) Adamo, C.; Barone, V. Toward Reliable Density Functional Methods Without Adjustable Parameters: The PBE0Model. *J. Chem. Phys.* **1999**, *110*, 6158−6170.
(181) Krukau, A. V.; Vydrov, O. A.; Izmaylov, A. F.; Scuseria, G. E. Influence of the Exchange Screening Parameter on the Performance of Screened Hybrid Functionals. *J. Chem. Phys.* **2006**, *125*, 224106.
(182) Wu, Q.; Van Voorhis, T. Constrained Density Functional Theory and Its Application in Long-Range Electron Transfer. *J. Chem. Theory Comput.* **2006**, *2*, 765−774.
(183) Kaduk, B.; Kowalczyk, T.; Van Voorhis, T. Constrained Density Functional Theory. *Chem. Rev.* **2012**, *112*, 321−370.
(184) Hedin, L. New Method for Calculating the One-Particle Green's Function with Application to the Electron-Gas Problem. *Phys. Rev.* **1965**, *139*, A796−A823.
(185) Aryasetiawan, F.; Gunnarsson, O. The GW method. *Rep. Prog. Phys.* **1998**, *61*, 237.
(186) Salpeter, E. E.; Bethe, H. A. A Relativistic Equation for Bound-State Problems. *Phys. Rev.* **1951**, *84*, 1232−1242.
(187) Brgoch, J.; DenBaars, S. P.; Seshadri, R. Proxies from Ab Initio Calculations for Screening Efficient $Ce^{3+}$ Phosphor Hosts. *J. Phys. Chem. C* **2013**, *117*, 17955−17959.
(188) Bachmann, V.; Ronda, C.; Meijerink, A. Temperature Quenching of Yellow $Ce^{3+}$ Luminescence in YAG:Ce. *Chem. Mater.* **2009**, *21*, 2077−2084.
(189) Denault, K. A.; Brgoch, J.; Kloß, S. D.; Gaultois, M. W.; Siewenie, J.; Page, K.; Seshadri, R. Average and Local Structure, Debye Temperature, and Structural Rigidity in Some Oxide Compounds Related to Phosphor Hosts. *ACS Appl. Mater. Interfaces* **2015**, *7*, 7264−7272.
(190) Fu, Z.; Zhou, S.; Pan, T.; Zhang, S. Band Structure Calculations on the Monoclinic Bulk and Nano-$SrAl_2O_4$ Crystals. *J. Solid State Chem.* **2005**, *178*, 230−233.
(191) Botterman, J.; Joos, J. J.; Smet, P. F. Trapping and Detrapping in $SrAl_2O_4$:Eu,Dy Persistent Phosphors: Influence of Excitation Wavelength and Temperature. *Phys. Rev. B: Condens. Matter Mater. Phys.* **2014**, *90*, 085147.
(192) Brgoch, J.; Borg, C. K. H.; Denault, K. A.; Mikhailovsky, A.; DenBaars, S. P.; Seshadri, R. An Efficient, Thermally Stable Cerium-Based Silicate Phosphor for Solid State White Lighting. *Inorg. Chem.* **2013**, *52*, 8010−8016.
(193) Im, W. B.; George, N.; Kurzman, J.; Brinkley, S.; Mikhailovsky, A.; Hu, J.; Chmelka, B. F.; DenBaars, S. P.; Seshadri, R. Efficient and Color-Tunable Oxyfluoride Solid Solution Phosphors for Solid-State White Lighting. *Adv. Mater.* **2011**, *23*, 2300−2305.
(194) Im, W. B.; Brinkley, S.; Hu, J.; Mikhailovsky, A.; DenBaars, S. P.; Seshadri, R. $Sr_{2.975-x}Ba_xCe_{0.025}AlO_4F$: A Highly Efficient Green-Emitting Oxyfluoride Phosphor for Solid State White Lighting. *Chem. Mater.* **2010**, *22*, 2842−2849.
(195) George, N. C.; Birkel, A.; Brgoch, J.; Hong, B.-C.; Mikhailovsky, A. A.; Page, K.; Llobet, A.; Seshadri, R. Average and Local Structural Origins of the Optical Properties of the Nitride Phosphor $La_{3-x}Ce_xSi_6N_{11}$ ($0 < x \leq 3$). *Inorg. Chem.* **2013**, *52*, 13730−13741.
(196) Ha, J.; Wang, Z.; Novitskaya, E.; Hirata, G. A.; Graeve, O. A.; Ong, S. P.; McKittrick, J. An Integrated First Principles and Experimental Investigation of the Relationship between Structural Rigidity and Quantum Efficiency in Phosphors for Solid State Lighting. *J. Lumin.* **2016**, *179*, 297−305.
(197) Mishra, K. C.; Hannah, M. E.; Piquette, A.; Eyert, V.; Schmidt, P. C.; Johnson, K. H. First-Principles Investigation of the Luminescence Mechanism of $Eu^{2+}$ in $M_2SiO_4$:$Eu^{2+}$ (M = Ba, Sr). *ECS J. Solid State Sci. Technol.* **2012**, *1*, R87−R91.
(198) Han, J. K.; Hannah, M. E.; Piquette, A.; Talbot, J. B.; Mishra, K. C.; McKittrick, J. Nano- and Submicron Sized Europium Activated Silicate Phosphors Prepared by a Modified Co-Precipitation Method. *ECS J. Solid State Sci. Technol.* **2012**, *1*, R98−R102.
(199) Han, J. K.; Hannah, M. E.; Piquette, A.; Hirata, G. A.; Talbot, J. B.; Mishra, K. C.; McKittrick, J. Structure Dependent Luminescence Characterization of Green−Yellow Emitting $Sr_2SiO_4$:$Eu^{2+}$ Phosphors for Near UV Leds. *J. Lumin.* **2012**, *132*, 106−109.
(200) Cervantes-Vásquez, D.; Contreras, O. E.; Hirata, G. A. Quantum Efficiency of Silica-Coated Rare-Earth Doped Yttrium Silicate. *J. Lumin.* **2013**, *143*, 226−232.
(201) Wang, Z.; Chu, I.-H.; Zhou, F.; Ong, S. P. Electronic Structure Descriptor for the Discovery of Narrow-Band Red-Emitting Phosphors. *Chem. Mater.* **2016**, *28*, 4024−4031.
(202) Duan, C. J.; Wang, X. J.; Otten, W. M.; Delsing, A. C. A.; Zhao, J. T.; Hintzen, H. T. Preparation, Electronic Structure, and Photoluminescence Properties of $Eu^{2+}$- and $Ce^{3+}$/$Li^+$-Activated Alkaline Earth Silicon Nitride $MSiN_2$ (M = Sr, Ba). *Chem. Mater.* **2008**, *20*, 1597−1605.
(203) Uheda, K.; Hirosaki, N.; Yamamoto, Y.; Naito, A.; Nakajima, T.; Yamamoto, H. Luminescence Properties of a Red Phosphor, $CaAlSiN_3$:$Eu^{2+}$, for White Light-Emitting Diodes. *Electrochem. Solid-State Lett.* **2006**, *9*, H22−H25.
(204) van Loef, E. V. D.; Dorenbos, P.; van Eijk, C. W. E.; Krämer, K.; Güdel, H. U. High-Energy-Resolution Scintillator: $Ce^{3+}$ Activated $LaCl_3$. *Appl. Phys. Lett.* **2000**, *77*, 1467−1468.
(205) Dorenbos, P.; de Haas, J. T. M.; van Eijk, C. W. E. Gamma Ray Spectroscopy with a Φ19 × 19 $mm^3$ $LaBr_3$:0.5% $Ce^{3+}$ Scintillator. *IEEE Trans. Nucl. Sci.* **2004**, *51*, 1289−1296.
(206) Matsuzawa, T.; Aoki, Y.; Takeuchi, N.; Murayama, Y. A New Long Phosphorescent Phosphor with High Brightness, $SrAl_2O_4$:$Eu^{2+}$,$Dy^{3+}$. *J. Electrochem. Soc.* **1996**, *143*, 2670−2673.
(207) Lin, Y.; Tang, Z.; Zhang, Z.; Wang, X.; Zhang, J. Preparation of a New Long Afterglow Blue-Emitting $Sr_2MgSi_2O_7$-Based Photoluminescent Phosphor. *J. Mater. Sci. Lett.* **2001**, *20*, 1505−1506.
(208) Suyver, J. F.; Grimm, J.; van Veen, M. K.; Biner, D.; Krämer, K. W.; Güdel, H. U. Upconversion Spectroscopy and Properties of $NaYF_4$ Doped $Er^{3+}$, $Tm^{3+}$ and/or $Yb^{3+}$. *J. Lumin.* **2006**, *117*, 1−12.
(209) Braun, C.; Seibald, M.; Börger, S. L.; Oeckler, O.; Boyko, T. D.; Moewes, A.; Miehe, G.; Tücks, A.; Schnick, W. Material Properties and Structural Characterization of $M_3Si_6O_{12}N_2$:$Eu^{2+}$ (M = Ba, Sr)-A Comprehensive Study on a Promising Green Phosphor for pc-LEDs. *Chem.−Eur. J.* **2010**, *16*, 9646−9657.
(210) Wen, D.; Kuwahara, H.; Kato, H.; Kobayashi, M.; Sato, Y.; Masaki, T.; Kakihana, M. Anomalous Orange Light-Emitting $(Sr,Ba)_2SiO_4$:$Eu^{2+}$ Phosphors for Warm White LEDs. *ACS Appl. Mater. Interfaces* **2016**, *8*, 11615−11620.
(211) Shi, R.; Qi, M.; Ning, L.; Pan, F.; Zhou, L.; Zhou, W.; Huang, Y.; Liang, H. Combined Experimental and ab Initio Study of Site Preference of $Ce^{3+}$ in $SrAl_2O_4$. *J. Phys. Chem. C* **2015**, *119*, 19326−19332.


DOI: 10.1021/acs.chemrev.6b00691
*Chem. Rev.* XXXX, XXX, XXX−XXX

(212) Tsai, Y.-T.; Chiang, C.-Y.; Zhou, W.; Lee, J.-F.; Sheu, H.-S.; Liu, R.-S. Structural Ordering and Charge Variation Induced by Cation Substitution in (Sr,Ca)$AlSiN_3$:Eu Phosphor. *J. Am. Chem. Soc.* **2015**, *137*, 8936−8939.
(213) Marsman, M.; Andriessen, J.; van Eijk, C. W. E. Structure, Optical Absorption, and Luminescence Energy Calculations of $Ce^{3+}$ Defects in $LiBaF_3$. *Phys. Rev. B: Condens. Matter Mater. Phys.* **2000**, *61*, 16477−16490.
(214) Furman, J. D.; Melot, B. C.; Teat, S. J.; Mikhailovsky, A. A.; Cheetham, A. K. Towards Enhanced Ligand-Centred Photoluminescence in Inorganic-Organic Frameworks for Solid State Lighting. *Phys. Chem. Chem. Phys.* **2011**, *13*, 7622−7629.
(215) Hill, R. The Elastic Behaviour of a Crystalline Aggregate. *Proc. Phys. Soc., London, Sect. A* **1952**, *65*, 349.
(216) Delhaès, P. *Graphite and precursors*; Gordon and Breach: Amsterdam, The Netherlands, 2001.
(217) Ashcroft, N. W.; Mermin, N. D. *Solid State Physics*; Holt, Rinehart and Winston: New York, 1976.
(218) Francisco, E.; Recio, J. M.; Blanco, M. A.; Pendás, A. M.; Costales, A. Quantum-Mechanical Study of Thermodynamic and Bonding Properties of $MgF_2$. *J. Phys. Chem. A* **1998**, *102*, 1595−1601.
(219) Francisco, E.; Blanco, M. A.; Sanjurjo, G. Atomistic Simulation of $SrF_2$ Polymorphs. *Phys. Rev. B: Condens. Matter Mater. Phys.* **2001**, *63*, 094107.
(220) Beghi, M. G.; Bottani, C. E.; Russo, V. Debye Temperature of Erbium-Doped Yttrium Aluminum Garnet from Luminescence and Brillouin Scattering Data. *J. Appl. Phys.* **2000**, *87*, 1769−1774.
(221) Hermus, M.; Phan, P.-C.; Brgoch, J. Ab Initio Structure Determination and Photoluminescent Properties of an Efficient, Thermally Stable Blue Phosphor, $Ba_2Y_5B_5O_{17}:Ce^{3+}$. *Chem. Mater.* **2016**, *28*, 1121−1127.
(222) Ueda, J.; Dorenbos, P.; Bos, A. J. J.; Meijerink, A.; Tanabe, S. Insight into the Thermal Quenching Mechanism for $Y_3Al_5O_{12}:Ce^{3+}$ through Thermoluminescence Excitation Spectroscopy. *J. Phys. Chem. C* **2015**, *119*, 25003−25008.
(223) Denault, K. A.; Brgoch, J.; Gaultois, M. W.; Mikhailovsky, A.; Petry, R.; Winkler, H.; DenBaars, S. P.; Seshadri, R. Consequences of Optimal Bond Valence on Structural Rigidity and Improved Luminescence Properties in $Sr_xBa_{2-x}SiO_4:Eu^{2+}$ Orthosilicate Phosphors. *Chem. Mater.* **2014**, *26*, 2275−2282.
(224) Lin, Y.-C.; Karlsson, M.; Bettinelli, M. Inorganic Phosphor Materials for Lighting. *Top. Curr. Chem.* **2016**, *374*, 21.
(225) Dorenbos, P. The $4f^n \leftrightarrow 4f^{n-1}5d$ Transitions of the Trivalent Lanthanides in Halogenides and Chalcogenides. *J. Lumin.* **2000**, *91*, 91−106.
(226) Andriessen, J.; van der Kolk, E.; Dorenbos, P. Lattice Relaxation Study of the 4f-5d Excitation of $Ce^{3+}$-Doped $LaCl_3$, $LaBr_3$, and $NaLaF_4$: Stokes Shift by Pseudo Jahn-Teller Effect. *Phys. Rev. B: Condens. Matter Mater. Phys.* **2007**, *76*, 075124.
(227) Bagatur'yants, A. A.; Iskandarova, I. M.; Knizhnik, A. A.; Mironov, V. S.; Potapkin, B. V.; Srivastava, A. M.; Sommerer, T. J. Energy Level Structure of 4f5d States and the Stokes Shift in $LaPO_4:Pr^{3+}$: A Theoretical Study. *Phys. Rev. B: Condens. Matter Mater. Phys.* **2008**, *78*, 165125.
(228) Gettinger, C. L.; Heeger, A. J.; Drake, J. M.; Pine, D. J. The Effect of Intrinsic Rigidity on the Optical Properties of PPV Derivatives. *Mol. Cryst. Liq. Cryst. Sci. Technol., Sect. A* **1994**, *256*, 507−512.
(229) Li, G.; Lin, C. C.; Chen, W. T.; Molokeev, M. S.; Atuchin, V. V.; Chiang, C.-Y.; Zhou, W.; Wang, C.-W.; Li, W.-H.; Sheu, H.-S.; et al. Photoluminescence Tuning via Cation Substitution in Oxonitridosilicate Phosphors: DFT Calculations, Different Site Occupations, and Luminescence Mechanisms. *Chem. Mater.* **2014**, *26*, 2991−3001.
(230) Mikami, M. Response Function Calculations of $Ba_3Si_6O_{12}N_2$ and $Ba_3Si_6O_9N_4$ for the Understanding of the Optical Properties of the Eu-Doped Phosphors. *Opt. Mater.* **2013**, *35*, 1958−1961.
(231) Tolhurst, T. M.; Boyko, T. D.; Pust, P.; Johnson, N. W.; Schnick, W.; Moewes, A. Investigations of the Electronic Structure and Bandgap of the Next-Generation LED-Phosphor $Sr[LiAl_3N_4]:Eu^{2+}$—Experiment and Calculations. *Adv. Opt. Mater.* **2015**, *3*, 546−550.
(232) Andriessen, J.; Dorenbos, P.; van Eijk, C. W. E. The Centroid Shift of the 5d Levels of $Ce^{3+}$ with respect to the 4f Levels in Ionic Crystals, A Theoretical Investigation. *Nucl. Instrum. Methods Phys. Res., Sect. A* **2002**, *486*, 399−402.
(233) Ning, L.; Wang, Y.; Wang, Z.; Jin, W.; Huang, S.; Duan, C.; Zhang, Y.; Chen, W.; Liang, H. First-Principles Study on Site Preference and 4f→5d Transitions of $Ce^{3+}$ in $Sr_3AlO_4F$. *J. Phys. Chem. A* **2014**, *118*, 986−992.
(234) Baroni, S.; de Gironcoli, S.; Dal Corso, A.; Giannozzi, P. Phonons and Related Crystal Properties from Density-Functional Perturbation Theory. *Rev. Mod. Phys.* **2001**, *73*, 515−562.
(235) Mikami, M.; Nakamura, S.; Itoh, M.; Nakajima, K.; Shishido, T. Lattice Dynamics and Dielectric Properties of Yttrium Oxysulfide. *Phys. Rev. B: Condens. Matter Mater. Phys.* **2002**, *65*, 094302.
(236) Shaltaf, R.; Juwhari, H. K.; Hamad, B.; Khalifeh, J.; Rignanese, G.-M.; Gonze, X. Structural, Electronic, Vibrational, and Dielectric Properties of $LaBGeO_5$ from First Principles. *J. Appl. Phys.* **2014**, *115*, 074103.
(237) Mikami, M.; Nakamura, S. Electronic Structure of Rare-Earth Sesquioxides and Oxysulfides. *J. Alloys Compd.* **2006**, *408−412*, 687−692.
(238) Vali, R. Electronic, Dynamical, and Dielectric Properties of Lanthanum Oxysulfide. *Comput. Mater. Sci.* **2006**, *37*, 300−305.
(239) Mikami, M.; Kijima, N. 5d Levels of Rare-Earth Ions in Oxynitride/Nitride Phosphors: To What Extent is the Idea Covalency Reliable? *Opt. Mater.* **2010**, *33*, 145−148.
(240) Newnham, R. E. *Properties of Materials: Anisotropy, Symmetry, Structure*; Oxford University Press: Oxford, UK, 2004.
(241) Mikami, M.; Watanabe, H.; Uheda, K.; Kijima, N. Nitridoaluminosilicate $CaAlSiN_3$ and Its Derivatives−Theory and Experiment. *Mater. Res. Soc. Symp. Proc.* **2008**, *1040*, Q10.
(242) Kijima, N.; Seto, T.; Hirosaki, N. A New Yellow Phosphor $La_3SiA_6N_{11}:Ce^{3+}$ for White LEDs. *ECS Trans.* **2009**, *25*, 247−252.
(243) Alemany, P.; Moreira, I. d. P. R.; Castillo, R.; Llanos, J. Electronic, Structural, and Optical Properties of Host Materials for Inorganic Phosphors. *J. Alloys Compd.* **2012**, *513*, 630−640.
(244) Li, Y. Q.; Delsing, A. C. A.; Metslaar, R.; de With, G.; Hintzen, H. T. Photoluminescence Properties of Rare-Earth Activated $BaSi_7N_{10}$. *J. Alloys Compd.* **2009**, *487*, 28−33.
(245) Takeda, T.; Hirosaki, N.; Xie, R.-J.; Kimoto, K.; Saito, M. Anomalous Eu Layer Doping in Eu, Si Co-Doped Aluminium Nitride Based Phosphor and Its Direct Observation. *J. Mater. Chem.* **2010**, *20*, 9948−9953.
(246) Dutczak, D.; Justel, T.; Ronda, C.; Meijerink, A. $Eu^{2+}$ Luminescence in Strontium Aluminates. *Phys. Chem. Chem. Phys.* **2015**, *17*, 15236−15249.
(247) Wu, J. L.; Gundiah, G.; Cheetham, A. K. Structure−Property Correlations in Ce-Doped Garnet Phosphors for Use in Solid State Lighting. *Chem. Phys. Lett.* **2007**, *441*, 250−254.
(248) Maniquiz, M. C.; Jung, K. Y.; Jeong, S. M. Luminescence Characteristics of $Y_3Al_{5-2y}(Mg, Si)_yO_{12}$:Ce Phosphor Prepared by Spray Pyrolysis. *J. Electrochem. Soc.* **2010**, *157*, H1135−H1139.
(249) Miao, S.; Xia, Z.; Molokeev, M. S.; Chen, M.; Zhang, J.; Liu, Q. Effect of Al/Si Substitution on the Structure and Luminescence Properties of $CaSrSiO_4:Ce^{3+}$ Phosphors: Analysis Based on the Polyhedra Distortion. *J. Mater. Chem. C* **2015**, *3*, 4616−4622.
(250) Ghigna, P.; Pin, S.; Ronda, C.; Speghini, A.; Piccinelli, F.; Bettinelli, M. Local Structure of the $Ce^{3+}$ ion in the Yellow Emitting Phosphor YAG:Ce. *Opt. Mater.* **2011**, *34*, 19−22.
(251) Seijo, L.; Barandiarán, Z. 4f and 5d Levels of $Ce^{3+}$ in $D_2$ 8-Fold Oxygen Coordination. *Opt. Mater.* **2013**, *35*, 1932−1940.
(252) Seijo, L.; Barandiaran, Z. Host Effects on the Optically Active 4f and 5d Levels of $Ce^{3+}$ in Garnets. *Phys. Chem. Chem. Phys.* **2013**, *15*, 19221−19231.
(253) Muñoz-García, A. B.; Seijo, L. Ce and La Single- and Double-Substitutional Defects in Yttrium Aluminum Garnet: First-Principles Study. *J. Phys. Chem. A* **2011**, *115*, 815−823.


DOI: 10.1021/acs.chemrev.6b00691
*Chem. Rev.* XXXX, XXX, XXX−XXX

(254) Muñoz-García, A. B.; Pascual, J. L.; Barandiarán, Z.; Seijo, L. Structural Effects and 4f-5d Transition Shifts Induced by La Codoping in Ce-Doped Yttrium Aluminum Garnet: First-Principles Study. *Phys. Rev. B: Condens. Matter Mater. Phys.* **2010**, *82*, 064114.
(255) Muñoz-García, A. B.; Seijo, L. Structural, Electronic, and Spectroscopic Effects of Ga Codoping on Ce-Doped Yttrium Aluminum Garnet: First-Principles Study. *Phys. Rev. B: Condens. Matter Mater. Phys.* **2010**, *82*, 184118.
(256) Muñoz-García, A. B.; Barandiaran, Z.; Seijo, L. Antisite Defects in Ce-Doped YAG ($Y_3Al_5O_{12}$): First-Principles Study on Structures and 4f-5d Transitions. *J. Mater. Chem.* **2012**, *22*, 19888−19897.
(257) Stephan, M.; Zachau, M.; Gröting, M.; Karplak, O.; Eyert, V.; Mishra, K. C.; Schmidt, P. C. A Theoretical Investigation of 4f→5d Transition of Trivalent Rare Earth Ions in Fluorides and Complex Oxides. *J. Lumin.* **2005**, *114*, 255−266.
(258) Ning, L.; Wu, C.; Li, L.; Lin, L.; Duan, C.; Zhang, Y.; Seijo, L. First-Principles Study on Structural Properties and 4f→5d Transitions of Locally Charge-Compensated $Ce^{3+}$ in $CaF_2$. *J. Phys. Chem. C* **2012**, *116*, 18419−18426.
(259) Manthey, W. J. Crystal Field and Site Symmetry of Trivalent Cerium Ions in $CaF_2$: The $C_{4v}$ and $C_{3v}$ Centers with Interstitial-Fluoride Charge Compensator. *Phys. Rev. B* **1973**, *8*, 4086−4098.
(260) Ma, N.-Y.; Yang, F.; Shen, X.-C.; Huang, Y.-C.; Ning, L.-X. Ab Initio Study on Spectral Properties of Charge-Compensated $Ce^{3+}$ in NaF. *Chin. J. Chem. Phys.* **2014**, *27*, 512−518.
(261) Robertson, J. M.; van Tol, M. W.; Smits, W. H.; Heynen, J. P. H. Colorshift of the $Ce^{3+}$ Emission in Monocrystalline Epitaxially Grown Garnet Layers. *Philips J. Res.* **1981**, *36*, 15−30.
(262) Pan, Y.; Wu, M.; Su, Q. Tailored Photoluminescence of YAG:Ce Phosphor through Various Methods. *J. Phys. Chem. Solids* **2004**, *65*, 845−850.
(263) Watanabe, S.; Ogasawara, K. Experimental and First-Principles Analysis of 4f−5d Absorption Spectrum for $Ce^{3+}$ in $LiYF_4$ Considering Lattice Relaxation. *J. Phys. Soc. Jpn.* **2008**, *77*, 084702.
(264) Phung, Q. M.; Barandiarán, Z.; Seijo, L. Structural Relaxation Effects on the Lowest 4f-5d transition of $Ce^{3+}$ in garnets. *Theor. Chem. Acc.* **2015**, *134*, 37.
(265) Ferrara, C.; Tealdi, C.; Pedone, A.; Menziani, M. C.; Rossini, A. J.; Pintacuda, G.; Mustarelli, P. Local versus Average Structure in $LaSrAl_3O_7$: A NMR and DFT Investigation. *J. Phys. Chem. C* **2013**, *117*, 23451−23458.
(266) Jia, Y.; Miglio, A.; Poncé, S.; Gonze, X.; Mikami, M. First-Principles Study of $Ce^{3+}$-Doped Lanthanum Silicate Nitride Phosphors: Neutral Excitation, Stokes Shift, and Luminescent Center Identification. *Phys. Rev. B: Condens. Matter Mater. Phys.* **2016**, *93*, 155111.
(267) Burdick, G. W.; Reid, M. F. *Handbook on the Physics and Chemistry of Rare Earths*; Gschneidner, K. A., Bünzli, J.-C., Pecharsky, V. K., Eds.; Elsevier Science B.V.: Amsterdam, 2007; Vol. 37, pp 61−98.
(268) Reid, M. F.; van Pieterson, L.; Meijerink, A. Trends in Parameters for the $4f^N \leftrightarrow 4f^{N-1}5d$ Spectra of Lanthanide Ions in Crystals. *J. Alloys Compd.* **2002**, *344*, 240−245.
(269) Dai, D.; Li, L.; Ren, J.; Whangbo, M.-H. Description of Ligand Field Splitting in terms of Density Functional Theory: Calculations of the Split Levels of the $^2F_{5/2}$ and $^2F_{7/2}$ Subterms in CeO and CeF under the Weak Field Coupling Scheme. *J. Chem. Phys.* **1998**, *108*, 3479−3488.
(270) Ren, J.; Whangbo, M.-H.; Dai, D.; Li, L. Description of Ligand Field Splitting in terms of Density Functional Theory: Split Levels of the Lowest-Lying Subterms of the $4f^{n-1}6s^2$ (n = 3−14) Configurations in Lanthanide Monofluorides LnF (Ln = Pr−Yb). *J. Chem. Phys.* **1998**, *108*, 8479−8484.
(271) Zbiri, M.; Daul, C. A.; Wesolowski, T. A. Effect of the f-Orbital Delocalization on the Ligand-Field Splitting Energies in Lanthanide-Containing Elpasolites. *J. Chem. Theory Comput.* **2006**, *2*, 1106−1111.
(272) Ning, L.; Zhang, L.; Hu, L.; Yang, F.; Duan, C.; Zhang, Y. DFT Calculations of Crystal-Field Parameters for the Lanthanide Ions in the $LaCl_3$ Crystal. *J. Phys.: Condens. Matter* **2011**, *23*, 205502.
(273) Xia, Z.; Ma, C.; Molokeev, M. S.; Liu, Q.; Rickert, K.; Poeppelmeier, K. R. Chemical Unit Cosubstitution and Tuning of Photoluminescence in the $Ca_2(Al_{1-x}Mg_x)(Al_{1-x}Si_{1+x})O_7:Eu^{2+}$ Phosphor. *J. Am. Chem. Soc.* **2015**, *137*, 12494−12497.
(274) Blasse, G.; Bril, A. Characteristic Luminescence II. The Efficiency of Phosphors Excited in the Activator. *Philips Tech. Rev.* **1970**, *31*, 314−323.
(275) Dorenbos, P. Electronic Structure Engineering of Lanthanide Activated Materials. *J. Mater. Chem.* **2012**, *22*, 22344−22349.
(276) Ning, L.; Wang, Z.; Wang, Y.; Liu, J.; Huang, S.; Duan, C.; Zhang, Y.; Liang, H. First-Principles Study on Electronic Properties and Optical Spectra of Ce-Doped $La_2CaB_{10}O_{19}$ Crystal. *J. Phys. Chem. C* **2013**, *117*, 15241−15246.
(277) Canning, A.; Chaudhry, A.; Boutchko, R.; Grønbech-Jensen, N. First-Principles Study of Luminescence in Ce-Doped Inorganic Scintillators. *Phys. Rev. B: Condens. Matter Mater. Phys.* **2011**, *83*, 125115.
(278) Wen, J.; Ning, L.; Duan, C.; Zhan, S.; Huang, Y.; Zhang, J.; Yin, M. First-Principles Study on Structural, Electronic, and Spectroscopic Properties of $\gamma$-$Ca_2SiO_4:Ce^{3+}$ Phosphors. *J. Phys. Chem. A* **2015**, *119*, 8031−8039.
(279) Ning, L.; Lin, L.; Li, L.; Wu, C.; Duan, C.; Zhang, Y.; Seijo, L. Electronic Properties and 4f→5d Transitions in Ce-Doped $Lu_2SiO_5$: A Theoretical Investigation. *J. Mater. Chem.* **2012**, *22*, 13723−13731.
(280) Ibrahim, I. A. M.; Lenčéš, Z.; Benco, L.; Hrabalová, M.; Šajgalík, P. Cerium-Doped $LaSi_3N_5$: Computed Electronic Structure and Band Gaps. *J. Eur. Ceram. Soc.* **2014**, *34*, 2705−2712.
(281) Benco, L.; Lenčéš, Z.; Šajgalík, P.; Jáné, E.; Velič, D. Europium-Doped $LaSi_3N_5$ Ternary Nitride: Synthesis, Spectroscopy, Computed Electronic Structure and Band Gaps. *J. Am. Ceram. Soc.* **2011**, *94*, 4345−4351.
(282) Ibrahim, I. A. M.; Lenčéš, Z.; Benco, L.; Hrabalová, M.; Šajgalík, P. Sm-Doped $LaSi_3N_5$: Synthesis, Computed Electronic Structure, and Band Gaps. *J. Am. Ceram. Soc.* **2014**, *97*, 2546−2551.
(283) Ibrahim, I. A. M.; Lenčéš, Z.; Šajgalík, P.; Benco, L. Electronic Structure and Energy Level Schemes of $RE^{3+}:LaSi_3N_5$ and $RE^{2+}:LaSi_3N_{5-x}O_x$ Phosphors (RE = Ce, Pr, ND, Pm, Sm, Eu) from First Principles. *J. Lumin.* **2015**, *164*, 131−137.
(284) Chaudhry, A.; Boutchko, R.; Chourou, S.; Zhang, G.; Grønbech-Jensen, N.; Canning, A. First-Principles Study of Luminescence in $Eu^{2+}$-Doped Inorganic Scintillators. *Phys. Rev. B: Condens. Matter Mater. Phys.* **2014**, *89*, 155105.
(285) Watras, A.; Matraszek, A.; Godlewska, P.; Szczygieł, I.; Wojtkiewicz, J.; Brzostowski, B.; Banach, G.; Hanuza, J.; Dereń, P. J. The Role of the Ca Vacancy in the Determination of the Europium Position in the Energy Gap, Its Valence State and Spectroscopic Properties in $KCa(PO_3)_3$. *Phys. Chem. Chem. Phys.* **2014**, *16*, 5581−5588.
(286) Biswas, K.; Du, M.-H. Energy Transport and Scintillation of Cerium-doped Elpasolite $Cs_2LiYCl_6$: Hybrid Density Functional Calculations. *Phys. Rev. B: Condens. Matter Mater. Phys.* **2012**, *86*, 014102.
(287) Du, M.-H.; Biswas, K. Electronic Structure Engineering of Elpasolites: Case of $Cs_2AgYCl_6$. *J. Lumin.* **2013**, *143*, 710−714.
(288) Erhart, P.; Sadigh, B.; Schleife, A.; Åberg, D. First-Principles Study of Codoping in Lanthanum Bromide. *Phys. Rev. B: Condens. Matter Mater. Phys.* **2015**, *91*, 165206.
(289) Chaudhry, A.; Canning, A.; Boutchko, R.; Weber, M. J.; Grønbech-Jensen, N.; Derenzo, S. E. First-Principles Studies of Ce-Doped $RE_2M_2O_7$ (RE = Y, La; M = Ti, Zr, Hf): A Class of Nonscintillators. *J. Appl. Phys.* **2011**, *109*, 083708.
(290) Dorenbos, P. Locating Lanthanide Impurity Levels in the Forbidden Band of Host Crystals. *J. Lumin.* **2004**, *108*, 301−305.
(291) Wang, D.; Xia, S.; Yin, M. Ab Initio Calculation of Electronic Structures and 4f-5d Transitions of Some Rare Earth Ions Doped in Crystal $YPO_4$. *J. Rare Earths* **2008**, *26*, 439−442.
(292) Yao, G.; Berry, M. T.; May, P. S.; Kilin, D. DFT Calculation of Russell−Saunders Splitting for Lanthanide Ions Doped in Hexagonal ($\beta$)-$NaYF_4$ Nanocrystals. *J. Phys. Chem. C* **2013**, *117*, 17177−17185.


DOI: 10.1021/acs.chemrev.6b00691
*Chem. Rev.* XXXX, XXX, XXX−XXX

(293) Yao, G.; Huang, S.; Berry, M. T.; May, P. S.; Kilin, D. S. Non-Collinear Spin DFT for Lanthanide Ions in Doped Hexagonal $NaYF_4$. *Mol. Phys.* **2014**, *112*, 546−556.
(294) Cho, I. S.; Yim, D. K.; Kwak, C. H.; An, J. S.; Roh, H. S.; Hong, K. S. Investigation of Crystal/Electronic Structure Effects on the Photoluminescence Properties in the $BaO−SiO_2:Eu^{2+}$ Systems. *J. Lumin.* **2012**, *132*, 375−380.
(295) Fang, C. M.; Biswas, K. Preferential Eu Site Occupation and Its Consequences in the Ternary Luminescent Halides $AB_2I_5:Eu^{2+}$ (A = Li−Cs; B = Sr, Ba). *Phys. Rev. Appl.* **2015**, *4*, 014012.
(296) Andriessen, J.; Dorenbos, P.; van Eijk, C. W. E. Ab Initio Calculation of the Contribution from Anion Dipole Polarization and Dynamic Correlation to 4f-5d Excitations of $Ce^{3+}$ in Ionic Compounds. *Phys. Rev. B: Condens. Matter Mater. Phys.* **2005**, *72*, 045129.
(297) Gracia, J.; Seijo, L.; Barandiarán, Z.; Curulla, D.; Niemansverdriet, H.; van Gennip, W. Ab Initio Calculations on the Local Structure and the 4f-5d Absorption and Emission Spectra of $Ce^{3+}$-doped YAG. *J. Lumin.* **2008**, *128*, 1248−1254.
(298) Pascual, J. L.; Barandiarán, Z.; Seijo, L. Ab Initio Theoretical Study of Luminescence Properties of $Pr^{3+}$-Doped $Lu_2O_3$. *Theor. Chem. Acc.* **2011**, *129*, 545−554.
(299) Pascual, J. L.; Barandiarán, Z.; Seijo, L. Ab Initio Theoretical Study of the $4f^8$ and $4f^7 5d$ Manifolds of $Tb^{3+}$-Doped $BaF_2$ Cubic Sites. *J. Lumin.* **2014**, *145*, 808−817.
(300) Sánchez-Sanz, G.; Seijo, L.; Barandiarán, Z. Energy Gaps in the $4f^{13}5d^1$ Manifold and Multiple Spontaneous Emissions in $Yb^{2+}$-Doped $CsCaBr_3$. *J. Phys. Chem. A* **2009**, *113*, 12591−12598.
(301) Ruipérez, F.; Barandiarán, Z.; Seijo, L. Quantum Chemical Study of 4f→5d Excitations of Trivalent Lanthanide Ions Doped in the Cubic Elpasolite $Cs_2NaYCl_6$. $Ce^{3+}$ to $Tb^{3+}$. *J. Chem. Phys.* **2005**, *123*, 244703.
(302) Barandiarán, Z.; Seijo, L. On the Bond Length Change upon $4f^1 \rightarrow 5d^1$ Excitations in Eightfold Coordination: $CaF_2:Ce^{3+}$ Cubic Defects. *Theor. Chem. Acc.* **2006**, *116*, 505−508.
(303) Ning, L.; Yang, F.; Duan, C.; Zhang, Y.; Liang, J.; Cui, Z. Structural Properties and 4f→5d Absorptions in Ce-Doped $LuAlO_3$: A First-Principles Study. *J. Phys.: Condens. Matter* **2012**, *24*, 055502.
(304) Ning, L.; Zhou, C.; Chen, W.; Huang, Y.; Duan, C.; Dorenbos, P.; Tao, Y.; Liang, H. Electronic Properties of $Ce^{3+}$-Doped $Sr_3Al_2O_5Cl_2$: A Combined Spectroscopic and Theoretical Study. *J. Phys. Chem. C* **2015**, *119*, 6785−6792.
(305) Oh, J. H.; Eo, Y. J.; Yoon, H. C.; Huh, Y.-D.; Do, Y. R. Evaluation of New Color Metrics: Guidelines for Developing Narrow-Band Red Phosphors for WLEDs. *J. Mater. Chem. C* **2016**, *4*, 8326−8348.
(306) Zhu, Q.-Q.; Wang, L.; Hirosaki, N.; Hao, L. Y.; Xu, X.; Xie, R.-J. Extra-Broad Band Orange-Emitting $Ce^{3+}$-Doped $Y_3Si_5N_9O$ Phosphor for Solid-State Lighting: Electronic, Crystal Structures and Luminescence Properties. *Chem. Mater.* **2016**, *28*, 4829−4839.
(307) Poncé, S.; Jia, Y.; Giantomassi, M.; Mikami, M.; Gonze, X. Understanding Thermal Quenching of Photoluminescence in Oxynitride Phosphors from First Principles. *J. Phys. Chem. C* **2016**, *120*, 4040−4047.
(308) Schmiechen, S.; Schneider, H.; Wagatha, P.; Hecht, C.; Schmidt, P. J.; Schnick, W. Toward New Phosphors for Application in Illumination-Grade White pc-LEDs: The Nitridomagnesosilicates $Ca[Mg_3SiN_4]:Ce^{3+}$, $Sr[Mg_3SiN_4]:Eu^{2+}$, and $Eu[Mg_3SiN_4]$. *Chem. Mater.* **2014**, *26*, 2712−2719.
(309) Tolhurst, T. M.; Schmiechen, S.; Pust, P.; Schmidt, P. J.; Schnick, W.; Moewes, A. Electronic Structure, Bandgap, and Thermal Quenching of $Sr[Mg_3SiN_4]:Eu^{2+}$ in Comparison to $Sr[LiAl_3N_4]:Eu^{2+}$. *Adv. Opt. Mater.* **2016**, *4*, 584−591.
(310) Kechele, J. A.; Oeckler, O.; Stadler, F.; Schnick, W. Structure Elucidation of $BaSi_2O_2N_2$ − A Host Lattice for Rare-Earth Doped Luminescent Materials in Phosphor-Converted (pc)-LEDs. *Solid State Sci.* **2009**, *11*, 537−543.
(311) Wang, L.; Ni, H.; Zhang, Q.; Xiao, F. Electronic Structure and Linear Optical Property of $BaSi_2N_2O_2$ Crystal. *J. Alloys Compd.* **2011**, *509*, 10203−10206.
(312) Bulloni, C.; García-Fuente, A.; Urland, W.; Daul, C. Effect of $Ca^{2+}$ Codoping on the $Eu^{2+}$ Luminescence Properties in the $Sr_2Si_5N_8$ Host Lattice: A Theoretical Approach. *Phys. Chem. Chem. Phys.* **2015**, *17*, 24925−24930.
(313) Wang, C.; Zhao, Z.; Wu, Q.; Zhu, G.; Wang, Y. Enhancing the Emission Intensity and Decreasing the Full Widths at Half Maximum of $Ba_3Si_6O_{12}N_2:Eu^{2+}$ by $Mg^{2+}$ Doping. *Dalton Trans.* **2015**, *44*, 10321−10329.
(314) Przybylińska, H.; Ma, C.-G.; Brik, M. G.; Kamińska, A.; Sybilski, P.; Wittlin, A.; Berkowski, M.; Zorenko, Yu.; Gorbenko, V.; Wrzesinski, H.; et al. Electronic Structure of $Ce^{3+}$ Multicenters in Yttrium Aluminum Garnets. *Appl. Phys. Lett.* **2013**, *102*, 241112.
(315) Seijo, L.; Barandiaran, Z. Large Splittings of the 4f Shell of $Ce^{3+}$ in Garnets. *Phys. Chem. Chem. Phys.* **2014**, *16*, 3830−3834.
(316) Brites, C. D. S.; Xie, X.; Debasu, M. L.; Qin, X.; Chen, R.; Huang, W.; Rocha, J.; Liu, X.; Carlos, L. D. Instantaneous Ballistic Velocity of Suspended Brownian Nanocrystals Measured by Upconversion Nanothermometry. *Nat. Nanotechnol.* **2016**, *11*, 851−856.
(317) Blasse, G.; Wanmaker, W. L.; ter Vrugt, J. W.; Bril, A. Fluorescence of $Eu^{2+}$ Activated Silicates. *Philips Res. Rep.* **1968**, *23*, 189.
(318) Blasse, G.; Bril, A.; De Vries, J. Luminescence of Alkaline-Earth Borate-Phosphates Activated with Divalent Europium. *J. Inorg. Nucl. Chem.* **1969**, *31*, 568−570.
(319) Happek, U.; Basun, S. A.; Choi, J.; Krebs, J. K.; Raukas, M. Electron Transfer Processes in Rare Earth Doped Insulators. *J. Alloys Compd.* **2000**, *303*−*304*, 198−206.
(320) Lin, C. C.; Xiao, Z. R.; Guo, G.-Y.; Chan, T.-S.; Liu, R.-S. Versatile Phosphate Phosphors $ABPO_4$ in White Light-Emitting Diodes: Collocated Characteristic Analysis and Theoretical Calculations. *J. Am. Chem. Soc.* **2010**, *132*, 3020−3028.
(321) Muñoz, G. H.; de la Cruz, C. L.; Muñoz, A. F.; Rubio, J. O. High-Temperature Luminescence Properties of $Eu^{2+}$-Activated Alkali Halide Phosphor Materials. *J. Mater. Sci. Lett.* **1988**, *7*, 1310−1312.
(322) Ivanovskikh, K. V.; Ogiegło, J. M.; Zych, A.; Ronda, C. R.; Meijerink, A. Luminescence Temperature Quenching for $Ce^{3+}$ and $Pr^{3+}$ *d-f* Emission in YAG and LuAG. *ECS J. Solid State Sci. Technol.* **2013**, *2*, R3148−R3152.
(323) Najafov, H.; Kato, A.; Toyota, H.; Iwai, K.; Bayramov, A.; Iida, S. Effect of Ce Co-Doping on $CaGa_2S_4$:Eu Phosphor: II. Thermoluminescence. *Jpn. J. Appl. Phys.* **2002**, *41*, 2058−2065.
(324) Sontakke, A. D.; Ueda, J.; Xu, J.; Asami, K.; Katayama, M.; Inada, Y.; Tanabe, S. A Comparison on $Ce^{3+}$ Luminescence in Borate Glass and YAG Ceramic: Understanding the Role of Host's Characteristics. *J. Phys. Chem. C* **2016**, *120*, 17683−17691.
(325) Dorenbos, P. Thermal Quenching of $Eu^{2+}$ 5d-4f Luminescence in Inorganic Compounds. *J. Phys.: Condens. Matter* **2005**, *17*, 8103−8111.
(326) Liu, C.; Qi, Z.; Ma, C.-C.; Dorenbos, P.; Hou, D.; Zhang, S.; Kuang, X.; Zhang, J.; Liang, H. High Light Yield of $Sr_8(Si_4O_{12})Cl_8:Eu^{2+}$ under X-ray Excitation and Its Temperature-Dependent Luminescence Characteristics. *Chem. Mater.* **2014**, *26*, 3709−3715.
(327) Luo, H.; Ning, L.; Dong, Y.; Bos, A. J. J.; Dorenbos, P. Electronic Structure and Site Occupancy of Lanthanide-Doped $(Sr,Ca)_3(Y,Lu)_2Ge_3O_{12}$ Garnets: A Spectroscopic and First-Principles Study. *J. Phys. Chem. C* **2016**, *120*, 28743−28752.
(328) Bertrand, B.; Poncé, S.; Waroquiers, D.; Stankovski, M.; Giantomassi, M.; Mikami, M.; Gonze, X. Quasiparticle Electronic Structure of Barium-Silicon Oxynitrides for White-LED Application. *Phys. Rev. B: Condens. Matter Mater. Phys.* **2013**, *88*, 075136.
(329) Chen, L.; Fei, M.; Zhang, Z.; Jiang, Y.; Chen, S.; Dong, Y.; Sun, Z.; Zhao, Z.; Fu, Y.; He, J.; et al. Understanding the Local and Electronic Structures toward Enhanced Thermal Stable Luminescence of $CaAlSiN_3:Eu^{2+}$. *Chem. Mater.* **2016**, *28*, 5505−5515.


DOI: 10.1021/acs.chemrev.6b00691
*Chem. Rev.* XXXX, XXX, XXX−XXX

(330) Dorenbos, P. Light Output and Energy Resolution of $Ce^{3+}$-Doped Scintillators. *Nucl. Instrum. Methods Phys. Res., Sect. A* **2002**, *486*, 208−213.
(331) Poort, S. H. M.; Meyerink, A.; Blasse, G. Lifetime Measurements in $Eu^{2+}$-Doped Host Lattices. *J. Phys. Chem. Solids* **1997**, *58*, 1451−1456.
(332) Andrews, D. L. A Unified Theory of Radiative and Radiationless Molecular Energy Transfer. *Chem. Phys.* **1989**, *135*, 195−201.
(333) Vergeer, P. Experimental Techniques. *Luminescence: From Theory to Applications*; Ronda, C., Ed.; Wiley-VCH, 2007; pp 219−250.
(334) Song, A. K. S.; Williams, R. T. *Self-Trapped Excitons*; Springer, 1996.
(335) Wei, H.; Du, M.-H.; Stand, L.; Zhao, Z.; Shi, H.; Zhuravleva, M.; Melcher, C. L. Scintillation Properties and Electronic Structures of the Intrinsic and Extrinsic Mixed Elpasolites $Cs_2NaRBr_3I_3$ (R = La, Y). *Phys. Rev. Appl.* **2016**, *5*, 024008.
(336) Shi, H.; Du, M.-H. Discrete Electronic Bands in Semiconductors and Insulators: Potential High-Light-Yield Scintillators. *Phys. Rev. Appl.* **2015**, *3*, 054005.
(337) Smet, P. F.; Parmentier, A. B.; Poelman, D. Selecting Conversion Phosphors for White Light-Emitting Diodes. *J. Electrochem. Soc.* **2011**, *158*, R37−R54.
(338) Nikl, M.; Mihokova, E.; Pejchal, J.; Vedda, A.; Zorenko, Y.; Nejezchleb, K. The Antisite $Lu_{Al}$ Defect-Related Trap in $Lu_3Al_5O_{12}$:Ce Single Crystal. *Phys. Status Solidi B* **2005**, *242*, R119−R121.
(339) Nikl, M. Energy Transfer Phenomena in the Luminescence of Wide Band-Gap Scintillators. *Phys. Status Solidi A* **2005**, *202*, 201−206.
(340) Muñoz-García, A. B.; Artacho, E.; Seijo, L. Atomistic and Electronic Structure of Antisite Defects in Yttrium Aluminum Garnet: Density-Functional Study. *Phys. Rev. B: Condens. Matter Mater. Phys.* **2009**, *80*, 014105.
(341) Muñoz-García, A. B.; Anglada, E.; Seijo, L. First-Principles Study of the Structure and the Electronic Structure of Yttrium Aluminum Garnet $Y_3Al_5O_{12}$. *Int. J. Quantum Chem.* **2009**, *109*, 1991−1998.
(342) Huang, Z.; Zhang, L.; Pan, W. Antisite Defect in Nonstoichiometric Yttrium Aluminum Garnet: Experimental and First-Principles Calculation. *J. Eur. Ceram. Soc.* **2014**, *34*, 783−790.
(343) Hu, C.; Liu, S.; Shi, Y.; Kou, H.; Li, J.; Pan, Y.; Feng, X.; Liu, Q. Antisite Defects in Nonstoichiometric $Lu_3Al_5O_{12}$:Ce Ceramic Scintillators. *Phys. Status Solidi B* **2015**, *252*, 1993−1999.
(344) Ning, L.; Cheng, W.; Zhou, C.; Duan, C.; Zhang, Y. Energetic, Optical, and Electronic Properties of Intrinsic Electron-Trapping Defects in $YAlO_3$: A Hybrid DFT Study. *J. Phys. Chem. C* **2014**, *118*, 19940−19947.
(345) Singh, D. J. Antisite Defects and Traps in Perovskite $YAlO_3$ and $LuAlO_3$: Density Functional Calculations. *Phys. Rev. B: Condens. Matter Mater. Phys.* **2007**, *76*, 214115.
(346) Yamaga, M.; Lee, D.; Henderson, B.; Han, T. P. J.; Gallagher, H. G.; Yosida, T. The Magnetic and Optical Properties of $Ce^{3+}$ in $LiCaAlF_6$. *J. Phys.: Condens. Matter* **1998**, *10*, 3223.
(347) Sato, H.; Shimamura, K.; Bensalah, A.; Satonaga, T.; Mihokova, T. F.; Dusek, M.; Vedda, M. N.; Machida, H.; Fukuda, T.; Nikl, M. Color Centers in $LiCaAlF_6$ Single Crystals and Their Suppression by Doping. *J. Appl. Phys.* **2002**, *91*, 5666−5670.
(348) Gektin, A.; Shiran, N.; Neicheva, S.; Gavrilyuk, V.; Bensalah, A.; Fukuda, T.; Shimamura, K. $LiCaAlF_6$:Ce Crystal: A New Scintillator. *Nucl. Instrum. Methods Phys. Res., Sect. A* **2002**, *486*, 274−277.
(349) Yokota, Y.; Fujimoto, Y.; Yanagida, T.; Takahashi, H.; Yonetani, M.; Hayashi, K.; Park, I.; Kawaguchi, N.; Fukuda, K.; Yamaji, A.; et al. Crystal Growth of Na-Co-Doped Ce:$LiCaAlF_6$ Single Crystals and Their Optical, Scintillation, and Physical Properties. *Cryst. Growth Des.* **2011**, *11*, 4775−4779.
(350) Rahangdale, S. R.; Palikundwar, U. A.; Wankhede, S. P.; Dhabekar, B.; Kadam, S.; Moharil, S. V. Effect of Co-Doping on Luminescence of $LiCaAlF_6$:Eu Phosphor. *J. Lumin.* **2015**, *167*, 80−84.
(351) Uberuaga, B. P.; Andersson, D. A.; Stanek, C. R. Defect Behavior in Oxides: Insights from Modern Atomistic Simulation Methods. *Curr. Opin. Solid State Mater. Sci.* **2013**, *17*, 249−256.
(352) Freysoldt, C.; Grabowski, B.; Hickel, T.; Neugebauer, J.; Kresse, G.; Janotti, A.; Van de Walle, C. G. First-Principles Calculations for Point Defects in Solids. *Rev. Mod. Phys.* **2014**, *86*, 253−305.
(353) Freysoldt, C.; Lange, B.; Neugebauer, J.; Yan, Q.; Lyons, J. L.; Janotti, A.; Van de Walle, C. J. Electron and Chemical Reservoir Corrections for Point-Defect Formation Energies. *Phys. Rev. B: Condens. Matter Mater. Phys.* **2016**, *93*, 165206.
(354) Kumagai, Y.; Oba, F. Electrostatics-Based Finite-Size Corrections for First-Principles Point Defect Calculations. *Phys. Rev. B: Condens. Matter Mater. Phys.* **2014**, *89*, 195205.
(355) Du, M.-H.; Singh, D. J. Electronic Structure, Small Polaron, and F Center in $LiCaAlF_6$. *J. Appl. Phys.* **2012**, *112*, 123516.
(356) Fasoli, M.; Vedda, A.; Nikl, M.; Jiang, C.; Uberuaga, B. P.; Andersson, D. A.; McClellan, K. J.; Stanek, C. R. Band-Gap Engineering for Removing Shallow Traps in Rare-Earth $Lu_3Al_5O_{12}$ Garnet Scintillators using $Ga^{3+}$ Doping. *Phys. Rev. B: Condens. Matter Mater. Phys.* **2011**, *84*, 081102.
(357) Stanek, C. R.; Jiang, C.; Yadav, S. K.; McClellan, K. J.; Uberuaga, B. P.; Andersson, D. A.; Nikl, M. The Effect of Ga-Doping on the Defect Chemistry of $RE_3Al_5O_{12}$ Garnets. *Phys. Status Solidi B* **2013**, *250*, 244−248.
(358) Yadav, S. K.; Uberuaga, B. P.; Nikl, M.; Jiang, C.; Stanek, C. R. Band-Gap and Band-Edge Engineering of Multicomponent Garnet Scintillators from First Principles. *Phys. Rev. Appl.* **2015**, *4*, 054012.
(359) Hu, C.; Liu, S.; Fasoli, M.; Vedda, A.; Nikl, M.; Feng, X.; Pan, Y. $O^-$ Centers in LuAG:Ce,Mg Ceramics. *Phys. Status Solidi RRL* **2015**, *9*, 245−249.
(360) Van den Eeckhout, K.; Smet, P. F.; Poelman, D. Persistent Luminescence in $Eu^{2+}$-Doped Compounds: A Review. *Materials* **2010**, *3*, 2536.
(361) Kunkel, N.; Sontakke, A. D.; Kohaut, S.; Viana, B.; Dorenbos, P. Thermally Stimulated Luminescence and First-Principle Study of Defect Configurations in the Perovskite-Type Hydrides $LiMH_3$:$Eu^{2+}$ (M = Sr, Ba) and the Corresponding Deuterides. *J. Phys. Chem. C* **2016**, *120*, 29414.
(362) Lin, H.; Xu, J.; Huang, Q.; Wang, B.; Chen, H.; Lin, Z.; Wang, Y. Bandgap Tailoring via Si Doping in Inverse-Garnet $Mg_3Y_2Ge_3O_{12}$:$Ce^{3+}$ Persistent Phosphor Potentially Applicable in AC-LED. *ACS Appl. Mater. Interfaces* **2015**, *7*, 21835−21843.
(363) Zhuang, Y.; Lv, Y.; Li, Y.; Zhou, T.; Xu, J.; Ueda, J.; Tanabe, S.; Xie, R.-J. Study on Trap Levels in $SrSi_2AlO_2N_3$:$Eu^{2+}$,$Ln^{3+}$ Persistent Phosphors Based on Host-Referred Binding Energy Scheme and Thermoluminescence Analysis. *Inorg. Chem.* **2016**, *55*, 11890−11897.
(364) Huang, B. Native Point Defects in CaS: Focus on Intrinsic Defects and Rare Earth Ion Dopant Levels for Up-Converted Persistent Luminescence. *Inorg. Chem.* **2015**, *54*, 11423−11440.
(365) Savarese, M.; Aliberti, A.; De Santo, I.; Battista, E.; Causa, F.; Netti, P. A.; Rega, N. Fluorescence Lifetimes and Quantum Yields of Rhodamine Derivatives: New Insights from Theory and Experiment. *J. Phys. Chem. A* **2012**, *116*, 7491−7497.
(366) Xia, Z.; Xu, Z.; Chen, M.; Liu, Q. Recent Developments in the New Inorganic Solid-State LED Phosphors. *Dalton Trans.* **2016**, *45*, 11214−11232.
(367) Xia, Z.; Meijerink, A. $Ce^{3+}$-Doped Garnet Phosphors: Composition Modification, Luminescence Properties and Applications. *Chem. Soc. Rev.* **2017**, *46*, 275.
(368) Schubert, E. F. *Light-Emitting Diodes*; Cambridge University Press, 2006.
(369) Robbins, D. J. The Effects of Crystal Field and Temperature on the Photoluminescence Excitation Efficiency of $Ce^{3+}$ in YAG. *J. Electrochem. Soc.* **1979**, *126*, 1550−1555.
(370) Setlur, A. A. Phosphors for LED-Based Solid-State Lighting. *Electrochem. Soc. Interface* **2009**, *18*, 32−36.


DOI: 10.1021/acs.chemrev.6b00691
*Chem. Rev.* XXXX, XXX, XXX−XXX

(371) Katelnikovas, A.; Bettentrup, H.; Uhlich, D.; Sakirzanovas, S.; Jüstel, T.; Kareiva, A. Synthesis and Optical Properties of $Ce^{3+}$-Doped $Y_3Mg_2AlSi_2O_{12}$ Phosphors. *J. Lumin.* **2009**, *129*, 1356−1361.
(372) Katelnikovas, A.; Bareika, T.; Vitta, P.; Jüstel, T.; Winkler, H.; Kareiva, A.; Žukauskas, A.; Tamulaitis, G. $Y_{3-x}Mg_2AlSi_2O_{12}$: Phosphors − Prospective for Warm-White Light Emitting Diodes. *Opt. Mater.* **2010**, *32*, 1261−1265.
(373) Höppe, H. A.; Lutz, H.; Morys, P.; Schnick, W.; Seilmeier, A. Luminescence in $Eu^{2+}$-Doped $Ba_2Si_5N_8$: Fluorescence, Thermoluminescence, and Upconversion. *J. Phys. Chem. Solids* **2000**, *61*, 2001−2006.
(374) Mueller-Mach, R.; Mueller, G.; Krames, M. R.; Höppe, H. A.; Stadler, F.; Schnick, W.; Juestel, T.; Schmidt, P. Highly Efficient All-Nitride Phosphor-Converted White Light Emitting Diode. *Phys. Status Solidi A* **2005**, *202*, 1727−1732.
(375) Uheda, K.; Hirosaki, N.; Yamamoto, H. Host Lattice Materials in the System $Ca_3N_2$−AlN−$Si_3N_4$ for White Light Emitting Diode. *Phys. Status Solidi A* **2006**, *203*, 2712−2717.
(376) Xia, Q.; Batentschuk, M.; Osvet, A.; Winnacker, A.; Schneider, J. Quantum Yield of $Eu^{2+}$ Emission in $(Ca_{1-x}Sr_x)S$:Eu Light Emitting Diode Converter at 20−420 K. *Radiat. Meas.* **2010**, *45*, 350−352.
(377) Zhang, X.; Mo, F.; Zhou, L.; Gong, M. Properties−Structure Relationship Research on $LiCaPO_4$:$Eu^{2+}$ as Blue Phosphor for NUV LED Application. *J. Alloys Compd.* **2013**, *575*, 314−318.
(378) Piquette, A.; Bergbauer, W.; Galler, B.; Mishra, K. C. On Choosing Phosphors for Near-UV and Blue LEDs for White Light. *ECS J. Solid State Sci. Technol.* **2016**, *5*, R3146−R3159.
(379) McKittrick, J.; Hannah, M. E.; Piquette, A.; Han, J. K.; Choi, J. I.; Anc, M.; Galvez, M.; Lugauer, H.; Talbot, J. B.; Mishra, K. C. Phosphor Selection Considerations for Near-UV LED Solid State Lighting. *ECS J. Solid State Sci. Technol.* **2013**, *2*, R3119−R3131.
(380) Dai, P.; Cao, J.; Zhang, X.; Liu, Y. Bright and High-Color-Rendering White Light-Emitting Diode Using Color-Tunable Oxychloride and Oxyfluoride Phosphors. *J. Phys. Chem. C* **2016**, *120*, 18713−18720.
(381) Chiu, Y.-C.; Liu, W.-R.; Chang, C.-K.; Liao, C.-C.; Yeh, Y.-T.; Jang, S.-M.; Chen, T.-M. $Ca_2PO_4Cl$:$Eu^{2+}$: An Intense Near-Ultraviolet Converting Blue Phosphor for White Light-Emitting Diodes. *J. Mater. Chem.* **2010**, *20*, 1755−1758.
(382) Dai, P.-P.; Li, C.; Zhang, X.-T.; Xu, J.; Chen, X.; Wang, X.-L.; Jia, Y.; Wang, X.; Liu, Y.-C. A Single $Eu^{2+}$-Activated High-Color-Rendering Oxychloride White-Light Phosphor for White-Light-Emitting Diodes. *Light: Sci. Appl.* **2016**, *5*, e16024.
(383) Jiang, L.; Pang, R.; Li, D.; Sun, W.; Jia, Y.; Li, H.; Fu, J.; Li, C.; Zhang, S. Tri-Chromatic White-Light Emission from a Single-Phase $Ca_9Sc(PO_4)_7$:$Eu^{2+}$,$Tb^{3+}$,$Mn^{2+}$ Phosphor for LED Applications. *Dalton Trans.* **2015**, *44*, 17241−17250.
(384) Wang, Z.; Lou, S.; Li, P. Single Phase Tunable Warm White-Light-Emitting $Sr_3La(PO_4)_3$:$Eu^{2+}$, $Sm^{3+}$ Phosphor for White LEDs. *Opt. Mater. Express* **2016**, *6*, 114−124.
(385) Li, C.; Dai, J.; Yu, H.; Deng, D.; Huang, J.; Wang, L.; Hua, Y.; Xu, S. Luminescence Properties of Single-Phase Color-Tunable $Li_4SrCa(Si_2O_4N_{8/3})$:$Eu^{2+}$ Phosphor for White Light-Emitting Diodes. *RSC Adv.* **2016**, *6*, 38731−38740.
(386) Lu, Q.-F.; Li, J.; Wang, D.-J. Single-Phased Silicate-Hosted Phosphor with 660 nm-Featured Band Emission for Biological Light-Emitting Diodes. *Curr. Appl. Phys.* **2013**, *13*, 1506−1511.
(387) Pinho, P.; Jokinen, K.; Halonen, L. Horticultural Lighting − Present and Future Challenges. *Lighting Res. Technol.* **2012**, *44*, 427−437.
(388) Wang, D.; Mao, Z.; Fahlman, B. D. Phosphors with a 660-nm-Featured Emission for LED/LD Lighting in Horticulture. *Phosphors, Up Conversion Nano Particles, Quantum Dots and Their Applications*; Liu, R. S., Ed.; Springer Singapore: Singapore, 2016; Vol. 2, pp 83−117.
(389) Liu, X.; Lei, B.; Liu, Y. The Application of Phosphor in Agricultural Field. *Phosphors, Up Conversion Nano Particles, Quantum Dots and Their Applications*; Liu, R.-S., Ed.; Springer Singapore: Singapore, 2016; Vol. 2, pp 119−137.
(390) Wang, J.; Zhang, X.; Su, Q. Rare Earth Solar Spectral Convertor for Si Solar Cells. *Phosphors, Up Conversion Nano Particles, Quantum Dots and Their Applications*; Liu, R.-S., Ed.; Springer Singapore: Singapore, 2016; Vol. 2, pp 139−166.
(391) Zhang, Q.; Wang, J.; Zhang, G.; Su, Q. UV Photon Harvesting and Enhanced Near-Infrared Emission in Novel Quantum Cutting $Ca_2BO_3Cl$:$Ce^{3+}$,$Tb^{3+}$,$Yb^{3+}$ Phosphor. *J. Mater. Chem.* **2009**, *19*, 7088−7092.
(392) Zhou, J.; Teng, Y.; Ye, S.; Zhuang, Y.; Qiu, J. Enhanced Downconversion Luminescence by Co-Doping $Ce^{3+}$ in $Tb^{3+}$−$Yb^{3+}$ Doped Borate Glasses. *Chem. Phys. Lett.* **2010**, *486*, 116−118.
(393) Liu, T.-C.; Zhang, G.; Qiao, X.; Wang, J.; Seo, H. J.; Tsai, D.-P.; Liu, R.-S. Near-Infrared Quantum Cutting Platform in Thermally Stable Phosphate Phosphors for Solar Cells. *Inorg. Chem.* **2013**, *52*, 7352−7357.
(394) Ueda, J.; Tanabe, S. Visible to Near Infrared Conversion in $Ce^{3+}$−$Yb^{3+}$ Co-Doped YAG Ceramics. *J. Appl. Phys.* **2009**, *106*, 043101.
(395) Smedskjaer, M. M.; Qiu, J.; Wang, J.; Yue, Y. Near-Infrared Emission from Eu−Yb Doped Silicate Glasses Subjected to Thermal Reduction. *Appl. Phys. Lett.* **2011**, *98*, 071911.
(396) Zhang, G.; Liu, C.; Wang, J.; Kuang, X.; Su, Q. A Dual-Mode Solar Spectral Converter $CaLaGa_3S_6O$:$Ce^{3+}$,$Pr^{3+}$: UV-Vis-NIR Luminescence Properties and Solar Spectral Converting Mechanism. *J. Mater. Chem.* **2012**, *22*, 2226−2232.
(397) Zhang, W.; Ding, F.; Chou, S. Y. Large Enhancement of Upconversion Luminescence of $NaYF_4$:$Yb^{3+}$/$Er^{3+}$ Nanocrystal by 3D Plasmonic Nano-Antennas. *Adv. Mater.* **2012**, *24*, OP236−OP241.
(398) Röntgen, W. C. On a New Kind of Rays. *Science* **1896**, *3*, 227−231.
(399) Fuchs, A. W. *Radiography of 1896*; George Eastman House, 1960; Vol. 9, pp 4−17.
(400) Hofstadter, R. The Detection of Gamma-Rays with Thallium-Activated Sodium Iodide Crystals. *Phys. Rev.* **1949**, *75*, 796−810.
(401) Van Sciver, W.; Hofstadter, R. Scintillations in Thallium-Activated $CaI_2$ and CsI. *Phys. Rev.* **1951**, *84*, 1062−1063.
(402) Gillette, R. H. Calcium and Cadmium Tungstate as Scintillation Counter Crystals for Gamma-Ray Detection. *Rev. Sci. Instrum.* **1950**, *21*, 294−301.
(403) Weber, M. J.; Monchamp, R. R. Luminescence of $Bi_4Ge_3O_{12}$: Spectral and Decay Properties. *J. Appl. Phys.* **1973**, *44*, 5495−5499.
(404) van Eijk, C. W. E.; Dorenbos, P.; Visser, R. $Nd^{3+}$ and $Pr^{3+}$ Doped Inorganic Scintillators. *IEEE Trans. Nucl. Sci.* **1994**, *41*, 738−741.
(405) Dorenbos, P.; Visser, R.; van Eijk, C. W. E.; Khaidukov, N. M.; Korzhik, M. V. Scintillation Properties of Some $Ce^{3+}$ and $Pr^{3+}$ Doped Inorganic Crystals. *IEEE Trans. Nucl. Sci.* **1993**, *40*, 388−394.
(406) Dorenbos, P. Fundamental Limitations in the Performance of $Ce^{3+}$-, $Pr^{3+}$-, and $Eu^{2+}$-Activated Scintillators. *IEEE Trans. Nucl. Sci.* **2010**, *57*, 1162−1167.
(407) Wisniewski, D.; Tavernier, S.; Wojtowicz, A. J.; Wisniewska, M.; Bruyndonckx, P.; Dorenbos, P.; van Loef, E.; van Eijk, C. W. E.; Boatner, L. A. $LuPO_4$:Nd and $YPO_4$:Nd—New Promising VUV Scintillation Materials. *Nucl. Instrum. Methods Phys. Res., Sect. A* **2002**, *486*, 239−243.
(408) van Eijk, C. W. E. Inorganic Scintillators in Medical Imaging. *Phys. Med. Biol.* **2002**, *47*, R85−R106.
(409) Conti, M. State of the Art and Challenges of Time-Of-Flight PET. *Phys. Med.* **2009**, *25*, 1−11.
(410) Lecoq, P. Development of New Scintillators for Medical Applications. *Nucl. Instrum. Methods Phys. Res., Sect. A* **2016**, *809*, 130−139.
(411) Melcher, C. L.; Schweitzer, J. S. A Promising New Scintillator: Cerium-Doped Lutetium Oxyorthosilicate. *Nucl. Instrum. Methods Phys. Res., Sect. A* **1992**, *314*, 212−214.
(412) Melcher, C. L.; Schweitzer, J. S. Cerium-Doped Lutetium Oxyorthosilicate: A Fast, Efficient New Scintillator. *IEEE Trans. Nucl. Sci.* **1992**, *39*, 502−505.


DOI: 10.1021/acs.chemrev.6b00691
*Chem. Rev.* XXXX, XXX, XXX−XXX

(413) Wienhard, K.; Schmand, M.; Casey, M. E.; Baker, K.; Bao, J.; Eriksson, L.; Jones, W. F.; Knoess, C.; Lenox, M.; Lercher, M.; et al. The ECAT HRRT: Performance and First Clinical Application of the New High Resolution Research Tomograph. *IEEE Trans. Nucl. Sci.* **2002**, *49*, 104−110.
(414) Herzog, H.; Tellmann, L.; Hocke, C.; Pietrzyk, U.; Casey, M. E.; Kuwert, T. NEMA NU2−2001 Guided Performance Evaluation of Four Siemens ECAT PET Scanners. *IEEE Trans. Nucl. Sci.* **2004**, *51*, 2662−2669.
(415) van Loef, E. V. D.; Dorenbos, P.; van Eijk, C. W. E.; Krämer, K.; Güdel, H. U. High-Energy-Resolution Scintillator: $Ce^{3+}$ Activated $LaBr_3$. *Appl. Phys. Lett.* **2001**, *79*, 1573−1575.
(416) Quarati, F. G. A.; Khodyuk, I. V.; van Eijk, C. W. E.; Quarati, P.; Dorenbos, P. Study of $^{138}La$ Radioactive Decays using $LaBr_3$ Scintillators. *Nucl. Instrum. Methods Phys. Res., Sect. A* **2012**, *683*, 46−52.
(417) Quarati, F. G. A.; Dorenbos, P.; van der Biezen, J.; Owens, A.; Selle, M.; Parthier, L.; Schotanus, P. Scintillation and Detection Characteristics of High-Sensitivity $CeBr_3$ Gamma-Ray Spectrometers. *Nucl. Instrum. Methods Phys. Res., Sect. A* **2013**, *729*, 596−604.
(418) Runkle, R. C.; Bernstein, A.; Vanier, P. E. Securing Special Nuclear Material: Recent Advances in Neutron Detection and Their Role in Nonproliferation. *J. Appl. Phys.* **2010**, *108*, 111101.
(419) van Eijk, C. W. E. Inorganic Scintillators for Thermal Neutron Detection. *IEEE Trans. Nucl. Sci.* **2012**, *59*, 2242−2247.
(420) Alekhin, M. S.; de Haas, J. T. M.; Kramer, K. W.; Dorenbos, P. Scintillation Properties of and Self Absorption in $SrI_2:Eu^{2+}$. *IEEE Trans. Nucl. Sci.* **2011**, *58*, 2519−2527.
(421) Shirwadkar, U.; Hawrami, R.; Glodo, J.; van Loef, E. V. D.; Shah, K. S. Promising Alkaline Earth Halide Scintillators for Gamma-Ray Spectroscopy. *IEEE Trans. Nucl. Sci.* **2013**, *60*, 1011−1015.
(422) Nikl, M.; Pejchal, J.; Mihokova, E.; Mares, J. A.; Ogino, H.; Yoshikawa, A.; Fukuda, T.; Vedda, A.; D'Ambrosio, C. Antisite Defect-Free $Lu_3(Ga_xAl_{1-x})_5O_{12}$:Pr Scintillator. *Appl. Phys. Lett.* **2006**, *88*, 141916.
(423) Kamada, K.; Endo, T.; Tsutumi, K.; Yanagida, T.; Fujimoto, Y.; Fukabori, A.; Yoshikawa, A.; Pejchal, J.; Nikl, M. Composition Engineering in Cerium-Doped $(Lu,Gd)_3(Ga,Al)_5O_{12}$ Single-Crystal Scintillators. *Cryst. Growth Des.* **2011**, *11*, 4484−4490.
(424) Kamada, K.; Yanagida, T.; Pejchal, J.; Nikl, M.; Endo, T.; Tsutumi, K.; Fujimoto, Y.; Fukabori, A.; Yoshikawa, A. Scintillator-Oriented Combinatorial Search in Ce-Doped $(Y,Gd)_3(Ga,Al)_5O_{12}$ Multicomponent Garnet Compounds. *J. Phys. D: Appl. Phys.* **2011**, *44*, 505104.
(425) Spurrier, M. A.; Szupryczynski, P.; Yang, K.; Carey, A. A.; Melcher, C. L. Effects of $Ca^{2+}$ Co-Doping on the Scintillation Properties of LSO:Ce. *IEEE Trans. Nucl. Sci.* **2008**, *55*, 1178−1182.
(426) Wu, Y.; Meng, F.; Li, Q.; Koschan, M.; Melcher, C. L. Role of $Ce^{4+}$ in the Scintillation Mechanism of Codoped $Gd_3Ga_3Al_2O_{12}$:Ce. *Phys. Rev. Appl.* **2014**, *2*, 044009.
(427) Liu, S.; Feng, X.; Zhou, Z.; Nikl, M.; Shi, Y.; Pan, Y. Effect of $Mg^{2+}$ Co-Doping on the Scintillation Performance of LuAG:Ce Ceramics. *Phys. Status Solidi RRL* **2014**, *8*, 105−109.
(428) Nikl, M.; Kamada, K.; Babin, V.; Pejchal, J.; Pilarova, K.; Mihokova, E.; Beitlerova, A.; Bartosiewicz, K.; Kurosawa, S.; Yoshikawa, A. Defect Engineering in Ce-Doped Aluminum Garnet Single Crystal Scintillators. *Cryst. Growth Des.* **2014**, *14*, 4827−4833.
(429) Liu, S.; Mares, J. A.; Feng, X.; Vedda, A.; Fasoli, M.; Shi, Y.; Kou, H.; Beitlerova, A.; Wu, L.; D'Ambrosio, C.; Pan, Y.; Nikl, M. Towards Bright and Fast $Lu_3Al_5O_{12}$:Ce,Mg Optical Ceramics Scintillators. *Adv. Opt. Mater.* **2016**, *4*, 731−739.
(430) Nikl, M.; Yoshikawa, A.; Kamada, K.; Nejezchleb, K.; Stanek, C. R.; Mares, J. A.; Blazek, K. Development of LuAG-Based Scintillator Crystals − A Review. *Prog. Cryst. Growth Charact. Mater.* **2013**, *59*, 47−72.
(431) Ricci, P. C.; Carbonaro, C. M.; Chiriu, D.; Anedda, A. Structurally Defective Cerium Doped Lutetium-Yttrium Oxyorthosilicates for Optically Stimulated Luminescence Imaging Devices. *J. Mater. Chem.* **2011**, *21*, 18425−18430.
(432) Chiriu, D.; Carbonaro, C. M.; Corpino, R.; Stagi, L.; Ricci, P. C. Selective Reading of Stored Information in RE Doped Aluminium Perovskites. *Cryst. Res. Technol.* **2015**, *50*, 43−48.
(433) Liu, X.; Zhang, J.; Zhang, X.; Hao, Z.; Qiao, J.; Dong, X. Strongly Enhancing Photostimulated Luminescence by Doping $Tm^{3+}$ in $Sr_3SiO_5:Eu^{2+}$. *Opt. Lett.* **2013**, *38*, 148−150.
(434) Wang, W. X.; Imai, Y.; Xu, C. N.; Matsubara, T.; Takao, Y. A New Smart Damage Sensor Using Mechanoluminescence Material. *Mater. Sci. Forum* **2011**, *675*−*677*, 1081−1084.
(435) Liu, Y.; Lei, B. Persistent Luminescent Materials. *Phosphors, Up Conversion Nano Particles, Quantum Dots and Their Applications*; Liu, R.-S., Ed.; Springer Singapore: Singapore, 2016; Vol. *2*; pp 167−214.
(436) Smith, A. M.; Mancini, M. C.; Nie, S. Bioimaging: Second Window for In Vivo Imaging. *Nat. Nanotechnol.* **2009**, *4*, 710−711.
(437) Rodríguez Burbano, D. C.; Sharma, S. K.; Dorenbos, P.; Viana, B.; Capobianco, J. A. Persistent and Photostimulated Red Emission in $CaS:Eu^{2+},Dy^{3+}$ Nanophosphors. *Adv. Opt. Mater.* **2015**, *3*, 551−557.
(438) Rodríguez Burbano, D. C.; Sharma, S. K.; Dorenbos, P.; Viana, B.; Capobianco, J. A. Persistent and Photostimulated Red Emission in $CaS:Eu^{2+},Dy^{3+}$ Nanophosphors. *Adv. Opt. Mater.* **2015**, *3*, 415−415.
(439) Chen, W.; Wang, Y.; Zeng, W.; Li, G.; Guo, H. Design, Synthesis and Characterization of Near-Infrared Long Persistent Phosphors $Ca_4(PO_4)_2O:Eu^{2+},R^{3+}$ (R = Lu, La, Gd, Ce, Tm, Y). *RSC Adv.* **2016**, *6*, 331−337.
(440) Ibarra-Ruiz, A. M.; Rodríguez Burbano, D. C.; Capobianco, J. A. Photoluminescent Nanoplatforms in Biomedical Applications. *Adv. Phys. X* **2016**, *1*, 194−225.
(441) Jaque, D.; Richard, C.; Viana, B.; Soga, K.; Liu, X.; García Solé, J. Inorganic Nanoparticles for Optical Bioimaging. *Adv. Opt. Photonics* **2016**, *8*, 1−103.
(442) Maldiney, T.; Scherman, D.; Richard, C. Persistent Luminescence Nanoparticles for Diagnostics and Imaging. *Functional Nanoparticles for Bioanalysis, Nanomedicine, and Bioelectronic Devices*; Hepel, M., Zhong, C.-J., Eds.; American Chemical Society, 2012; Vol. *2*, pp 1−25.
(443) Li, Z.-J.; Zhang, H.-W.; Sun, M.; Shen, J.-S.; Fu, H.-X. A Facile and Effective Method to Prepare Long-Persistent Phosphorescent Nanospheres and Its Potential Application for In Vivo Imaging. *J. Mater. Chem.* **2012**, *22*, 24713−24720.
(444) Wu, B.-Y.; Wang, H.-F.; Chen, J.-T.; Yan, X.-P. Fluorescence Resonance Energy Transfer Inhibition Assay for α-Fetoprotein Excreted during Cancer Cell Growth Using Functionalized Persistent Luminescence Nanoparticles. *J. Am. Chem. Soc.* **2011**, *133*, 686−688.
(445) Gutiérrez-Martín, F.; Fernández-Martinez, F.; Díaz, P.; Colón, C.; Alonso-Medina, A. Persistent UV Phosphors for Application in Photo Catalysis. *J. Alloys Compd.* **2010**, *501*, 193−197.
(446) Wang, P.; Xu, X.; Zhou, D.; Yu, X.; Qiu, J. Sunlight Activated Long-Lasting Luminescence from $Ba_5Si_8O_{21}:Eu^{2+},Dy^{3+}$ Phosphor. *Inorg. Chem.* **2015**, *54*, 1690−1697.
(447) Li, H.; Wang, Y. Photocatalysis Enhancement of $CaAl_2O_4:Eu^{2+}$, $Nd^{3+}@TiO_2$ Composite Powders. *Res. Chem. Intermed.* **2010**, *36*, 51−59.
(448) Wang, C.; Xuan, T.; Liu, J.; Li, H.; Sun, Z. Long Afterglow $SrAl_2O_4:Eu^{2+},Dy^{3+}$ Phosphors as Luminescent Down-Shifting Layer for Crystalline Silicon Solar Cells. *Int. J. Appl. Ceram. Technol.* **2015**, *12*, 722−727.
(449) Shwetha, G.; Kanchana, V.; Vaitheeswaran, G. $CsMgCl_3$: A Promising Cross Luminescence Material. *J. Solid State Chem.* **2015**, *227*, 110−116.
(450) Chen, X.; Liu, L.; Liu, G. Recent Progress on the Spectroscopy of Rare Earth Ions in Core-Shells, Nanowires, Nanotubes, and Other Novel Nanostructures. *J. Nanosci. Nanotechnol.* **2008**, *8*, 1126−1137.
(451) Wang, F.; Han, Y.; Lim, C. S.; Lu, Y.; Wang, J.; Xu, J.; Chen, H.; Zhang, C.; Hong, M.; Liu, X. Simultaneous Phase and Size Control of Upconversion Nanocrystals through Lanthanide Doping. *Nature* **2010**, *463*, 1061−1065.
(452) Tu, D.; Liu, Y.; Zhu, H.; Li, R.; Liu, L.; Chen, X. Breakdown of Crystallographic Site Symmetry in Lanthanide-Doped $NaYF_4$ Crystals. *Angew. Chem., Int. Ed.* **2013**, *52*, 1128−1133.


DOI: 10.1021/acs.chemrev.6b00691
*Chem. Rev.* XXXX, XXX, XXX−XXX

(453) Chen, X.; Jin, L.; Kong, W.; Sun, T.; Zhang, W.; Liu, X.; Fan, J.; Yu, S. F.; Wang, F. Confining Energy Migration in Upconversion Nanoparticles towards Deep Ultraviolet Lasing. *Nat. Commun.* **2016**, *7*, 10304.
(454) Sui, Y.; Tao, K.; Tian, Q.; Sun, K. Interaction Between $Y^{3+}$ and Oleate Ions for the Cubic-to-Hexagonal Phase Transformation of $NaYF_4$ Nanocrystals. *J. Phys. Chem. C* **2012**, *116*, 1732−1739.
(455) Wang, F.; Sun, L.-D.; Gu, J.; Wang, Y.-F.; Feng, W.; Yang, Y.; Wang, J.; Yan, C.-H. Selective Heteroepitaxial Nanocrystal Growth of Rare Earth Fluorides on Sodium Chloride: Synthesis and Density Functional Calculations. *Angew. Chem., Int. Ed.* **2012**, *51*, 8796−8799.
(456) Zherebetskyy, D.; Scheele, M.; Zhang, Y.; Bronstein, N.; Thompson, C.; Britt, D.; Salmeron, M.; Alivisatos, P.; Wang, L.-W. Hydroxylation of the Surface of PbS Nanocrystals Passivated with Oleic Acid. *Science* **2014**, *344*, 1380−1384.
(457) Sluydts, M.; De Nolf, K.; Van Speybroeck, V.; Cottenier, S.; Hens, Z. Ligand Addition Energies and the Stoichiometry of Colloidal Nanocrystals. *ACS Nano* **2016**, *10*, 1462−1474.
(458) Liu, D.; Xu, X.; Du, Y.; Qin, X.; Zhang, Y.; Ma, C.; Wen, S.; Ren, W.; Goldys, E. M.; Piper, J. A.; et al. Three-Dimensional Controlled Growth of Monodisperse Sub-50 nm Heterogeneous Nanocrystals. *Nat. Commun.* **2016**, *7*, 10254.


DOI: 10.1021/acs.chemrev.6b00691
*Chem. Rev.* XXXX, XXX, XXX−XXX